ATOMIC FORCE MICROSCOPY-BASED NANOMECHANICAL CHARACTERIZATION OF KENAF MICROFIBER AND CELLULOSE NANOFIBRIL

A Thesis
Submitted to the Graduate Faculty
of the
North Dakota State University
of Agriculture and Applied Science

By

M. Subbir Parvej

In Partial Fulfillment of the Requirements
for the Degree of
MASTER OF SCIENCE

Major Department:
Mechanical Engineering

November 2020

Fargo, North Dakota

North Dakota State University
Graduate School

Title

ATOMIC FORCE MICROSCOPY-BASED NANOMECHANICAL CHARACTERIZATION OF KENAF MICROFIBER AND CELLULOSE NANOFIBRIL

By

M. Subbir Parvej

The Supervisory Committee certifies that this ***disquisition*** complies with North Dakota State University's regulations and meets the accepted standards for the degree of

MASTER OF SCIENCE

SUPERVISORY COMMITTEE:

Dr. Xinnan Wang
Chair

Dr. Chad Ulven

Dr. Long Jiang

Dr. Annie Tangpong

Dr. Nurun Nahar

Approved:

November 25, 2020
Date

Dr. Alan Kallmeyer
Department Chair

ABSTRACT

Kenaf fiber is increasingly getting the attention of the industries due to its excellent mechanical properties, feasibility, growth rate, and ease of cultivation. On the other hand, cellulose nanofibril is one of the important building blocks of all the bast fibers which significantly contributes to their mechanical properties. However, most of the studies in the literature have estimated the value of axial elastic modulus for fiber-bundles which has some unavoidable issues resulting in incorrect modulus. Moreover, the transverse elastic modulus is another important parameter that also needs to be studied. Hence, to compensate for the gap in the literature, a single unit of both kenaf microfiber and cellulose nanofibril have been subjected to nanomechanical characterization to analyze their surface morphology and determine their elastic modulus in the axial and transverse direction. The experiments also pave to a protocol to characterize micro and nanofibrils nanomechanically and determine their elastic moduli.

ACKNOWLEDGEMENTS

It was an amazing ride to come near the completion of my degree in North Dakota State University by the grace of the almighty. The person to whom I am most thankful throughout the journey is my supervisor Dr. Xinnan Wang who introduced me to the amazing world of nanotechnology and the 'plenty of room at the bottom'. With an immense patience and compassion, he has continuously paved me the way to excel in my academic affair and professional goals. Moreover, his insightful teaching in ethical and spiritual development will be always remembered. Besides, I shall be endebted to him for his time to review my writings and encouragement to development of my writing skill.

The contribution of Dr. Chad Ulven and his group is particularly mentionable. I would love to acknowledge his contributions to find fiber supplier, his kind consent to use his apparatus, and arrangements of proper training to run my experiment. Besides, his thoughtful reviews, questions, and feedbacks from his profound knowledge in the field of fiber were very helpful to improve my research and thesis. I am also grateful to Dr. Long Jiang for supplying the cellulose nanofibril and helping me with valuable tips and suggestions to perform my study on it. Credit also goes to my colleagues Joseph Fehrenbach, Dallas Patton and Qian Ma who helped me in the sample preparation and training. Additionally, I recognize the guidelines of Dr. Annie Tangpong and Dr. Nurun Nahar to bring my thesis in a good shape with appropriate data and formatting.

Last but not the least is the acknowledgement of the constant mental and emotional support of my parents and family members that has always driven me with the impetus to develop myself everyday and fortified me with the ambition to reach the pinnacle. Special thanks to Dr. Sumathy Krishnan and my beloved friends Md. Faisal Kabir, Tanvir Ahmed, Arup Dey,

Tabassum Tanha Sharna, Md. Mozammal Kamal, and Joshua Liaw for their amazing companionship and sweet memories which I would cherish rest of my life.

DEDICATION

I dedicate my effort to my family, well-wishers, and the amazing people around me who always encourage me to work and dream for a better world.

TABLE OF CONTENTS

LIST OF TABLES

LIST OF FIGURES

LIST OF ABBREVIATIONS

AFM	Atomic Force Microscopy
CNF	Cellulose Nanofibril
BC	Bacterial Cellulose
STM	Scanning Tunneling Microscopy
SPM	Scanning Probe Microscopy
TEM	Transmission Electron Microscopy
SEM	Secondary Electron Microscopy
EELS	Electron Energy Loss Spectroscopy
XRD	X-Ray Diffraction
JKR	Johnson-Kendall-Roberts
DMT	Derjaguin-Muller-Toporov
MD	Maugis-Dugdale
AD	Anderson-Darling

LIST OF SYMBOLS

a	Contact Radius
k	Elastic Constant
R	Nominal Radius
P	Contact Force
δ	Indentation Depth
E	Elastic Modulus
K	Nominal Elastic Constant
G	Adhesion Release Rate
γ	Surface Energy
z_o	Equilibrium Distance between Two Atomic Planes
c	Radius of Adhesive Region
m	Ratio of Contact Radius and Radius of Adhesive Region
σ_o	Uniform Adhesive Stress
μ	Tabor Parameter
M_e	Normalized Effective Mass
ρ	Density of Cantilever
b	Width of Cantilever
h	Thickness of Cantilever
l	Length of Cantilever
w_{vac}	Unloaded Resonance Frequency of Cantilever
Δz	Z-axis Displacement of Probe
R_i	Radius of Indenter
R_s	Radius of Sample Surface

$P(\sigma)$ ..... Probability Function

m ..... Shape Parameter

σ_o ..... Characteristic Parameter

σ_f ..... Experimental Value

β ..... Scale Parameter

γ ..... Threshold Parameter

F ..... Applied Load

$\Delta\delta$ ..... Change in Deflection

I ..... Second Moment of Inertia

1. INTRODUCTION

1.1. Background

In today's world, human civilization has already reached the stage of saturation in using conventional neat materials for structural purposes. It has become increasingly necessary to form composite materials with expected properties. Composite materials are the materials which are made from two or more constituent materials that are essentially different in physical or chemical properties. When the different materials are combined, they can produce a material with characteristics different from the individual components. Unlike the mixtures and solid solutions, the individual components in composite material remain separate and distinct within the finished structure [1]. Typically, there are two phases of materials in composites: continuous and dispersed phase. In terms of composites, the continuous phase is also known as a matrix where the distributed material through the matrix is popularly known as reinforcements or fillers. A schematic of the arrangement of these two phases is illustrated in Figure 1.1 [2, 3].

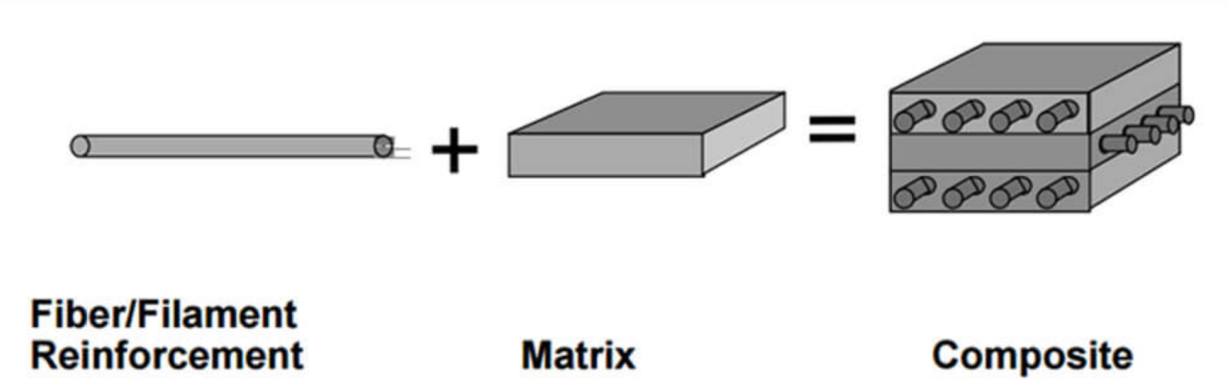

Figure 1.1. Schematic of composite structure.

Composite-based industries are currently using a wide range of reinforcement materials. Fibers, fillers, flakes, whiskers, particulates, and directionally solidified eutectics are the commonly used reinforcements in the composites, where using fiber as reinforcement is one of the most popular ways for reinforcement [4]. This type of composite consists of three types of

components: the fibers as the discontinuous or dispersed phase, the matrix as the continuous phase, and the fine interphase region between matrix and filler which possess higher tensile properties. Depending on the sources, fibers can be classified into two categories: synthetic fiber and natural fiber. Synthetic fibers are the human-made artificial fibers through chemical synthesis where the fiber-forming materials are extruded from spinnerets. Figure 1.2 is a simplified diagram of the synthetic fiber manufacturing process [5, 6].

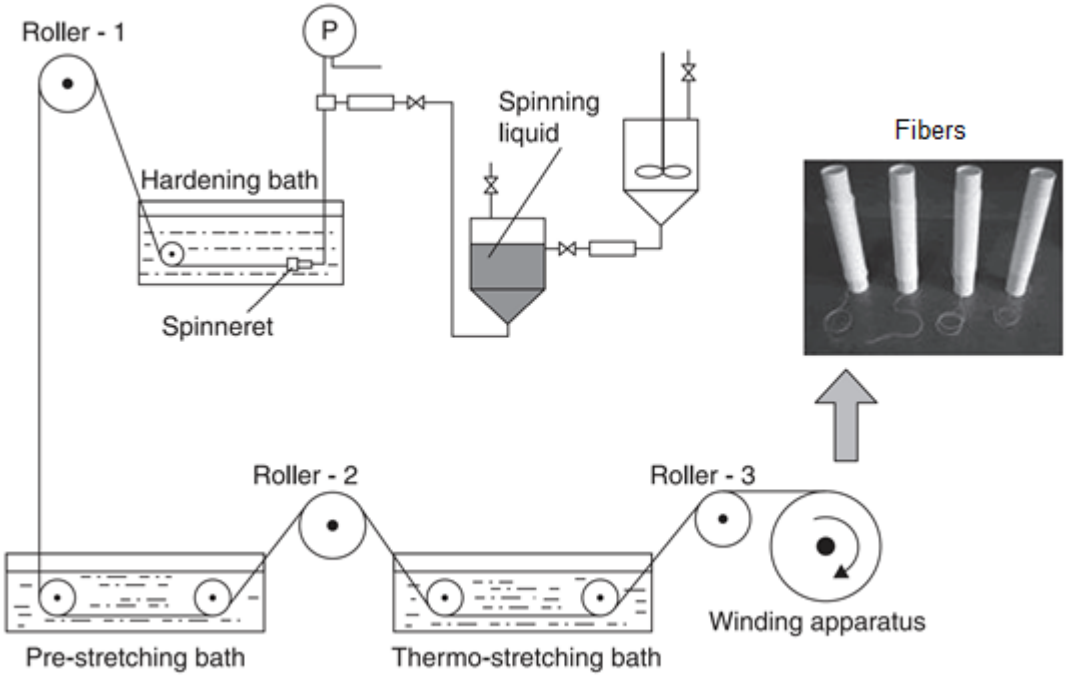

Figure 1.2. Synthetic fiber manufacturing [5].

Nylon, polyester, Acrylic, Spandex, Kevlar, Dacron, Terelyne, etc. are the most commonly used synthetic fibers. The lucrative features offered by synthetic fibers are their higher tensile strength, wrinkle freeness, abrasion resistance, durability, quick-drying and water resistance, less shrinkage, and resistance to discoloration [7-11]. At the same time, the noxious impact of this non-biodegradable fiber in nature, health issues, and its less feasibility are the issues for which the modern world is looking for its replacements [12-15]. On the other hand, natural fibers are highly biodegradable and eco-friendly. These are the type of fibers that we

extract directly from nature and use with little or no modification. Moreover, low specific weight, high thermal stability, appreciable resistance to heat and electricity, renewability, feasibility, and excellent performance as acoustic insulation are some other unique properties of natural fibers [16-20]. Besides, the high yield of natural fibers involves lower cost, less energy, and lower CO_2 emission than synthetic fibers [17]. Figure 1.3 shows a comparative cost study between some popular natural and synthetic fibers where we can find most natural fibers are more feasible and less costly than synthetic fibers [21]. Hence, natural fibers have appeared as a potential replacement for synthetic fibers and industries are increasingly switching to natural fibers as reinforcements in composites.

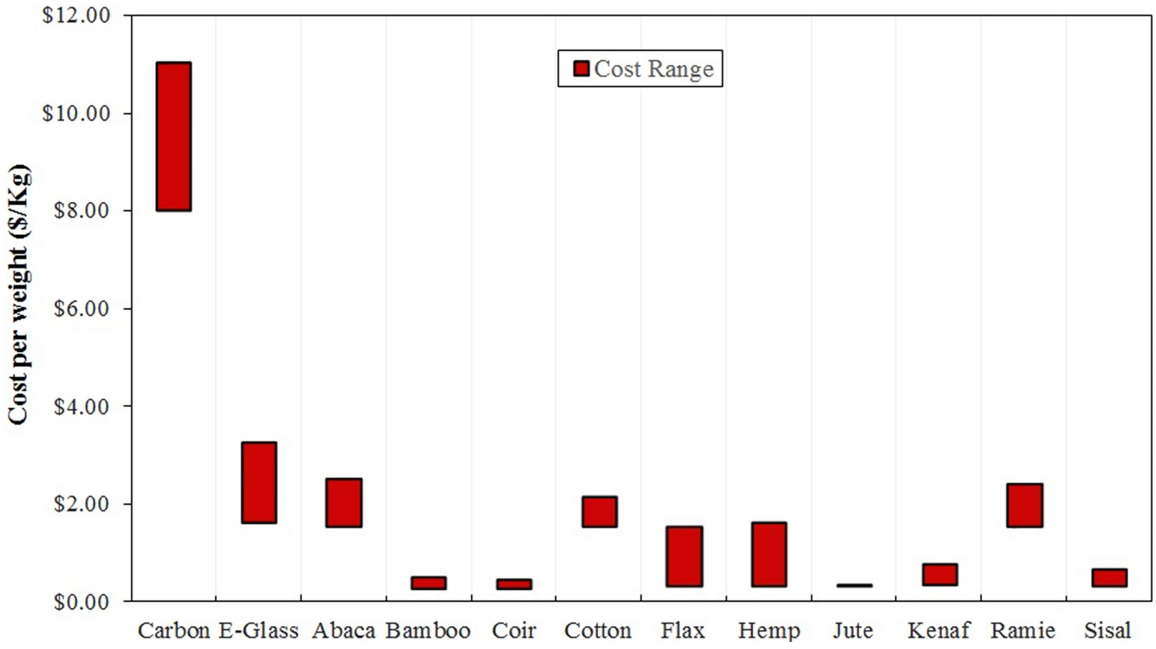

Figure 1.3. Comparative cost of different fibers [21].

Natural fiber-based composites have already started to dominate in the industries related to automobiles, aerospace, sports, electronics packaging, and building and construction materials, e.g., window frame, panels, decking, etc.[22-25]. Natural fibers in composites have been found to effectively reduce CO_2 and enhance fuel efficiency from motor vehicles.

Additionally, the weight and cost were reduced by 30% and 20%, respectively, with the use of these composites in the vehicles. Similarly, it has advantages in other sectors for which the industries are gradually moving towards natural fibers. Figure 1.4 shows the global natural fiber composite market revenue by application in 2016 where a lion share of biocomposites are found to be used in automotive industries [26]. There are numerous sources from where it is possible to extract natural fibers and kenaf, jute, sisal, coir, flax, and hemp are the most commonly used natural fibers that are incorporated in the polymer matrix to tailor the mechanical properties [22]. These natural fibers are exceptionally important for their excellent mechanical properties, e.g., tensile strength, flexural strength, and impact strength [27, 28].

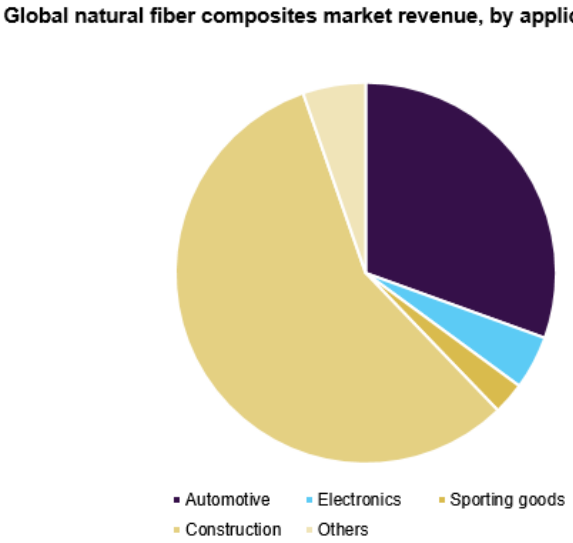

Figure 1.4. Global natural fiber composite market revenue by application in 2016 [26].

1.2. Kenaf fiber

Kenaf (*Hibiscus cannabinus* L.) is a member of the Malvaceae family. It is an annual herbaceous unbranched plant with a height of 8-14 feet and it may even reach 20 feet in some cases. It has a considerable significance as a multipurpose plant due to having a huge potential for its fiber, energy, and feedstock. Despite its sparse presence in tropics and subtropics, kenaf is endemic to most African countries south of the Sahara and Sudan. These countries have been

cultivating this plant as a domestic fiber growing plant for about 6000 years. However, India is the largest producer of this fiber [29]. Research on the kenaf bast fibers began in the USA at the time of World War II when jute imports from Asia stopped. In the 1950s, the Agricultural Research Service (ARS), Department of Agriculture of the USA spotted kenaf as the 'most promising non-wood fiber plant as an outcome of screening from more than 500 plant species to select the potential fiber sources to harness pulp for paper manufacturing. Currently, research and development are going on, on kenaf mostly in Texas, Oklahoma, Mississippi, and Southeastern USA [30]. Figure 1.5 shows a photo of kenaf plants and seeds [31].

Figure 1.5. Kenaf plants and seeds [31].

The yield of kenaf can be influenced by the timing of planting, photoperiod, length of the growing season, plant populations, and the level of maturity of the plant [32]. In a research, the total dry yield of the rain-fed crop was found as 10 t.ha-1 if harvested in the mid-September and 13 t.ha-1 if harvested in late October. If a well-watered condition is maintained, crop biomass can increase by 50%. Besides, it has time dependency and can increase linearly with time to reach 20 t.ha-1 [33]. There are two factors which influence kenaf's agricultural advantages: (i) kenaf can absorb a significant amount of nitrogen and phosphorus from soil; (ii) the rate of

carbon dioxide accumulation is high. Kenaf can absorb nitrogen and phosphorus at a rate of 0.81 g/m^2 and 0.11 g/m^2 per day, respectively which is several times higher than many other plants [34]. Besides, the photosynthesis rate of kenaf is much higher than the photosynthesis rates of conventional trees which can trap a huge amount of carbon dioxide from the atmosphere [35]. Research finds, the production of 1 ton of Kenaf dry matter needs 1.5-ton carbon dioxide [36, 37]. It means, it has a very high carbon density in it and can be able to replace wood as the source of biomass.

Kenaf has proved itself as a successful alternative crop by being incorporated into a wide range of value-added products. 35% of the kenaf plant is bast fiber which makes it suitable for paper and textile-based industries [38]. Historically, kenaf is being used as ropes, canvas, sacking, and animal feeds where recently, kenaf has started to become a reliable alternative raw material of wood which has paved us to a bypass to avoid the mass destruction of forests and the habitat of wild animals. Besides, some other prospective scopes of kenaf lie in the manufacturing of woven and non-woven textiles, and industrial absorbents to soak oil spills. Apart from the aforementioned significance, kenaf is also regarded as an excellent reinforcement material in composite industries owing to its considerable amount of toughness and high aspect ratio compared to many other natural fibers. A single strand of kenaf microfiber can possess a tensile strength and axial elastic modulus as high as 11.9 GPa and 60 GPa, respectively [39]. Rowell et al. [30] have performed a comparative study between different fibers reinforced polypropylene composites to assess the potential of kenaf as a reinforcement. The results have been listed in Table 1.1 which supports the excellency of kenaf fiber [40]. On the other hand, kenaf core fibers can be used in animal bedding, summer forage, and potting media [41].

Table 1.1. Microfiber size and chemical content of kenaf stem [40].

Filler/ reinforcement in PP	Units	Neat PP	Kenaf	Glass	Talc	Mica
Filler by weight	%	0	50	40	40	40
Filler by volume	%	0	39	19	18	18
Specific gravity	–	0.9	10.7	1.23	1.27	1.26
Tensile modulus	GPa	1.7	8.3	9	4	7.6
Specific tensile modulus	GPa	1.9	7.8	7.3	3.1	6.0
Tensile strength	MPa	33	65	110	35	39
Specific tensile strength	MPa	37	61	89	28	31
Flexural modulus	GPa	1.4	7.3	6.2	4.3	6.9
Specific flexural modulus	GPa	1.6	6.8	5.0	3.4	5.5
Elongation at break	%	10	2.2	2.5	–	2.3
Notched Izod impact	J/m	24	32	107	32	27
Water absorption (24 h)	%	0.02	1.05	0.06	0.02	0.03

However, several issues affect the performance of kenaf as a reinforcement in the matrix of the composite. The major problem encountered is the poor interphase bonding between matrix and kenaf reinforcement which induces weaker composites [41-43]. Besides, it has a problem of water absorption which leads to humidity aging in long term [44]. Nevertheless, there are chemical treatment procedures that can effectively reduce the flaw where still research is going on to find a solution to chemically treat kenaf in an optimized way [45]. This chemical modification or treatment of the natural fibers is mainly carried out to bind different functional groups with the hydroxyl group of the fibers using reagents to facilitate bond formation with the matrix of the composite.

1.3. Superiority of kenaf over other natural fibers

Compared to other natural fibers, kenaf is on a more propitious ground for having several advantages. Firstly, the spectrum of weather and geographical condition to grow kenaf is vast. The basic requirement for its growth is mainly well-drained and fertile soils with a neutral pH. However, it can withstand late-season flooding, drought, low soil fertility, and a wide range of soil pH values [46]. Besides, it can survive within the temperature 11.1-27.5°C and in the pH

limit between 4.3 and 8.2. The range of tolerance of annual precipitation for kenaf is between 57 to 410 cm. Kenaf is a highly daylight sensitive plant. The flowering starts when the photoperiod is less than 12.5 hr/day. It has been grown successfully as a crop as far north of North America as Indiana, Iowa, Kansas, and Nebraska [47].

Secondly, it's yearly yield and growth rate is appreciably high as it can grow as much as 10cm/day under optimal conditions, and has approximately a 3 month growing period from planting to harvesting [48]. Besides, kenaf is often compared to hemp as both of them have the potential to make significant advancements in future composite materials and high yield rate and stem production per year [49]. Additionally, hemp has drug value that makes it illegal to cultivate hemp in many regions of the world [50]. On the contrary, kenaf does not have any drug value like hemp which makes it easy to grow without any legal issues [51]. Moreover, along with a wide growing zone, kenaf is also found to have excellent overall feasibility [52].

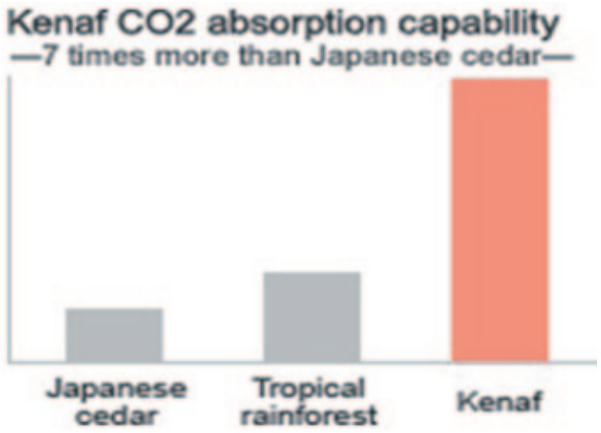

Figure 1.6. Comparison of CO_2 absorption [53].

Thirdly, Kenaf has a very high CO_2 absorption capacity. Unlike other C_3 crops, its photosynthetic and assimilation capacity are very high which can reach 32–37 $\mu molm^{-2}s^{-1}$. The net assimilation rate can even increase with the increase of Nitrogen in the leaf [54]. This high-efficiency CO_2 assimilation has led kenaf and its industrial end-products to be known as carbon

dioxide sinks in addition to making it a high biomass crop [55]. Figure 1.6 shows a comparison between conventionally accepted high CO_2 absorbents when kenaf is found to absorb an enormously higher amount of CO_2 [53].

Fourthly, the requirement for pesticides and fertilizers is relatively lower in comparison to other plants [56]. Low fertilizer (N-P-K) inputs are enough to grow kenaf in non-muddy soil of pH 5.7 – 8.2 [57]. It has been reported that kenaf competes with weeds very well once the plants are of sufficient size to shade the ground. As this plant grows very fast to reach that size, weed control is needed for the small initial period [58].

Finally, Kenaf has a magnificent set of mechanical properties which makes it superior to a lot of other natural fibers. More excellent and attractive properties have been exhibited by kenaf reinforced polymeric composites materials under flexural loading circumstances in comparison to the other similar type of natural fibers. Table 1.2 shows a comparative study between different popular natural fibers where kenaf is found to possess the highest elastic modulus [59]. Therefore, currently, kenaf is an auspicious option for the industries to manufacture biodegradable, low-cost, and environmentally friendly composite materials with splendid mechanical and structural performance [35].

Table 1.2. Comparison of specific gravity and Young's modulus of wood fibers with those of other natural and man-made fibers [59].

Fiber	Specific Gravity	Fiber Young's Modulus (GPa)
Spruce Kraft	1.2	40.0
Pine Kraft	1.2	31.7
Birch Kraft	1.2	37.9
Eucalyptus Kraft	1.2	34.8
Single Cellulose	1.5	100
Cotton	1.5-1.6	5.5-12.6
Jute	1.3-1.45	13-55
Flax	1.43-1.52	27.6-45
Hemp	1.47-1.50	50
Kenaf	1.5	53
Ramie	1.5	39.2-128
Sisal	1.5	9.4-22

1.4. Structure of kenaf microfiber

There are three parts of the stem of the kenaf plant: bast, core, and pith. The cross-section of the kenaf plant is illustrated in Figure 1.7 [60]. Kenaf fibers are mainly collected from bast which has been reported to have an excellent elastic modulus compared to the other parts of the plant [15, 61].

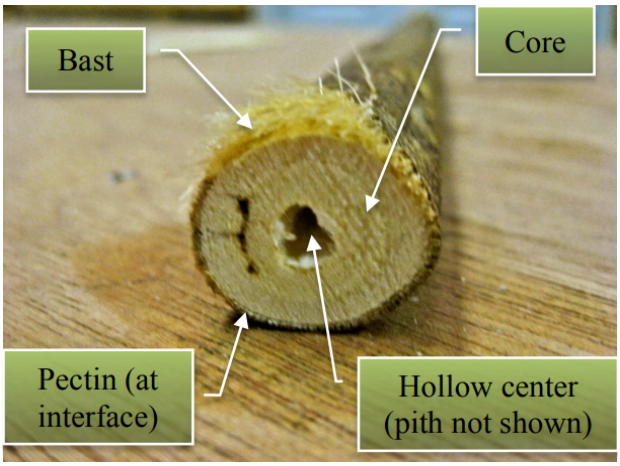

Figure 1.7. Cross-section of kenaf plant [60].

Kenaf filaments are composed of discrete individual fibers with lengths ranging from 2–6 mm. Filaments and individual fiber properties can differ depending on sources, age, method of separation, and history of the fibers. Bast and core can be separated easily by chemicals and/or by enzymatic retting. The bast has a denser structure than the other parts of the plant where the core has a wood-like structure [38]. The other way to differentiate the core from bast is the crystallinity. Where the bast has a more crystalline structure, the core is almost isotropic [15]. The kenaf fibers are also known as bast fibers, microfiber, or primary/elementary fiber [34]. The size and the constituents have been listed in Table 1.3 which proves the economic significance of bark [62].

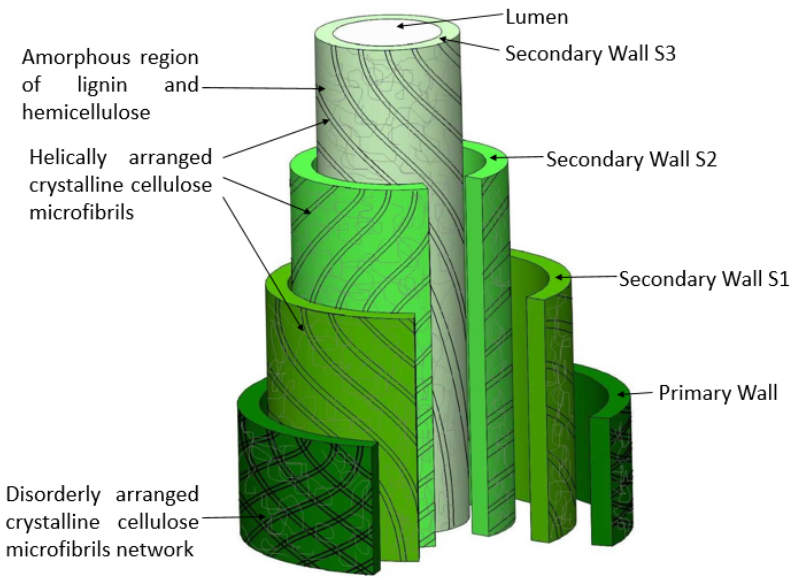

Figure 1.8. Schematic of a kenaf bast fiber with primary and secondary layers composed of S1, S2, and S3.

Table 1.3. Macrofibril size and chemical content of kenaf stem [62].

Parameters	Bark	Core
Fibril Length, L(mm)	2.2	0.75
Fibril Length, W (μm)	17.34	19.23
L/W	128	39
Lumen Diameter (μm)	7.5	32
Cell wall thickness (μm)	3.6	1.5
Cellulose (%)	69.2	32.1
Lignin (%)	2.8	25.21
Hemicellulose (%)	27.2	41
Ash content (%)	0.8	1.8

However, most of the bast fibers extracted from nature have a similar structure like kenaf what has been shown in Figure 1.8. It also depicts, the cellulose nanofibril is oriented at a certain angle with the vertical. This is one of the most vital things which vary among fibers and influence the overall mechanical properties. This angle is called a microfibrillar angle which can vary between 2° and 49° depending on plants. The smaller the angle is, the greater the elastic modulus in the axial direction becomes. For kenaf fiber, this angle varies between 9° and

15° based on growing conditions [63]. It can be considered as a strong reason for the appreciable mechanical properties of kenaf fiber [64]. It implies, there is a certain contribution of cellulose fibrils that actively influences the mechanical properties of the bast fibers of different plants.

1.5. Cellulose nanofibril

Cellulose nanofibril (CNF) is the fundamental unit of almost all types of natural fibers extracted from plants and is regarded as one of the main factors that influence their mechanical properties. It is mainly synthesized in plants but is not limited to plants. There are also certain bacteria which are capable of producing the polysaccharide. However, Acetobacter xylinum is the most extensively researched bacteria for cellulose synthesis. The anticipated biological significance of cellulose produced by bacteria is to assist in flocculation or to maintain a particular environment, e.g. aerobic conditions. It can also ease the attachment to plants [65]. Figure 1.9 shows the hierarchy that descends to cellulose nanofibril starting from microfiber of natural fiber.

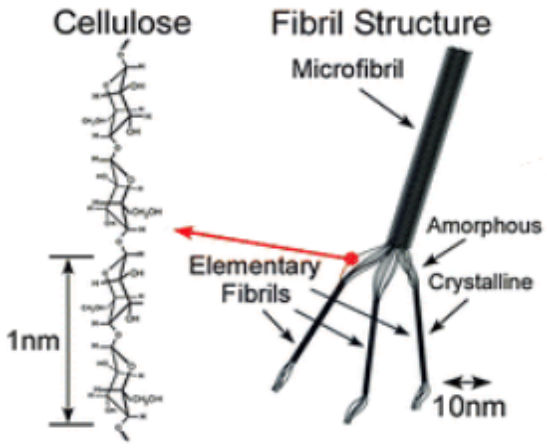

Figure 1.9. Hierarchy of structure in natural fiber [65].

With the development of nanotechnology, it has become possible to extract CNF from plants recently [66]. There are two common ways to extract CNF: from plants and bacteria. Cellulose from plant sources can be extracted by Chemical solubilization-type processes, e.g.

pulping, which are used to extract CNF from plant sources which makes it possible to obtain a refined structure of CNF. The cellulose structure is broken and the remaining portion of CNF in solution is collected as precipitation. This is how regenerated cellulose is prepared [67]. Recently, bacterial cellulose (BC) has become a reliable source of CNF. BC is manufactured with the help of oxidative fermentation by acetic acid in both synthetic and non-synthetic medium. *Acetobacter xylinum* is the most popular bacteria for its supreme efficiency as a BC producer which can manage the assimilation of different types of sugars and produces excellent quality of cellulose in liquid medium [68-70]. However, the challenge of BC is the high cost and low yield production which has shrunk down the industrial production of BC and its commercial application. Hence, researchers are still working to find a new cost-effective carbon source with a shorter fermentation process for high yield BC production to make this process feasible [71].

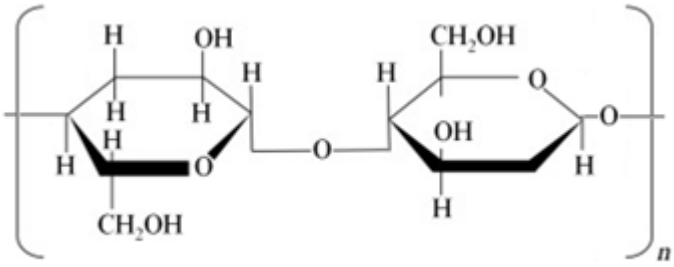

Figure 1.10. Structure of cellulose.

The structure of cellulose is illustrated in Figure 1.10. Cellulose has a chain structure consisting of numerous pyranose units (Dextro glucose) along the axial direction. Two units of pyranose are sigma covalent bonded with oxygen (glycoside linkage) [72]. Cellulose chains agglomerate as microfibrils or bundles of polysaccharides that are arranged in fibrils. In addition to making plant structures stable, this arrangement indicates the high strength and other superior mechanical properties of cellulose.

Cellulose and cellulose-based products are being used for a pretty long time. All the natural fibers currently being used commercially contain cellulose. Hence, cellulose is one of the most important ingredients of paper and paper products as well as textiles which rely on cotton, linen, and other plant fibers [73]. Microcrystalline cellulose is used as a filler, both in the pharmaceutical and food industries. Cellulose can also be converted into some other commercial products like cellophane or nitrocellulose for photographic and household applications, respectively, as well as military industries. Besides, recently, Nanocellulose or nanocrystalline cellulose is gradually getting more popularity in several exclusive applications. The properties of nanocellulose make it suitable for applications, such as, in photonics or optoelectronics. Crystallized nanocellulose has a huge prospect as a raw material in the food packaging and electronics industries. Additionally, nanocellulose can be derivatized and functionalized easily with a wide range of chemical functional groups to introduce different kinds of bonds in polymer and composite materials. For example, esterification of nanocellulose can enhance the hydrophobicity and strength of the material, while cationization can strongly influence pH sensitivity to nanocellulose allowing CO_2-controlled flocculation. However, as like many biopolymers, nanocellulose applications are limited because of their less feasibility [74]. Hence, because of having such promising applications, it has become important to know more about cellulose nanofibril and make it more feasible.

1.6. Research on mechanical properties of cellulose nanofibril

As CNF is offering a promising prospect in the next generation nanocomposites, it is important to know the mechanical properties of CNF comprehensively to use it potentially in nanocomposites [75, 76]. Researchers have studied CNF in different aspects. At the beginning of the last century, Nishikawa and Ono found performed X-ray diffraction on wood, hemp, and

bamboo finding the first X-ray diffraction traces [77]. From the traces, they were able to publish some X-ray diffraction patterns of cellulose fibers which led to the proposal of several cellulose structures. In 1928, Meyer and Mark made a significant advancement in the molecular models of cellulose by revising the previous model [78]. They successfully managed to provide a realistic molecular description of the glucosyl rings in an antiparallel two-chain monoclinic unit cell. Later, some other modified models were proposed where the adoption of the 'bent' C_1 chair configuration was shown to be a result of the interaction of intramolecular hydrogen-bonding after the glucosyl moieties [79-82]. Nevertheless, two chains of monoclinic unit cells were not sufficient to resolve electron diffraction diagrams from highly crystalline cellulose. Besides, there was a controversy in the correctness between the eight chain unit cell and the disordered structure [83].

After 1974, a major development has been brought about in computer methods in model building. Sarko and Blackwell, with their computer-based model, simulated the structures that were well aligned with the available experimental data for native cellulose and other allomorphs [84-86]. The researchers asserted that monoclinic unit cell with two parallel and conformationally equivalent chains can be used to model cellulose I successfully. The main chain is placed at the corner of the unit cell parallel to the direction of the c-axis where the center chain goes through the center of the a/b plane and is translated along the c-axes direction by about c/4 with respect to the original chain. In contrast to the determined "parallel down" direction of the chains by Gardner and Blackwell, the other group, Sarko and Muggli determined it along "parallel-up" the direction [84, 85].

Though the researchers have accepted most of the parts of these structures, with the development of 13C CP/MAS solid-state NMR, the remaining details have faced strong

contradictions. This technique unraveled some surprising details of highly crystalline cellulose I which could be described only by a consisting of two completely separate crystal phases system. The system has been identified as Iα and Iβ which is also related to the cellulose origin [87]. Where Iα am prevalent in Valonia and bacterial cellulose, Iβ dominates in the formation of tunicate (*Halocynthia roretzi*) or animal cellulose [88, 89]. Consequently, the idea of cellulose I collapsed where the two new cellulose structures, Iα and Iβ got established. It implies there could be a possibility to find the structures by refining X-ray diffraction patterns collected from highly crystalline mixed-phase cellulose sources, e.g., Valonia which can be distinguished into Iα and Iβ subdiagrams. Alternatively, collecting diffraction data from Iα and Iβ containing the sample was another way. However, researchers found the second option more convincing because of the advancements in sample characterization. Additionally, uncertainties in separating overlaid diffraction features from mixed-phase cellulose is another reason to prefer the second method. Utilizing the X-ray electron diffraction technique, Sugiyama et al. characterized the space group and chain packing of the Iα and Iβ cellulose [90, 91]. They discovered the single strand triclinic unit cell of Cellulose Iα where cellulose Iβ has a double parallel stranded monoclinic unit cell similar to the approximate proposed unit cell for cellulose I by Gardner and Blackwell and Sarko and Muggli [84, 85]. Later, the proposed “parallel-up” chain-packing organization by Sarko and Muggli was proved by the development of the electron microscope [92]. These results encouraged the next generation researchers to reveal elaborate molecular descriptions for Iα and Iβ to be by modeling studies [93-97]. Valonia cellulose has also been experimented with to determine cellulose Iβ structure from its X-ray patterns [98]. Nevertheless, Nishiyama et al. found no instance of atomic coordinates using diffraction data collected from samples of pure Iα or Iβ phase. They aligned cellulose microcrystals from tunicin to yield-

oriented fibrous samples which were later subjected to synchrotron and neutron diffraction. They mainly focused on the Iβ phase of cellulose and explored its crystal and molecular structure. Besides, they were able to determine the hydrogen-bonding system in cellulose Iβ. The X-ray data estimated the positions of the C and O atoms. Figure 1.11 shows the parallel strands having slightly different conformations comprise the resulting structure which follows *t-g* conformation organizing in sheets packed in a "parallel-up" fashion, with all hydroxymethyl groups [99].

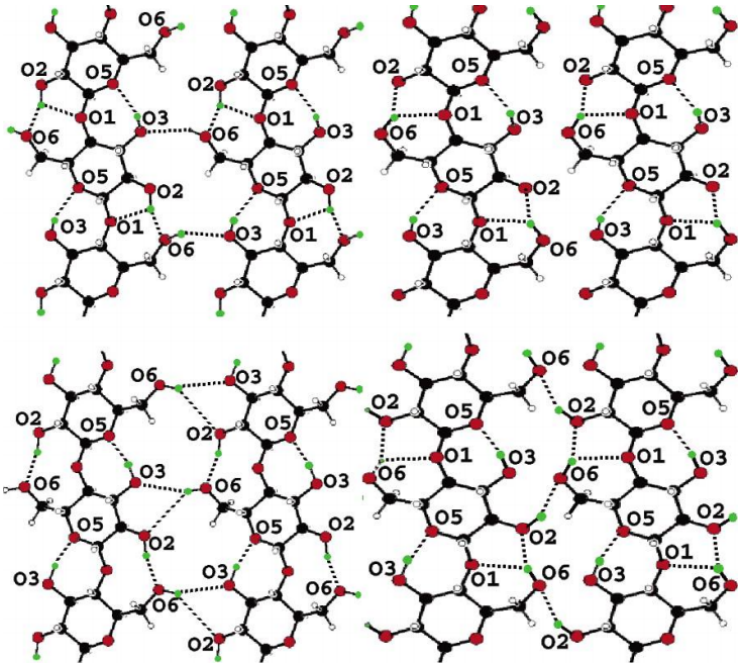

Figure 1.11. Schematic of cellulose Iβ showing the hydrogen bonds in the origin and center sheets. C, O, H atoms and deuterium molecules are illustrated with the color black, red, white, and green, respectively. The dotted line shows the hydrogen bond present in the chain [99].

In the later years, Nishiyama proceeded further to explore the structure and properties of the cellulose microfibril. He considered cellulose microfibril as a single-stranded highly anisotropic slender and long crystalline entity. He performed different characterization, e.g., electron microscopy, infrared spectroscopy, X-ray scattering and diffraction, solid-state nuclear magnetic resonance spectroscopy, and molecular modeling to reveal the structure and mechanical properties. He determined Young's modulus of the crystalline domain by performing

uniaxial tensile loading along the fiber axis and measured the lattice deformation along the chain axis with the help of X-ray diffraction. In these tests, bulk specimens having parallelly aligned cellulose microfibrils bundles (e.g. flax) are loaded along the axis of the fiber. The tiny axial strains in the cellulose structure is measured in XRD to determine elastic modulus. Direct measurement of Young's modulus was additionally made by applying the sound velocity and density relation. The X-ray or neutron scattering can probe the density–density correlation in time and space and using this property, the velocity of sound while passing the lattice can be determined. The signal is influenced greatly by the direction and the structure factor of the substrate. Taking the advantage of this technique, he estimated Young's modulus in the direction perpendicular to the hydrogen-bonded plane as 14.8 ± 0.8 GPa [100]. Besides, Diddens et al., Matsuo et al., and Sakurada et al. measured axial elastic modulus between 120-138 GPa [101-104]. Researchers have also used inelastic X-ray scattering (IXS) of cellulose microfibrils. Here, the sound velocity is used as a function of acoustic phonon dispersion through the crystalline regions and unlike the XRD method, it disregards the perfect load transfer issues [101]. Through this process, the axial elastic modulus was found larger (220±50 GPa). Besides, the transverse elasticity was also measured which is 15 ±1 GPa. However, a perfect load transfer and orientation of cellulose crystal in the microfibril axis of loading is important in this procedure. As the condition is difficult to achieve, the properties estimated in this procedure can have errors. Additionally, XRD and IXS procedures are particularly limited to CNC and can be invalid for microfibrils. So, the extraction procedure can have a significant influence on the result.

Lahiji et al. combined high-resolution AFM indentation and finite element modeling to measure individual wood CNC and measured the transverse elastic modulus [105]. AFM experiments were performed to image CNC in a high-resolution dynamic mode where jump-

mode measurements were adopted on individual CNCs under ambient conditions with 30% relative humidity (RH) and under a nitrogen atmosphere with 0.1% RH. Figure 1.12(a) shows a representative 2D dynamic-mode AM-AFM image of CNC of length 220 nm on a mica substrate where Figure 1.12(b) is a 3D image. Figure 1.12(c) depicts the height profile. In the experiment, they measured the transverse elastic modulus as between 18-50 GPa.

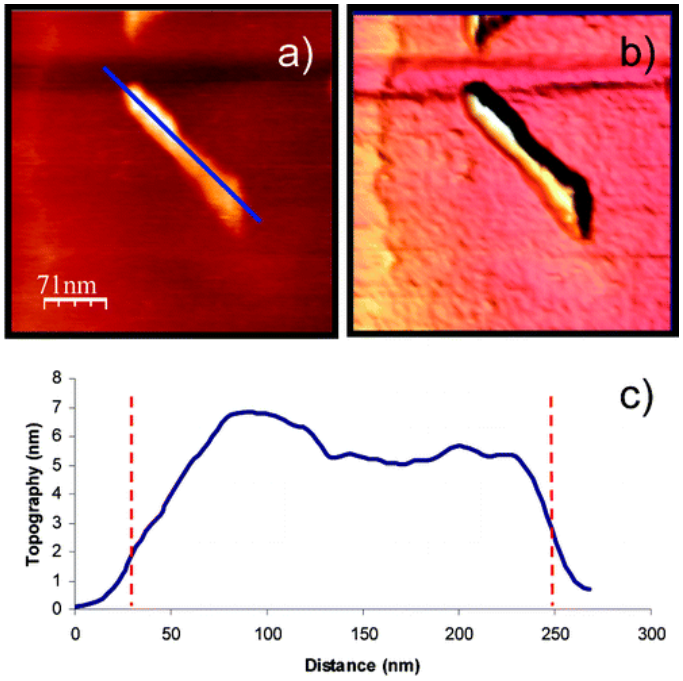

Figure 1.12. (a) AM-AFM 2D image of CNC. (b) 3D image of CNC (c) Height profile of line along the length of the CNC [105].

Paavilainen et al. used atomistic molecular dynamics-based simulations to explore the structure of cellulose nanofibrils designing in such a way that is comparable with the available commercial nanocellulose [106]. The simulations found the influence of temperature on the twisting of the cellulose chain's rate of relaxation without affecting the bending or stretching of nanocellulose. Taking the atomic-scale interaction patterns into account, they discovered the fact that the observed twisting stems from the hydrogen bonding within and between the chains in a nanofibril. The left diagram of Figure 1.13 shows the Cross-section of the 59-chain cellulose nanofibril after 140 ns simulation at 310 K. The three highlighted chains at the different sides of

the cross-section are easing the visualization of the twisting caused by chain reorientations. The front end is the reducing end of the chains.

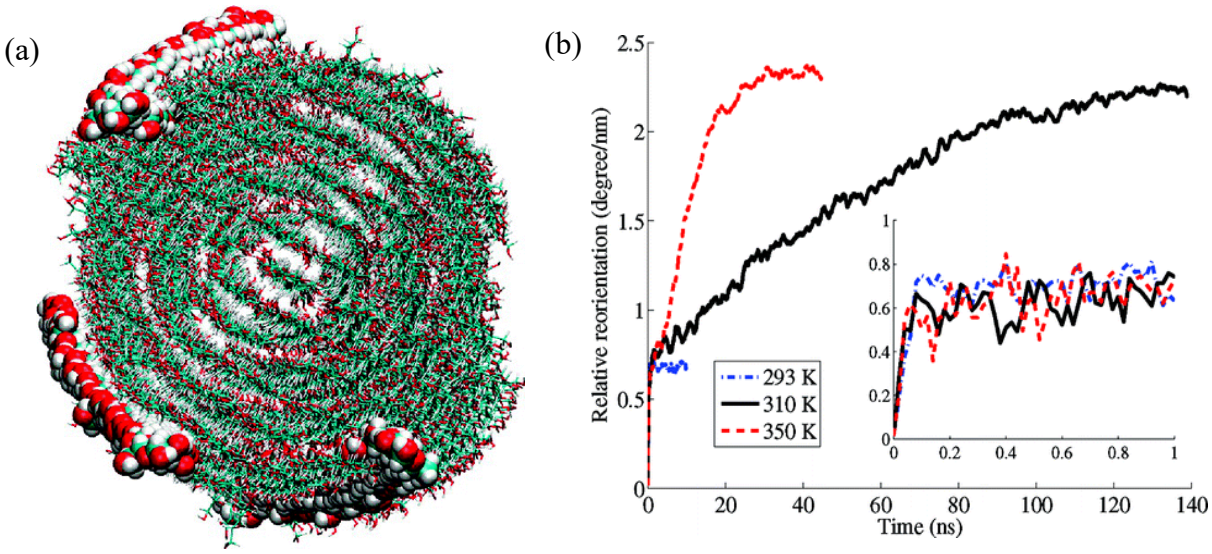

Figure 1.13. (a) Cross-section of the 59-chain cellulose nanofibril after 140 ns simulation at 310 K. (b) Average twisting evaluated as the reorientation of a chain divided by its distance from the middle chain, plotted as a function of simulation time at 293, 310, and 350 K. The inset depicts the first nanosecond of the simulations which contains some instability (Right) [106].

The right diagram displays average twisting measured as the reorientation of a chain divided by its distance from the middle chain plotted as a function of simulation time at 293, 310, and 350 K. It shows, the twisting is extremely slow at 293 K with no sign of change noticed within 10 ns whereas, at 350 K, the reorientation is significantly high which reach 2.3 degrees/nm reorientation within 30 ns. Largely homogeneous distribution of reorientations can be easily observed for the data at 310 K after 140 ns. The first nanoseconds of the simulations have been illustrated in the inset. Though the data are not stable, it gets smoother as the time elapses. Another noticeable fact is the reorientation during the first nanosecond has no dependence on temperature. The researchers also found the relative twisting for different cellulose chains to vary in the range between 2.08 and 2.47 degrees/nm where larger values were noted at the surface and in the corners of the nanofibrils [106].

Sturcova et al. applied an in-situ combination of tensile test experiments and Raman spectroscopy to determine the axial elastic modulus as 143 GPa for the crystalline form of cellulose, i.e., t-CNC [107]. A thin t-CNCs mat was used with epoxy and this composite material was subjected to a tensile test. Raman spectroscopy was engaged to find the shifts in the characteristic curve's peak for the sample. It helped to determine strain along the axial direction of the crystal. Their micron-sized laser was able to sample several t-CNCs within a single stroke of measurement which led to the determination of axial elastic modulus. However, the experiment assumed perfect load transfer between the epoxy matrix and the t-CNC and t-CNC network was assumed 2-dimensional (2D). So, it is likely to have errors associated with this method which directly affect the result. A similar technique was followed by Rusli et al. where different values of axial elastic modulus were obtained based on the assumed network (2D or 3D) [108]. Their determined value was 57 GPA and 105 GPA for 2D and 3D network structure assumption respectively. The sample preparation was also different in this case. Figure 1.14 (a) shows an AFM image of the dispersed cellulose where the height information has been shown in a scale bar on the left hand is and the spatial resolution is shown in the bottom. The cellulose sample was dispersed in epoxy from which a bend bar specimen was cast which makes the distribution of cellulose in a 3D manner. The lower axial elastic modulus has resulted from the less efficiency of stress transfer between the epoxy matrix and cellulose particles for its smaller length. A Raman spectroscopy spectrum of cellulose marking 1095 cm−1 band's position has been shown in Figure 1.14 (b) where the inset presents the distribution of orientations.

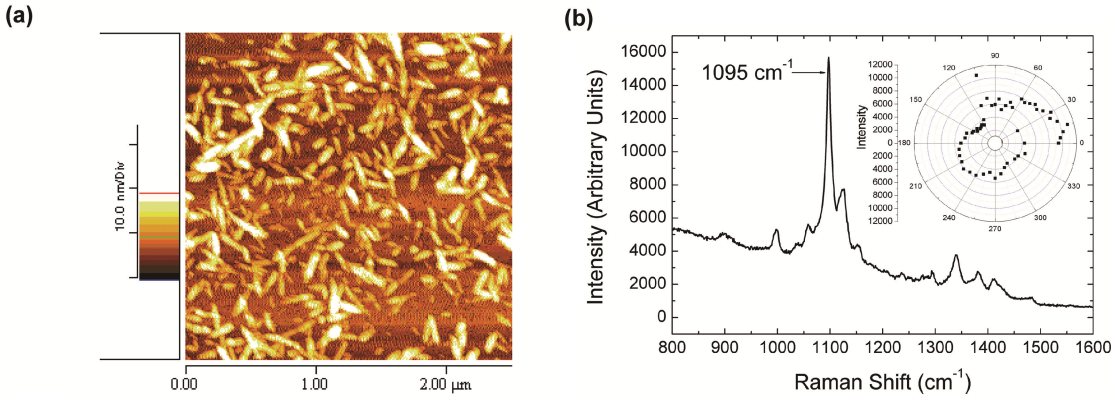

Figure 1.14. (a) AFM image of the dispersed cellulose whiskers. (b) A Raman spectrum of the cellulose whiskers depicting the 1095 cm^{-1} band position [108].

Literature shows some research on bacterial cellulose as well. Guhados et al. used AFM to determine the forces with sub-nanonewton sensitivity at the nanometer scale to measure the axial elastic modulus [109]. They modeled the experiment in such a way where the deflection was measured at a different point along with a fiber that was suspended over a 1.5 μm gap designed on a trenched micro fabricated Silicon wafer. Their measured value of axial elastic modulus 78 $\pm$17 GPa. They observed no relation of the modulus on the diameter of the fiber which is a good indication of the shear forces being unimportant and mechanical behavior of fiber like a homogeneous material.

Hsieh et al. presented a Raman spectroscopy-based technique to determine the Axial elastic modulus of a single filament of bacterial cellulose [110]. They implemented this procedure to measure the local molecular deformation of the cellulose through a shift century in the central position of the 1095 cm^{-1} Raman band which belongs to the glycosidic bond in the backbone of cellular structure. The calculation of shift rate with respect to applied strain yielded the axial elastic modulus of the single-stranded bacterial cellulose. They rotated the matrix of fiber through 360° and recorded the change of the intensity of 1095 cm^{-1} Raman band. They found no significant influence of the angle of rotation on the calculated intensity of the band

which indicated the random distribution of the network. Utilizing literature data and back-calculation of Krenchel analysis, this research group calibrated the Raman band shift for different axial elastic modulus to predict their result for a single fibril of bacterial cellulose. Their obtained value for axial modulus is 114 GPa which was higher than the existing literature values and also lower than the value estimated for the cellulose crystal which was between the range 130-145 GPa. They showed crystallinity and structural composition of the samples as the reasons for this discrepancy. According to this group, the main challenge to this characterization was the issues in measurement technique and the assumption used in the property calculation. Hereby, there are a good number of studies on cellulose and its derivatives which can be found in the literature.

Paavilainen et al. continued their study and experimented with the bare crystalline structure of CNF where they used wide-angle X-ray data for commercial nanocellulose [106, 111]. They used the results with previous studies of crystal structure by Nishiyama et al. to construct configurations for the fibrils initially. This group modeled the elementary fibrils of CNF atomistically which consisted of regions having 34 or 36 cellulose chains. The designed cross-sectional diameter of the fibril was about 3.4 nm. The model was simulated using atomistic molecular dynamics to investigate the mechanical properties of CNF in water and ethanol medium. The models on which the simulations were performed included both crystalline and non-crystalline regions. They accounted for non-crystalline regions to simulate the essentials parts of amorphous cellulose nanofibrils. They investigated with different numbers of connecting strands between the crystallites and depending on different numbers connecting chains between the crystallites, the elastic constants, inelastic deformations, and strength of the fibrils were investigated.

The calculation of the stress developed in the nanofibrils requires the cross-sectional area. Considering the research of Nishiyama et al., for 6x6 cellulose chains, the separation of chains was taken as 0.53 nm in the 110-crystal direction where 0.60 nm was the separation in the 110-crystal direction in the fibril [99, 100]. The angle between these crystal directions was taken as 93.5° degrees. Hence, the cross-sectional area was determined to be (6 x 0.53 nm) x (6 x 0.60 nm) x sin(93.5°) = 11.4 nm^2 . They used this estimation in all the calculations related to the stress. Figure 1.15 shows their atomistic model of cellulose that they used in their simulation. Two 10 nm long crystalline parts connected by 10 chains in the non-crystalline part comprise the fibril.

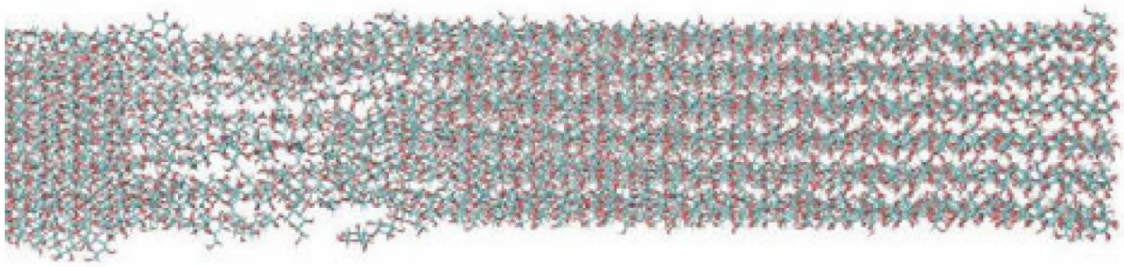

Figure 1.15. Atomistic model of a cellulose nanofibril [111].

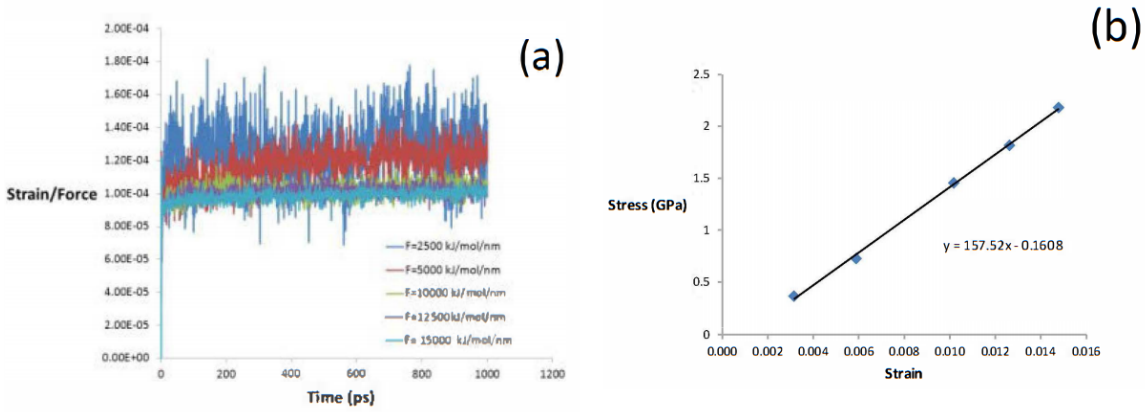

Figure 1.16. (a) The strain of the crystal region with time in water medium for different loads. (b) Stress-strain curve by averaging the strain for the period 3-1000 ps, with the cross-sectional area of the full single crystal with 36 chains [111].

The elasticity of the modeled nanofibrils was measured by applying a tensile load on them and strain response was collected. The constant load was varied between 2500-15000 kJ.mol-1.nm-1 which corresponded to 0.415-2.491 GPa for their study. The strain behavior found by this research group for the crystalline region of cellulose has illustrated in Figure 1.16 for the water medium. An interesting feature in Figure 1.16 (a) can be marked as the small gradual increase in strain with time in most cases. They found the value of axial elastic modulus as 157±4 GPa. They also studied the elasticity of the amorphous part of CNF with 3 and 10 connecting chains attached to the neighboring crystal CNF. For the amorphous part, the load was varied between 500 and 5000 $kJmol^{-1}nm^{-1}$. An example of the effect of the relatively large applied force on the fibril structure is shown in Figure 1.17 (a) where Figure 1.17 (b) shows the response of strain for the whole fibril. They found it easier to determine the strain for non-crystalline for the small bending of the fibril under an applied force. They assumed the same cross-sectional area that they used for the full single-crystalline CNF while calculating the axial elastic modulus. As the number of connected chains decreased, the elastic modulus also decreased. Besides, in Table 1.4 it is shown that it is possible to roughly predict the total elastic modulus of a bundle of CNF by assuming that each addition of the connecting chain increases 4 GPa to the overall value of axial elastic modulus. Figure 1.17(b) shows the strain of the fibril vs time curve for three connecting non-crystalline CNF chains at 5000 $kJmol^{-1}nm^{-1}$ stress level. In this case, the strain gets stability after 100 ps.

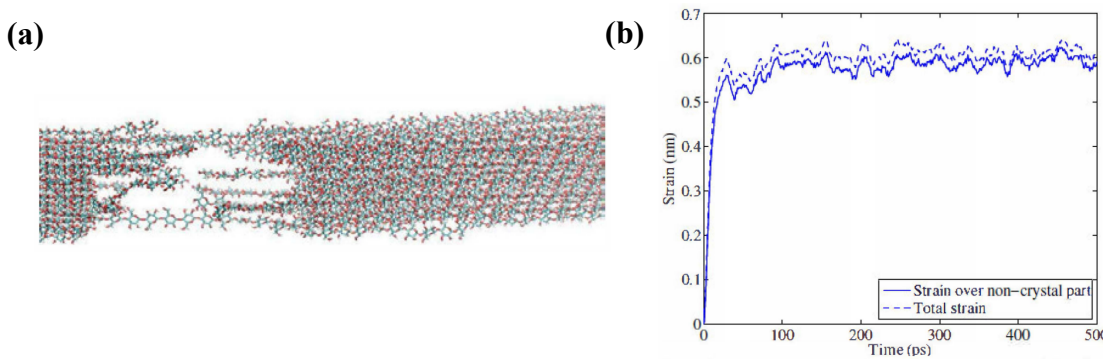

Figure 1.17. (a) 10 connecting chains of CNF under tension load of 15000 $kJmol^{-1}nm^{-1}$. (b) The strain of the fibril vs time curve of 3 connecting non-crystalline CNF chains at 5000 $kJmol^{-1}$ nm^{-1}stress levels [111].

Table 1.4. Axial Elastic properties of the CNF with 36 chains with a different number of connecting chains. The linearly extrapolated value of strain for vanishing stress is presented in the third column.

Number of connecting chains	E_{mod} (GPa)	E_{mod}/chain (GPa)	Strain at F=0 (%)
3	1 1 .9±0.2	4.0±0.1	0.29±0.06
10	54±2	5.4±0.2	0.16±0.04
36	157±4	4.4±0.1	0.10±0.04

Their study showed the effect of surrounding liquid which also influences in determining the axial elasticity of fibrils. For a similar condition as for water, the value of elastic modulus for the CNF was found as 41.0 ± 0.5 GPa by averaging strain for the time interval 6-500 ps (Figure 1.18 (a)) which is smaller than the value 54 ± 2 GPa for water. This result shows the effect of hydrogen bonding in the ethanol medium. By calculating the modulus from the three largest forces for 1300-1500 ps, they obtained the value of 39.7 GPa. The initial strain offset (0.008 ± 0.025%) disappears in Figure 1.18 (b), which indicates a primary power-law increase of strain is observed for all stress levels.

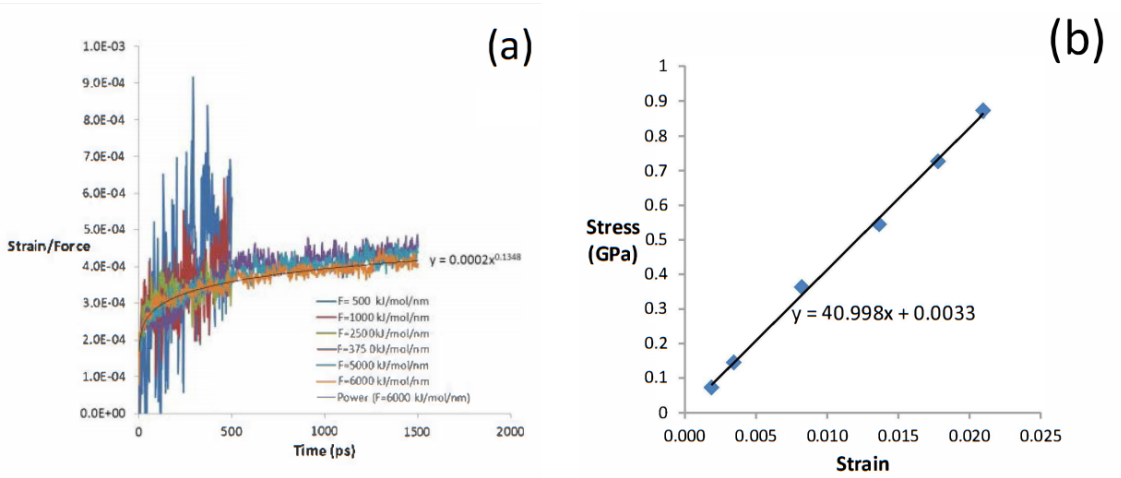

Figure 1.18. (a) Strain response with time for CNF (b) Stress-strain curve obtained by averaging the strain over a time period of 6-500 ps after the force was applied at time zero [111].

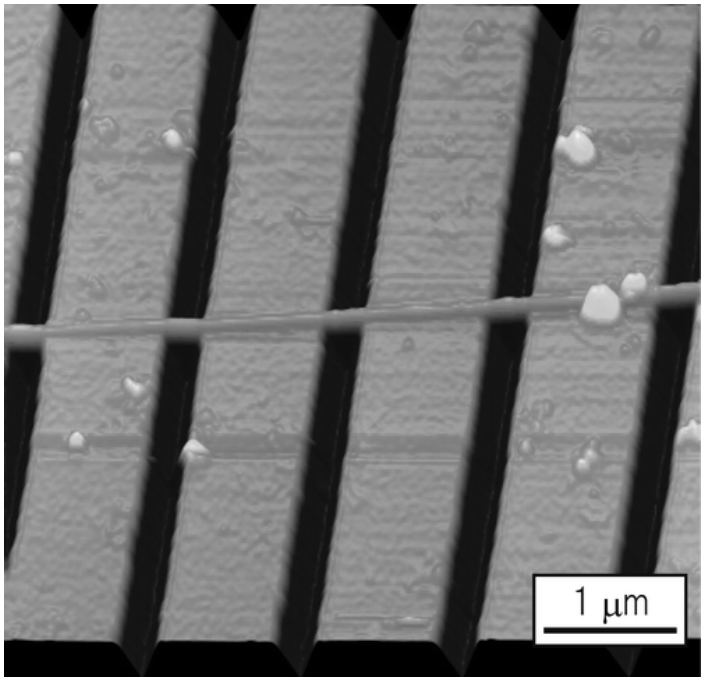

Figure 1.19. AFM images of the TEMPO-oxidation prepared cellulose microfibrils on the microfabricated silicon wafer [112].

Iwamoto et al. based on atomic force microscopy (AFM) based 3 points bending of Cellulose microfibrils to determine the axial elastic modulus [112]. They treated these microfibers by oxidation of cellulose with 2,2,6,6-tetramethylpiperidine-1-oxyl radical (TEMPO) and subsequent mechanical disintegration in water and by sulfuric acid hydrolysis. The

nanocellulosic materials were placed on a microfabricated silicon wafer in 227 nm width grooves and were subjected to a three-point bending test to determine the elastic modulus using the AFM cantilever. Figure 1.19 shows the AFM image of the test fiber and testing site. The axial elastic moduli of single cellulose microfibrils treated by TEMPO-oxidation and acid hydrolysis were found as 145.2 ±31.3 and 150.7 ±28.8 GPa, respectively (Figure 1.20). The result proved the similarity of the experimentally determined modulus of the highly crystalline tunicate microfibrils and the elastic modulus of native cellulose crystals. However, the result may not be reliable as Euler-Bernouli beam formula was used for the dwarf beam where Timoshenko beam could be a better fit.

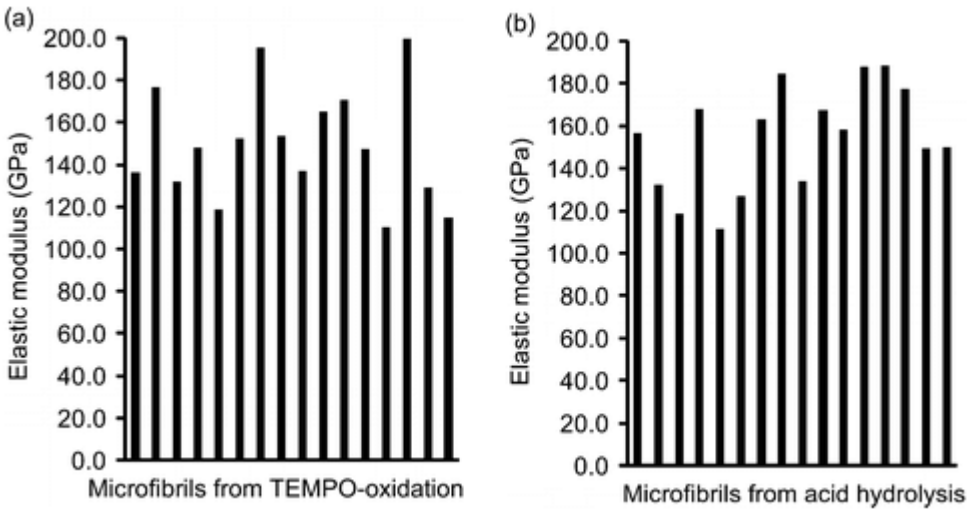

Figure 1.20. Axial elastic modulus of cellulose microfibrils treated by (a) TEMPO oxidation and (b) acid hydrolysis [112].

Cheng et al. performed AFM-based 3 points bending similarly [113]. However, this group focused on the nanoscale CNF which was subjected to a nanoscale three-point bending test to measure the axial elastic modulus. They marked several factors that influenced the determine the deflection of the fibril, e.g., data mining, AFM probe selection, and the testing position of the reference material, the different stiffness AFM probe. The measured deflection can strongly

affect the determined value of the axial elastic modulus. So, they calibrated their calculation to suppress the effect of these issues. Figure 1.21 (a) shows the schematic of the test where Figure 1.21 (b) shows the positions of the probe during the test.

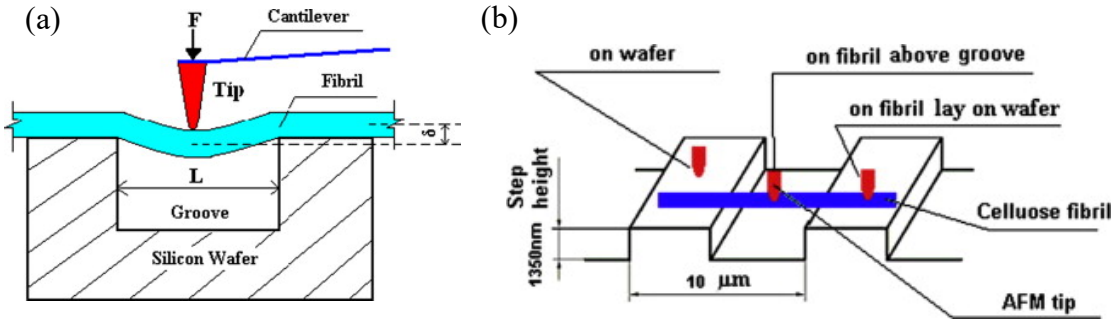

Figure 1.21. (a) Schematic of the test set-up and (b) Positions of the AFM probe during the test [113].

An indentation was made on the wafer and the Force versus Deformation (F-z) curve was combined with the F-z curve of 3 points bending on CNF. Figure 1.22 shows the combined curve to find the deflection of the CNF due to the force exerted by the AFM probe.

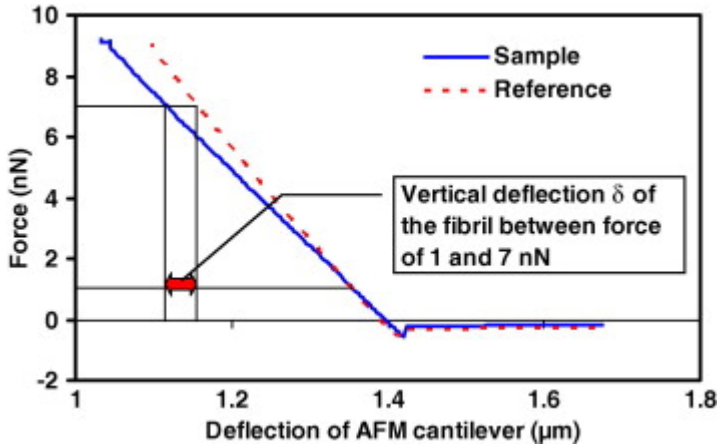

Figure 1.22. AFM F-z curve to find the deflection of CNF [113].

They used the Euler beam formula and considered a circular cross-section of the fiber. In their research, they measured the axial elastic modulus of CNF with a diameter of 270 nm as 93 GPa.

1.7. Research on mechanical properties of kenaf

Though researches on kenaf microfiber reinforced polymers and their mechanical properties were scant until 2011 and were limited to a few studies [61, 114], presently, comprehensive researches are being conducted. These researches mainly focus on finding an optimal combination of kenaf in synthetic polymeric matrices [115] and determining the mechanical properties e.g. tensile strength, Young modulus, and flexural strength [116]. The researchers have investigated the kenaf composites with HDPE [117], Polyester [118], Polypropylene [119], etc., to have outstanding mechanical properties which also sometimes vary based on the method of testing, growing condition, and whether the fibers have been chemically treated or not.

In order to engage kenaf fiber as a reinforcement material more potentially, it is necessary to understand the mechanical properties of kenaf microfiber more accurately and comprehensively. Despite performing numerous researches on kenaf composite's mechanical properties, there is a dearth of ventures to investigate the mechanical properties, particularly for kenaf microfiber.

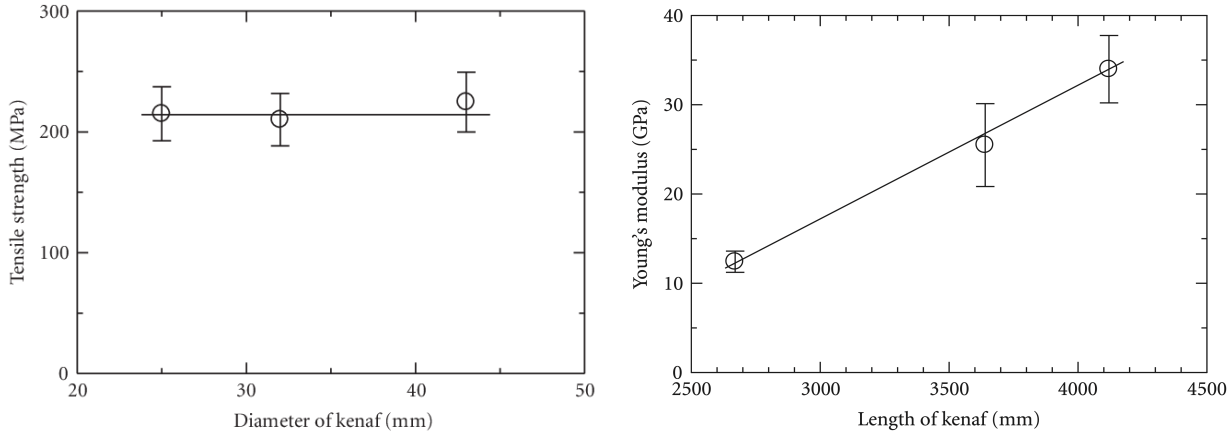

Figure 1.23. (a) Tensile strength of different diameter kenaf microfiber; (b) Young modulus of kenaf fiber for different length of kenaf [120].

Shinji performed a tensile test on a kenaf fiber bundles with varying kenaf diameters between 20-45 mm and found tensile strength about 215MPa [120] (Figure 1.23 (a)). He found no significant change in tensile strength while changing the fiber bundle diameter. On the other hand, in Figure 1.23 (b), their result shows a varied Young's modulus, i.e., axial elastic moduli, between 12-33 GPa for different plant height. Shibata has stated the axial elastic modulus of kenaf is 22 GPa [121] and Cicala et al. has found it as 10.94 GPa [122]. On the other hand, other researchers have shown the axial modulus of kenaf in the range between 21-60 GPa [15, 123, 124] [125].

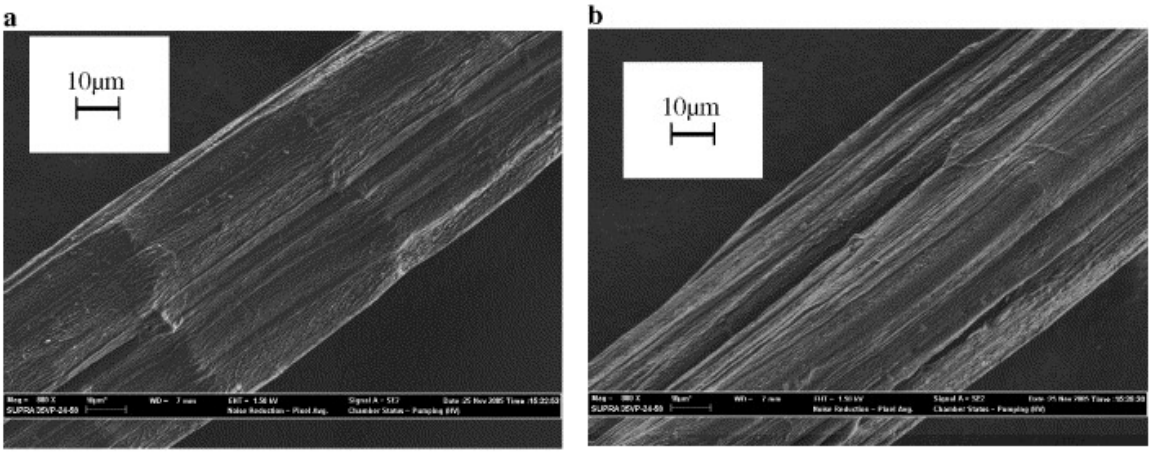

Figure 1.24. SEM micrograph of (a) an untreated kenaf fiber and (b) 3% NaOH treated kenaf fiber [43].

Edeerozey et al. modified kenaf microfibers with NaOH and the SEM micrograph of fiber has been illustrated in Figure 1.24 for the treated and untreated condition. The highest tensile strength of a bundle of kenaf microfiber was found as approximately 243.7 MPa for 6% water bath treated sample [43] as shown by Figure 1.25. So, based on the literature, most of the elastic moduli of kenaf microfibers were determined for a bundle of fiber that has the chance to contain errors. So, it is necessary to investigate the elastic moduli for a single fiber what makes it necessary to further expedite to determine the correct modulus.

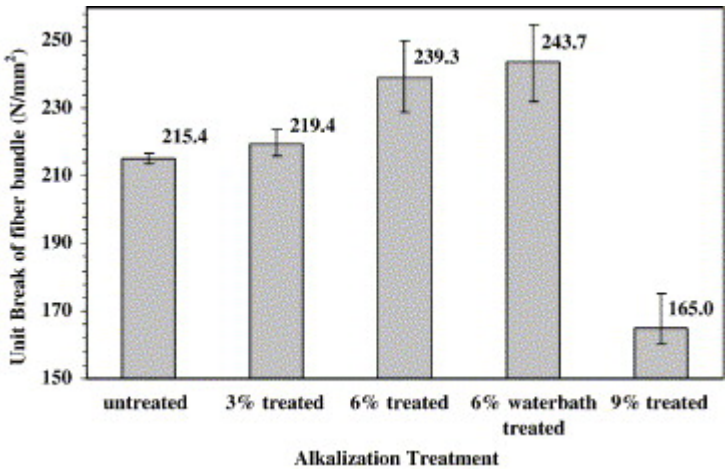

Figure 1.25. Tensile strength for kenaf microfiber bundle for different treating conditions [43].

2. SIGNIFICANCE OF PERFORMED RESEARCH

Literature shows the increasing commercial significance of kenaf microfiber and CNF which makes it important to explore the mechanical properties accurately to apply in next-generation structural materials correctly. Hence, one of the primary goals of this research is to find the elastic modulus of kenaf microfiber and CNF. Elastic modulus is one of the most important mechanical properties of a material which strongly influences shear modulus, Poisson's ratio, and torsional strength [126, 127]. There are two major reasons for what further study is needed to estimate the mechanical properties of kenaf microfiber and CNF more accurately. The reasons have been discussed downwards.

2.1. Error for considering bundle of fibers for testing

A handful of research have been done already on the elastic properties of kenaf microfiber and CNF. Unfortunately, most of the previous studies have performed studies on a bundle of fibers to determine the elastic modulus which is an erroneous process due to the following reasons:

2.1.1. Determination of incorrect diameter

It imposes a great challenge to know the real diameter of the bundle of fibers due to the presence of the void. In Figure 2 (a), a fiber bundle has been depicted with 75 fibers where each fiber has 0.23 mm in diameter. The diameter of the bundle is about 2.3 mm. So, mathematically, there are about 25% void spaces in the bundle which is shown in Figure 2(b). Hence, the determination of the correct diameter will be difficult and if the bundle diameter is regarded as the diameter in the tensile test, it is more likely to find an incorrect modulus.

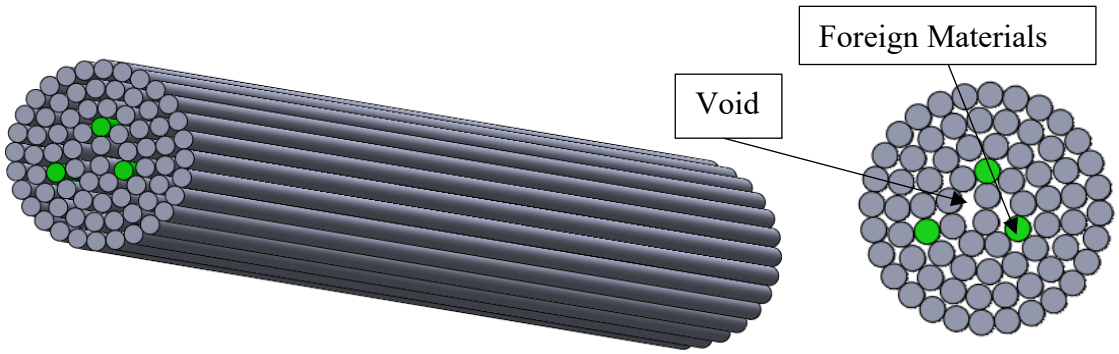

Figure 2.1. (a) Schematic of a bundle of fiber. (b) The cross-sectional view of the fiber bundle. Fibers in green representing the presence of foreign materials.

2.1.2. Presence of foreign materials

The existence of foreign material poses as a great hindrance to determine the accurate elastic moduli. The fibers in green color in Figure 2.26 show the presence of foreign material in the fiber bundle which can affect the test result. For example, kenaf microfibers are glued together by other non-cellulosic materials such as lignin and hemicellulose which form continuous strands [124]. So, considering a bundle of kenaf can bring error in the experimental results.

2.1.3. Determination of incorrect gauge length

Due to the waviness of the fibers, it is unlikely to get all the fibers straight and aligned. Besides, there are discontinuities in the fibers. It makes the measurement of the gauge length very hard in the bundle basis testing of kenaf microfiber.

2.1.4. Possibility of nanoindentation at incorrect location

Several instances of nanoindentation have been found in the literature aiming to find the transverse elastic modulus of fibers [105]. However, considering a bundle of fiber increases the possibilities of the nanoindentation between two fibers or in an incorrect location.

2.2. Limited study of transverse elastic modulus

Kenaf microfiber and CNF are not homogenous and isotropic materials. Figure 1.10 shows cellulose has a chain structure consisting of numerous pyranose units (Dextro glucose) along the longitudinal direction. Two units of pyranose are sigma covalent bonded with oxygen (glycoside linkage). Though the structure of cellulose shows heterogeneity, most of the research found in the literature are investigating particularly axial elastic modulus [128].

2.3. Novelty of current study

To compensate for the information gap in the literature and eradicate the problems associated with the bundle fibers, measures have been taken in the current study. Single strands of kenaf microfibers and CNF were subjected to the experiments instead of fiber bundles to minimize the errors stem from the bundle basis consideration of fibers for testing. Besides, transverse modulus for kenaf and CNF have been considered for study which will contribute to the literature significantly as there is not enough study for transverse elastic modulus. Because of the structural heterogeneity of kenaf microfiber and CNF, it is necessary to know the elastic modulus in the transverse direction which should be different from the axial elastic modulus and can be a remarkable addition to the literature.

3. OBJECTIVES

The demand of bast fibers are increasing in our life for their renewability and biodegradability. Kenaf is one of the most popular bast fiber growing plants for its high yield, ease of growth in a wide range of weather conditions, and appreciable mechanical properties. Recently, kenaf is getting the attention of the composite industries alongside its conventional usages as textile raw material, rope, biomass, and animal feed. Hence, having an extensive idea of the fiber is important to utilize the fiber more appropriately in different applications. Besides, it helps us to identify the scopes to improve or modify the fiber for multipurpose applications. Therefore, the overarching goal of this research is to have a comprehensive idea about its mechanical properties to fill the research gap in the literature. On the other hand, cellulose nanofibril is one of the important building blocks of kenaf and the other bast fibers like this and can contribute potentially to their overall mechanical properties. This is why, it is also necessary to study cellulose nanofibril thoroughly to know its influence on the bast fibers, modify or treat the bast fibers for applications, and explore cellulose nanofibril's scopes to use it in the nanocomposites as reinforcement. Additionally, the research also focuses on the formulation of protocols that can be used to study elastic moduli of microfibers and nanofibrils.

An in-depth literature review shows that, most of the studies on the mechanical properties of kenaf fibers have focused on the axial elastic modulus though transverse elastic modulus is also an important parameter for an anisotropic material like kenaf fiber that also needs to be studied. Moreover, the method of testing a bundle of fiber has its own flaw. Similarly, studies have been performed mostly on the axial elastic modulus of the microfibril bundles of Cellulose. Hence, there are scopes to improve the test method and fix the issues of bundle-basis fiber

testing to determine accurate elastic moduli experimentally. Thus, the aspects we have focused on in this thesis cover:

- Determining the elastic moduli of kenaf microfiber in axial and transverse directions.
- Determining the elastic modulus of CNF in both axial and transverse directions.
- Scanning and generating surface morphology of CNF.
- Scanning and generating surface morphology of kenaf microfiber.

4. EXPERIMENT TECHNIQUE AND THEORIES

In this chapter, the experimental technique, theoretical models, and related assumptions will be discussed which were taken into the account for the experiment. There are three main sections of this chapter. The first section describes the AFM technique and some essential parts of the AFM setup to understand the basic functionality. The second section demonstrates data analysis models with what the AFM nanoindentation is analyzed where the last section refers to a micro tensile tester.

4.1. Atomic force microscopy (AFM)

4.1.1. Brief history

The era of the family of scanning probe microscopy (SPM) was initiated with the original invention of the scanning tunneling microscope (STM) in 1981 by Gerd Binnig and Heinrich Rohrer. This development in the field of microscopy brought them Nobel Prize in physics in 1986. AFM is a modified version of high-resolution STM that can facilitate the measurements on a nanometer scale and even smaller. AFM is primarily an invention of Binnig and the first experimental implementation was performed by the triad Binnig, Quate, and Gerber in 1986. AFM eliminated some serious shortcomings of the contemporary STM technique including being selective to apply for only conducting or semiconducting surfaces. On the other hand, AFM can image almost any type of surfaces which include but are not limited to polymers, ceramics, composites, glass, and biological samples. Their original AFM had a diamond shard which was attached at the end of a strip of gold foil. The diamond tip used to come into contact with the surface under experiment directly and sensed the interatomic van der Waals forces providing the interaction mechanism. The cantilever's vertical movement was sensed by a second tip – an STM situated above the cantilever.

4.1.2. Brief description of AFM parts

There are 8 major components of the AFM apparatus. A schematic of the AFM setup has been illustrated in Figure 4.1.

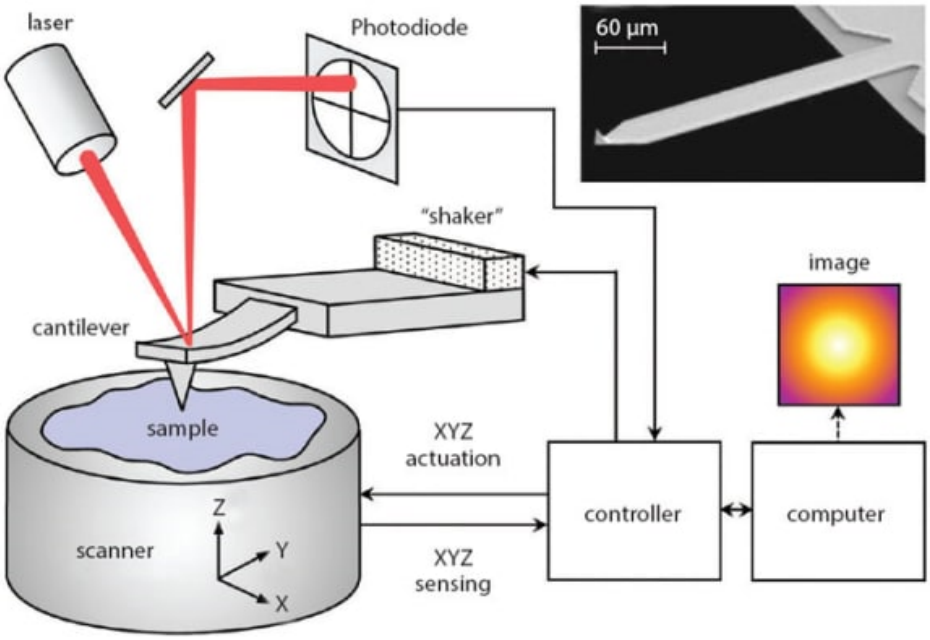

Figure 4.1. Schematic of AFM set up [129].

4.1.2.1. AFM cantilever

This is the central component of the AFM setup (Figure 4.2) which is a cantilever having several micrometers in length. The cantilever is generally made of flexible material with a sharp probe functionalized near the free end while the other end is attached to the piezoelectric tube. The cantilever used in this study had a dimension of 125 microns × 30 microns.

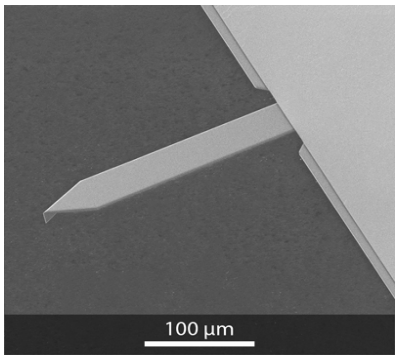

Figure 4.2. AFM cantilever [130].

4.1.2.2. AFM probe

AFM probe is also known as AFM tip which is the most important part of the AFM setup. The tip situated at the end of the cantilever is used to probe a sample by physically "feeling" the morphology of a surface while either being in contact or out of contact. AFM tips can have different shapes according to their applications. Figure 4.3 shows some popular types of tips. When the tip travels over the samples for imaging, it will move up and down which eventually deflects the incident laser to a different position of the photodiode. Thus, the height of different places on the sample can be sensed by the deflection of the cantilever. The measurements of surface height, composition, and local forces can be utilized in different types of studies including forming images, even with sub-nanometer resolution.

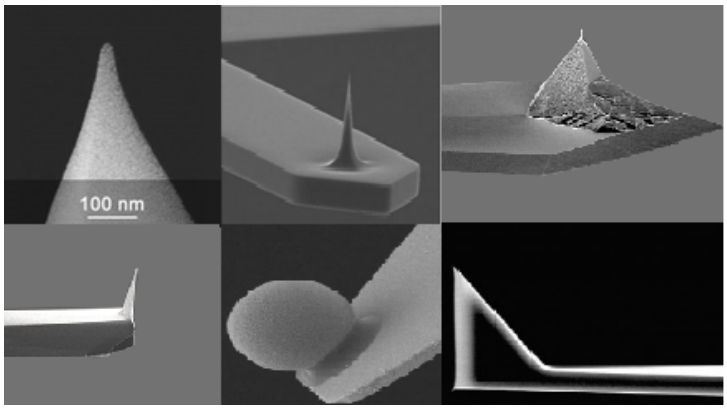

Figure 4.3. Different AFM probes [131-133].

4.1.2.3. Piezoelectric tube

The AFM cantilever is connected to the piezoelectric tube which is responsible for inducing the oscillation in it (Figure 4.4(a)). It also creates the raster motion to scan a sample in the X-Y plane. Figure 4.4 (b) shows the raster scanning profile of the AFM probe which has been initiated by a piezoelectric tube.

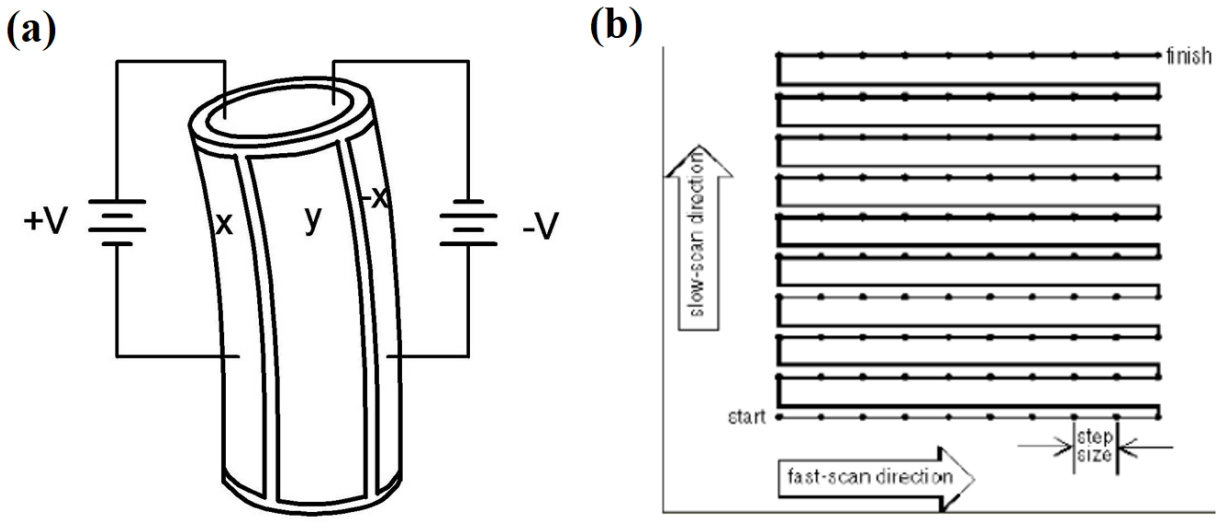

Figure 4.4. (a) An oscillating AFM piezoelectric tube. (b) Raster scanning by piezoelectric tube [134].

4.1.2.4. Laser

It is a laser beam that is shot from a laser gun placed over the cantilever and the target on the laser is the reflective top surface of the cantilever. The reflected laser beam is received by the mirror that is directed to a photodiode. The density of the laser is usually high and thus it can create an excellent spatial resolution.

4.1.2.5. Mirror

This is the reflective top surface of the cantilever. It reflects the incident laser to the photodiode.

4.1.2.6. Photodiode detector

Figure 4.5 depicts how the photodiode is arranged in the AFM head. There are four elements of the photodiode which are used to extract different information in different operating modes. The signals are combined, and this combined signal from all four elements is displayed on the elliptical SUM console. For the contact and tapping mode of AFM, the differential signal between the top two elements (A) and the two bottom elements (B) measures the vertical deflection of the cantilever. Similarly, while performing lateral force microscopy in contact mode, the differential signal between the sum of two left photodiodes (C) and the sum of the two right photodiodes (D) provides the measure of the torsional deflection of the cantilever.

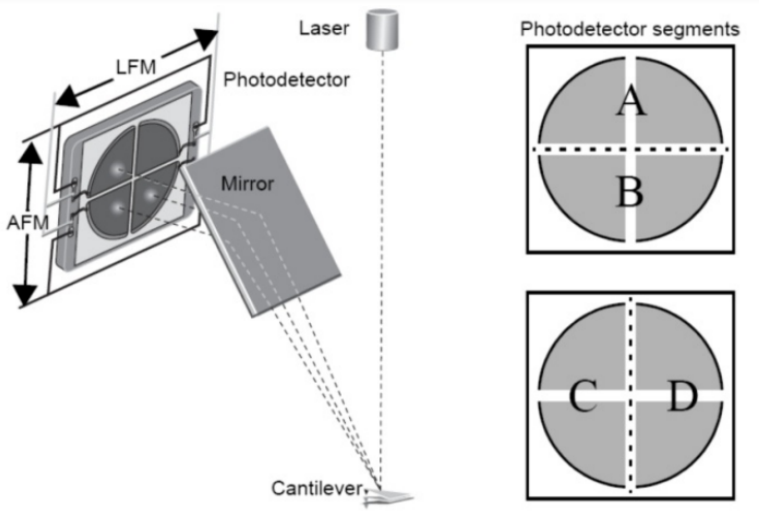

Figure 4.5. Schematic of AFM photodiode detector [135].

4.1.2.7. Amplifier

The amplifier received the data from the photodiode detector and amplifies the signal. Besides, the data are filtered and made ready for further processing before sending it to the register.

4.1.2.8. Register

The register is generally located in the computer where the data from the amplifier is received and analyzed to form a 3D image.

4.1.3. Surface morphology scanning by AFM

In the AFM procedure, the main theme is the scanning of a sample's surface by the travel of a cantilever with typically a very sharp tip to scan over a sample surface. Figure 4.6 shows a schematic of how AFM surface morphology scanning works. A laser beam is shot from the laser gun towards the reflective surface of the cantilever which is used to detect cantilever deflections towards or away from the surface. The laser is reflected by the photodiode and as the probe travels over the surface, due to the different heights on the surface, the reflected beam is deflected to different points on the photodiode detector. Being position-sensitive, the heights of different points on the sample can be logged from the positions of the reflected beam on the photodiode. Thus, all the heights on different points on the X-Y plane are combined to get an idea about the whole surface morphology. The quality of the scan can be adjusted by varying the frequencies and selecting how many sample point heights will be scanned per line of scanning.

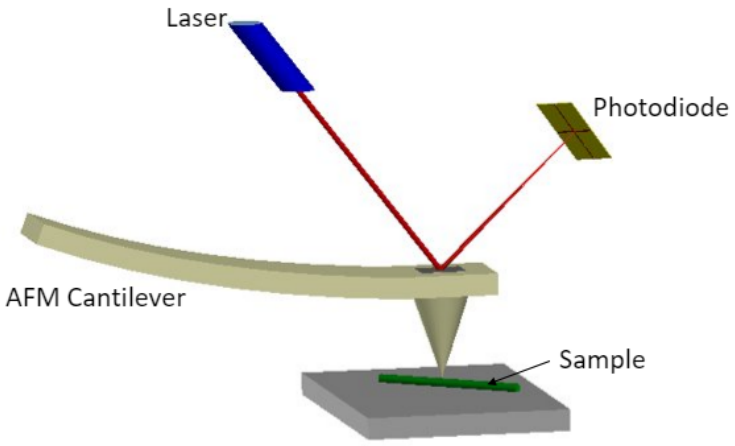

Figure 4.6. Schematic of AFM surface morphology scanning [64].

There are three different modes of scanning the sample points on a surface:

- **Contact mode**

In contact mode, the tip is dragged across the surface of the sample and the z-axis deflection of the cantilever is measured directly from the z-axis movement of the probe. Alternatively, the heights can be measured by considering the feedback signal needed to keep the cantilever at a certain position which is a more common approach. However, the challenge of this mode is the measurement and correction of the static signal coming from the probe which is prone to noise and drift. Strong attractive force can be very prevalent in the vicinity of the surface of the sample causing the tip to "snap-in" to the surface. Besides, this mode can damage the probe and the sample too. Hence, this mode of AFM is a nice fit at a depth where the overall surface force is repulsive.

- **Non-contact mode**

The Probe of the cantilever does not come into contact with the sample surface in the non-contact mode of AFM. The cantilever in non-contact mode is oscillated at its resonant frequency or just above where the amplitude of oscillation can be between a few picometers to a few nanometers (<10 nm). While oscillating near a surface, the probe faces the van der Waals forces which are generally strong enough from 1 nm to 10 nm above the surface to decrease the frequency of the oscillating cantilever. This decrease of the frequency is combined with a feedback loop system that tends to maintain a certain oscillation amplitude or frequency by adjusting the average tip-to-sample distance. The measurement of the tip-to-sample distance in the X-Y plane is used by the scanning software to form a topographic image of the sample surface. As the probe does not come into contact with the surface, there is no risk of the sample or the probe degradation in this mode which is a great advantage of non-contact mode over the

contact mode of AFM, particularly at the microscopy of the biological samples and organic thin film. However, it may not be a better option than contact mode when there are a few monolayers of adsorbed fluid or contamination on the surface of the sample.

- **Tapping mode**

The tapping mode is the most common dynamic mode of atomic force microscopy and can be used in versatile applications. In this mode, the cantilever is oscillated at or near its resonance frequency over the sample surface. The small piezo element at the cantilever holder induces the oscillating motion where the other oscillation sources are AC magnetic field, piezoelectric cantilevers, or periodic heating with a modulated laser beam. The amplitude of the oscillation can be up to 200 nm while keeping the frequency and amplitude of the driving signal constant. A constant amplitude oscillation of the cantilever is generated unless there is any drift or interaction with the surface, such as van der Waals forces, dipole-dipole interactions, electrostatic forces, etc. As the probe gets closer to the surface, the amplitude is influenced by the surface interaction forces. The influence on the amplitude is related to the height of a point being scanned. Using a feedback electronic system, the distance between the cantilever and sample is controlled by keeping either the amplitude or the phase of the oscillating cantilever constant with the help of the electronic servo.

4.1.4. AFM based nanoindentation

The main purpose of AFM-based nanoindentation is to determine the elastic modulus of a sample. It is a very effective technique to determine the elastic modulus of the nanoscale samples. In nanoindentation, the probe does not travel all over the surface but concentrates on a certain point of a sample to indent it. While indenting, along with the sample, the probe also faces surface forces from the sample surface. The indentation takes place up to a certain amount

of force sensed by the AFM probe. The force is a function of the voltage induced in the piezo. So, before the indentation, the voltage is set to limit the indentation process. Figure 4.47 shows a typical AFM nanoindentation curve.

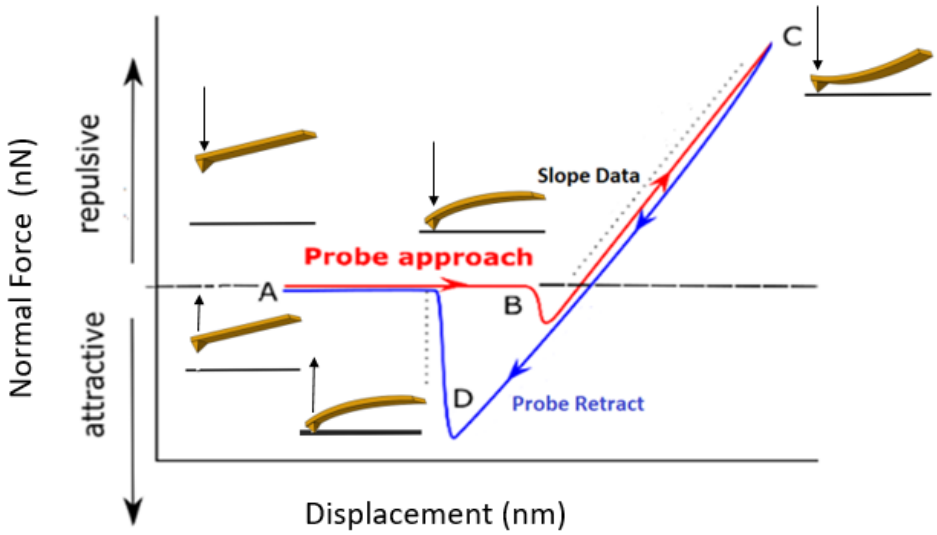

Figure 4.7. Typical nanoindentation curve (modified based on [136]).

There are two parts of the nanoindentation curve: probe approach (marked by red) and probe retract (Marked by blue). The indentation starts from point A when the probe starts to approach the sample surface. After point B when the probe is very close to the surface, it starts to feel the surface forces. It eventually becomes attracted to the surface starting to decrease the distance between the probe and the surface until it touches the sample surface while the cantilever is still far enough. Gradually the cantilever comes down and the probe starts to exert force on the sample pulling the curve up. The indentation takes place up to a preset point C and then the retraction starts. As the probe has indented the sample, the probe is now in contact with more molecules which apply more force on the probe when it tries to retract from the surface. Hence, point D shows the pull-off force at the retraction that is much bigger than the attraction force at the approach. After point D, the probe gets separated from the surface and finally, the

indentation ends at point A. This curve is used to analyze an appropriate model to extract more information, e.g., radial or transverse elastic modulus of the sample.

4.1.5. AFM based 3 points bending

AFM based 3-points bending is a feature of AFM which facilitates the determination of longitudinal or axial elastic modulus. The operation of the cantilever and the probe has similarities in their operation at the time of nano-indentation. However, the setup of the sample is a bit different in 3 points bending. Here, the sample is placed on a microfabricated plate with trenches. So, the two edges of the trench can work as a support for the sample where the probe comes down and applies force on a specified point of the sample.

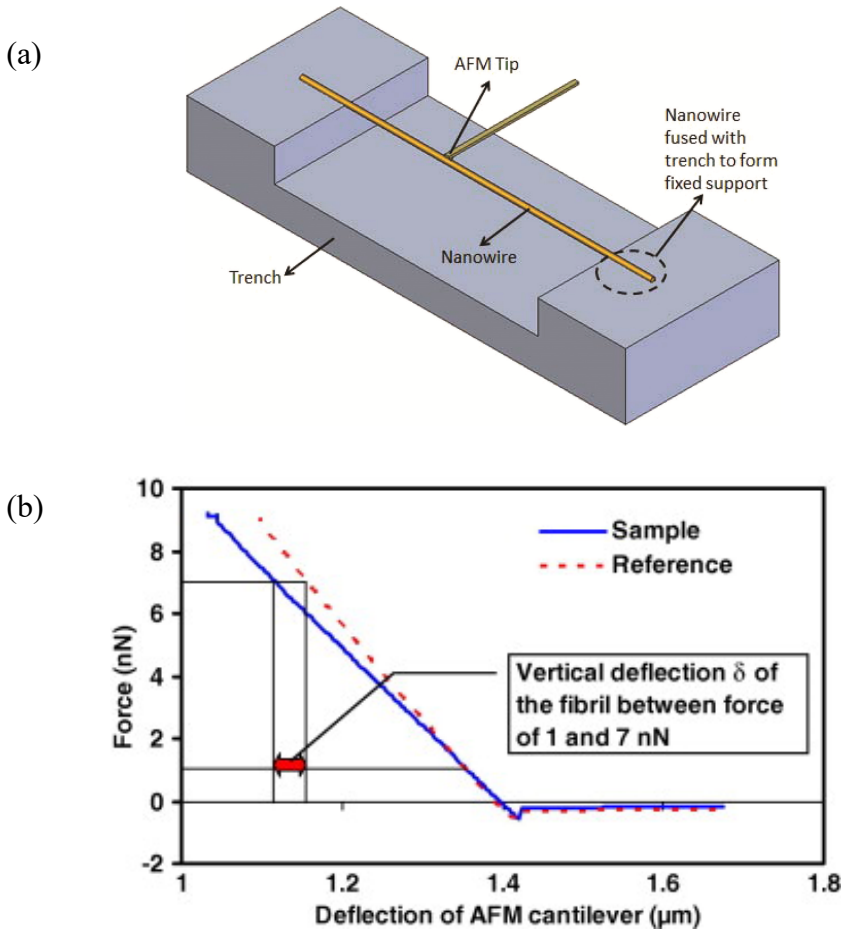

Figure 4.8. (a) Schematic of 3 points bending test [137]. (b) Typical AFM-based 3 point bending curve [113].

Figure 4.8(a) shows the sample setup on the trench for AFM-based 3 points bending where Figure 4.8(b) shows a typical curve found from the experiment. There are two parts to a curve. The red dotted line is the indentation curve found from the nano-indentation of the reference material, e.g., Silicon wafer whereas the blue curve is found from the 3 points bending by AFM. The horizontal distance between two points of this curve denoted the deflection under a certain force. This information is used in the beam formula to find the modulus.

4.1.6. Advantages

Arguably, atomic force microscopy is one of the most versatile and powerful microscopy technologies for studying samples at the nanoscale. There are several advantages for which AFM is very favorable in different types of applications including microscopy, elastic modulus determination, rough measurement, and viscoelasticity measurement. Some major advantages have been noted downwards.

4.1.6.1. 3D profile of surface

Unlike optical and electron microscopes, AFM can find the height profile of a sample to form a 3D image of a sample. As the z-axis deflection is measured in the AFM procedure, the 3D profile of a sample surface can be easily formed by AFM.

4.1.6.2. Inexpensive device

AFM is not a million-dollar set up like the electron microscopes. A good quality AFM can be obtained without spending no more than 100,000 dollars.

4.1.6.3. High resolution

A very high resolution can be achieved by using AFM to scan a sample. Typically, nanometer resolution can be easily achieved where even picometer resolution is also possible. Besides, it doesn't need any lens to zoom which depends on the scan size.

4.1.6.4. Safe to work with vulnerable samples

AFM does not create any electron beam or is not dependent on light. It eliminates the risk of possible damage to the sample due to the light, electron beam, or other rays that are detrimental to samples. Hence, it is also very safe to apply to the biological sample which keeps the sample alive after the scan.

4.1.6.5. No risk of radiation

As there is no electron beam associated with the AFM procedure, there is no risk of the creation of any radiation or harmful beam for human.

4.1.6.6. Easy sample preparation

There is no complicated and lengthy sample preparation like what we have to do for the sample preparation of TEM, SEM, EELS, etc. As the surface is only scanned, a sample of any thickness can be scanned through this procedure which cancels the necessity of making a sample with micro/nanoscale thickness.

4.1.6.7. Wide range of medium of application

AFM can scan samples in a wide range of mediums including vacuum, air, and liquids.

4.1.7. Limitations

4.1.7.1. Small single scan image size

The image size of the scanning is very small which is mostly on the order of 150 x 150 micrometers where the image size of SEM and TEM are in the millimeter range. As the scanned area is increased, the quality of the image is deteriorated in the AFM for the pendulum effect of the cantilever.

4.1.7.2. Slow process

As the AFM scans line by line, the process is very slow. If the scanning rate is increased, it affects the quality of the scan. The slow scan rate often causes thermal drift on some specific types of samples.

4.1.7.3. Replacement of probe

The probe used in the AFM is very fragile and it is very common to break the probe while focusing on the desired sample surface to scan. Besides, the probe can lose sharpness easily after scanning several and there is also a risk of probe contamination while scanning on different surfaces.

4.1.7.4. Calibration

AFM needs calibration on a timely basis. As the setup is dependent on the piezo which prone to issues like hysteresis, it is always important to calibrate the AFM setup regularly for an accurate result.

4.1.7.5. Unable to identify material compositions

AFM can only scan the surface and the major scope of AFM is limited to the surface phenomenon. Hence, it is not easy to identify different atoms and bonds in a compound similar to TEM, SEM, EELS, ERD, etc. Besides, the subsurface data is not possible to be extracted in AFM.

4.2. Theoretical models of elastic contact mechanics

4.2.1. Hertz model

Hertz model is a very popular model in contact mechanics which was proposed by Hertz in 1882 in his legendary research article named ‘On the contact of elastic solids’ [138] which can be applied for the non-adhesive elastic contact between two spheres. This model addresses

the localized contact stress developed [139] between two curved surfaces in contact and are subjected to deformation due to the applied load. For the simplicity of the mathematical derivation, the equation of the spherical profile was supplanted by the equation of the parabolic profile in this model [140]. Hence, the Hertz model assumes the contacts as small contact cases where the contact radius is small enough compared to the radii of the two interacting elastic spheres (Figure 4.9). The theory suggests two-equation for the two spheres contact. The Hertz theory for two spheres contact can be represented by the following equations [139, 141].

$$a^3 = \frac{3\pi}{4}(k_1 + k_2)\frac{R_1 R_2}{R_1 + R_2}\, P \tag{4.1}$$

$$\delta^3 = \frac{9\pi^2}{16}(k_1 + k_2)^2 \frac{R_1 + R_2}{R_1 R_2} P^2 \tag{4.2}$$

Here, a is the contact radius, R_1 and R_2 are the radii of the two contacting surfaces, ν_1 and ν_2 are the Poisson's ratio of the two spheres, and $E_1$and E_2 are the elastic modulus of the two intersecting spheres. The contact force and the indentation depth are denoted by P and δ respectively where the elastic constants, k_1 and k_2 are measured using equation (4.3) and (4.4).

$$k_1 = \frac{1-\nu_1^2}{\pi E_1} \tag{4.3}$$

$$k_2 = \frac{1-\nu_2^2}{\pi E_2} \tag{4.4}$$

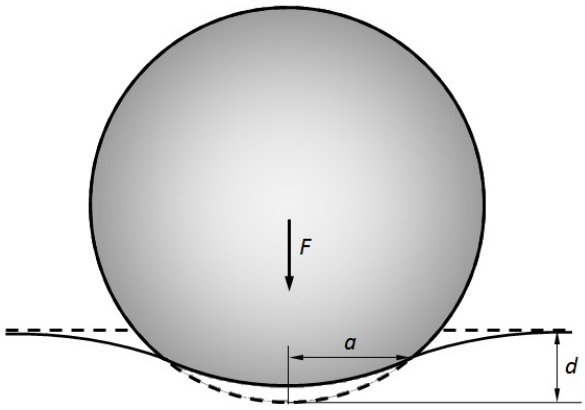

Figure 4.9. Interaction between an elastic sphere and an elastic half-space [142].

Hertz model has been popularly used in literature. Babahosseini et al. has used this model in the determination of the mechanical properties of ovarian cancer stem-like/tumor-initiating cells [143]. In another research, the Hertz model has been applied in the determination of the dynamic response of a human knee joint model by Machado et al. However, a negative force is observed in the indentation force-displacement curve at a certain portion of the indenter/probe before the tip is detached from the sample surface. This phenomenon stems from the surface forces including van der Waals between the molecules and this is an obvious incident in the cases of nano-level contacts. Hence, this model falls short in the nano-indentation where such strong surface forces are extant.

4.2.2. Johnson-Kendall-Roberts (JKR) model

To compensate for the gap in the existing contact mechanics model in the literature, the Johnson-Kendall-Roberts (JKR) model was introduced in 1971 where the surface force was considered [141]. They have started from the mathematical formulation of the Hertz model and incorporated the effect of the surface energy. The developed model was verified through a contact experiment on rubber and gelatin surfaces which were found to satisfy their theory. The model presents the contact circle radius, *a,* as a function of the applied load where

$$a^3 = \frac{R}{K}(P + 3G\pi R + \sqrt{6G\pi RP + (3G\pi R)^2}) \tag{4.5}$$

The external force is represented by P and the nominal elastic constant, K is calculated from equation (4.6).

$$K = \frac{4}{3\pi(k_1+k_2)} \tag{4.6}$$

Here, elastic constants, k_1 and k_2 are measured using equation (4.7) and (4.8).

$$k_1 = \frac{1-\nu_1^2}{\pi E_1} \tag{4.7}$$

$$k_2 = \frac{1-\nu_2^2}{\pi E_2} \tag{4.8}$$

R is determined using the radius of the indenter tip (R_i) and the radius of the sample (R_s) in equation (4.9).

$$R = \left(\frac{1}{R_i} + \frac{1}{R_s}\right)^{-1} \tag{4.9}$$

R and the pull-off force, P_o are used to find the adhesion release rate G at the contact surface through equation (4.10) which can be equal to the adhesion energy of the contact area γ in the equilibrium systems.

$$G = -\frac{6P_o}{5\pi R} \tag{4.10}$$

The combination of equations (4.5) and (4.10) forms the following equation (4.11).

$$a^3 = \frac{R}{K}(P - 2P_o + \sqrt{-4P_oP + 4P_o^2}) \tag{4.11}$$

According to this model, the deformation can be defined by equation (4.12).

$$\delta = \frac{a^2}{R} - \sqrt{\frac{8G\pi a}{3K}} \tag{4.12}$$

4.2.3. Derjaguin-Muller-Toporov (DMT) model

DMT model is the next stage development JKR model which not only considers the contact surface forces but also it takes the surface force out of the contact region [144]. In this model, the contact radius and the deformation can be expressed by equation (4.13).

$$a = \sqrt[3]{\frac{R}{K}(P + 2\pi GR)} \tag{4.13}$$

Here R is the nominal radius, K is the nominal elastic constant, P is the external force, and G is the adhesion release rate at the contact surface which is yielded by equation (4.14).

$$G = -\frac{P_o}{2\pi R} \tag{4.14}$$

According to this model, the surface deformation is calculated by equation (4.15).

$$\delta = \frac{a^2}{R} \tag{4.15}$$

4.2.4. Bradley model

This model is based on the Lennard –Jones potential which suggests the surface force between atomic planes at a distance z can be expressed by equation (4.16).

$$P(z) = \frac{16\gamma}{3z_o}\left[\left(\frac{z}{z_o}\right)^{-9} - \left(\frac{z}{z_o}\right)^{-3}\right] \tag{4.16}$$

Here P is the applied force, 2γ is the total surface energy of both surface per unit area, and z_o is equilibrium distance between two atomic planes.

The Bradley model is applicable to find the surface force between two spheres using the Lennard –Jones potential. The total surface force between two spheres of radius, R_1 and R_2 according to this model can be estimated through equation (4.17) [145].

$$P = \frac{16\gamma\pi R}{3}\left[\frac{1}{4}\left(\frac{z}{z_o}\right)^{-8} - \left(\frac{z}{z_o}\right)^{-2}\right] \tag{4.17}$$

4.2.5. Maugis-Dugdale (MD) model

MD model was initiated in 1991 to resolve the contradiction between JKR and DMT models. This model is a derivative of a self-consistent numerical calculation where the Dugdale model has been used instead of Lennard –Jones potential. As per this model, the force, P and the surface deformation can be determined by equations (4.18) and (4.19) respectively [146].

$$P = \pi w R[\bar{a}^3 - -\lambda\bar{a}^2(\sqrt{m^2-1} + m^2\tan^{-1}\sqrt{m^2-1}] \tag{4.18}$$

$$\delta = \left(\frac{\mathrm{K}^2}{\pi^2\mathrm{w}^2\mathrm{R}}\right)^{-\frac{1}{3}}(\bar{a}^2 - \frac{4}{3}\bar{a}\lambda\sqrt{m^2-1}) \tag{4.19}$$

Here, m is the ratio of contact radius, a, and the radius of the adhesive region, c. λ is defined by equation (4.20).

$$\lambda = 2\sigma_o\left(\frac{R}{\pi\omega K^2}\right)^{\frac{1}{3}} \tag{4.20}$$

Equation (4.21) is used to determine $\bar{a}$.

$$\bar{a} = a\left(\frac{K}{\pi\omega R^2}\right)^{\frac{1}{3}} \tag{4.21}$$

4.2.6. Applicability of contact mechanics model

The contact mechanics models demonstrated in the above paragraphs are applicable in different situations according to the interacting materials. So, this is important to know the applicability of different contact mechanics models. For a better understanding of the scenarios, Marshall et al. have sketched an adhesion map (Figure 4.10) based on 2 parameters that are defined to be λ and $\bar{P}$ where λ is the ratio between the elastic deformations on the surface and the range of surface forces [147]. On the other hand, $\bar{P}$ measures the ratio of the load to the adhesive force. λ and $\bar{P}$ can be calculated by equations (4.22) and (4.23) respectively.

$$\lambda = \sigma_o\left(\frac{8R}{\pi w K^2}\right)^{\frac{1}{3}} \tag{4.22}$$

$$\bar{P} = \frac{P}{\pi w R} \tag{4.23}$$

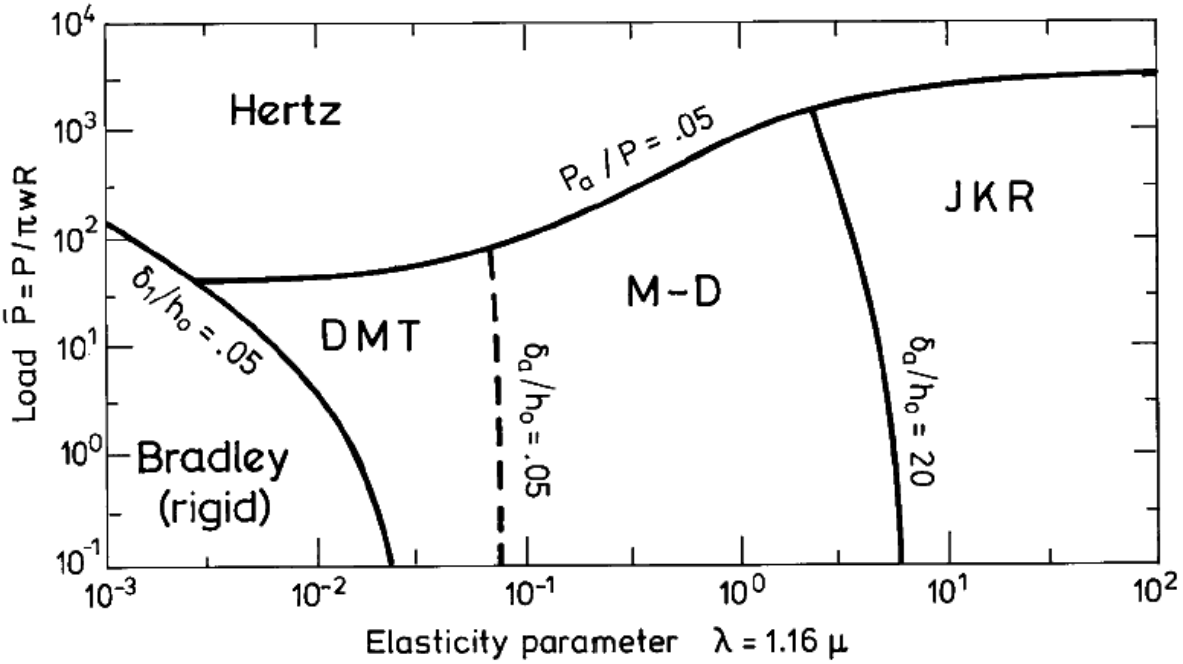

Figure 4.10. Adhesion map for contact mechanics models [147].

Hertz contact model is more applicable in the cases where the surface force can be overlooked compared to the applied load. The condition for the applicability of the Hertz model can be expressed by equation (4.24) where P is the load and P_a is the adhesive force proposed in the MD model.

$$\left|\frac{P_a}{P}\right| < \xi \tag{4.24}$$

Equation (4.25) can be used to determine the adhesive force.

$$P_a = -2\sigma_o c^2[\cos^{-1}\left(\frac{a}{c}\right) + a\sqrt{c^2 - a^2}] \tag{4.25}$$

Here a is the radius of the region under compression, c is the radius of the region under tension which has been induced by the adhesion, and σ_o is the uniform adhesive stress between the regions of radius a to that of radius c. There is no technically determined value of the parameter ξ. Hence, it can be chosen arbitrarily which will be less than 1. In Fig. 4.9, the parameter has been chosen as 0.05.

JKR and DMT model consider the effect of surface adhesion force where Tabor specified the cases of applicability of these two models. Tabor initiated a dimensionless parameter known as the Tabor parameter, μ, i.e., the ratio between the gap outside the contact zone and the equilibrium distance between atoms [148, 149]. DMT is applicable where $\mu < 0.1$; for the cases where $\mu > 10$, JKR is appropriate. As per the assumption, the Bradley model is limited to the contact between two surfaces with high elastic modulus which makes it applicable to the rigid contact.

4.3. Fiber tensile tester

Instron TARDIS set-up was used for fiber testing that has the capability to handle micro-level fibers to measure the fiber diameter and perform the tensile test of a fiber. The tester has four major parts: Sample Holder, Pneumatic Arm, Loading Assembly, Fiber Micrometer, Controller Unit, and Pneumatics Unit. The image of a full setup with an exploded view has been shown below in Figure 4.11.

4.3.1. Sample holder

The sample holder is also known as a cassette which is a metal slab with the slots to accommodate the tabs in a row. Each sample is glued by UV curable Epoxy on the two sides with tabs. The flat middle region of the tab is the place where the pneumatic arm can suck air and grab it to move the sample to places. Figure 4.11 (c) shows the cassette and the arrangement of the samples on it.

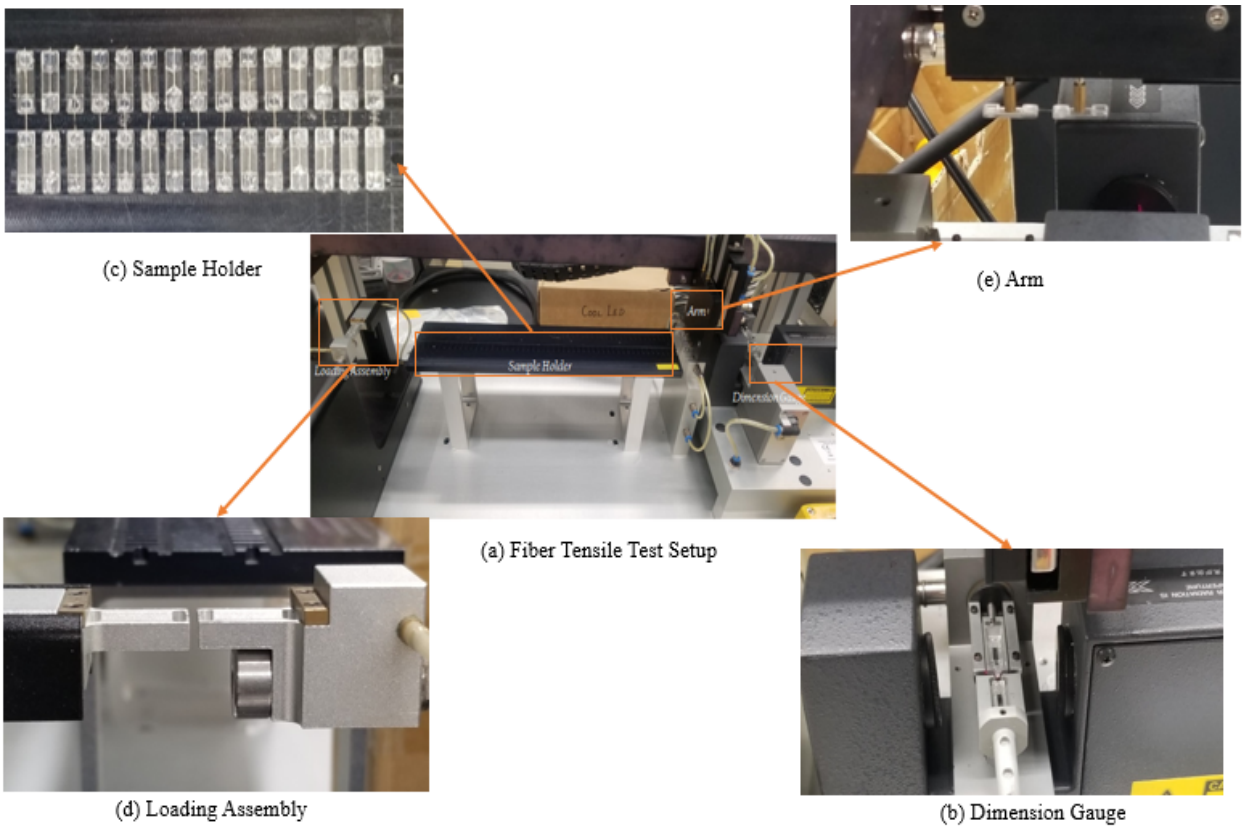

Figure 4.11. (a) Fiber tensile tester set up; (b) Fiber micrometer; (c) Sample holder; (d) Loading assembly; (e) Pneumatic arm.

4.3.2. Pneumatic arm

The pneumatic arm is responsible for grabbing the tab with the sample from the cassette and moving it to the dimension gauge, loading assembly, and finally bringing back to the cassette. It has two nozzles which are used to grab the tabs. The arm can move along a linear path on a rod assembly. The pneumatic arm has been shown in Figure 4.11 (e).

4.3.3. Loading assembly

Loading assembly shown in Figure 4.11 (d) is the main component of the tensile tester where the tensile test is performed. It is a miniature version of the common tensile testers where a very small strain rate is possible to achieve. The pneumatic arm brings the tab with the sample to the loading assembly. There are two small jaws on what the tabs are attached by decreasing

the air pressure. The failure criterion is set from the computer software and the tensile test is done until meeting that certain condition.

4.3.4. Fiber micrometer

A fiber micrometer is a specialized device that is used to measure the diameter of the fiber. There are slots where the pneumatic arm places the tab with the sample. It keeps the sample attached by its pneumatic set-up which decreases the air pressure. A laser is used to measure the diameter. The dimensions at different places of the sample are measured to yield the mean diameter of the sample.

4.3.5. Controller unit

The controller unit is used to regulate the overall process. It receives the input from the computer software about the test parameters and regulates the air pressure through the pneumatic unit to grab and move the tab with the sample, measure the sample diameter, and test the sample.

4.3.6. Pneumatics unit

The pneumatic unit controls the air pressure in different parts of the tensile tester according to the necessity. The unit receives compressed air for its operation to move different parts of the tensile tester and grab samples.

5. DETERMINATION OF ELASTIC MODULUS OF KENAF MICROFIBER[1]

In this chapter, the measurement of the axial and transverse elastic modulus of kenaf microfiber has been discussed with associated protocols. The results have been analyzed with different models and statistics.

5.1. Transverse elastic modulus of kenaf microfiber

The measurement of the elastic modulus of kenaf microfiber has been demonstrated to fill up the gap in the literature. To find the transverse elastic modulus in the transverse direction, individual kenaf microfiber was subjected to the experiment. The transverse elastic modulus of the fiber was characterized by atomic force microscopy-based nanoindentation. To determine the transverse elastic modulus from the force vs sample deformation data, the extended Johnson-Kendall-Roberts model was used which considered adhesion forces from the fiber surface. A shooting method was used to find the correct modulus to find the modulus with which a numerically expensive regression method was avoided.

5.1.1. Material and experimental procedures

The kenaf microfiber was supplied from Sunstand LLC. The room temperature and humidity of the lab were maintained as 70°F and 30%, respectively. Figure 5.1 shows a schematic of the sample surface scanning by AFM, and AFM based *in situ* nanoindentation to determine the elastic modulus of the sample in the transverse direction. AFM was performed using the tapping mode of the probe (Bruker: SNL 10). Slipping of the AFM probe on a tapered

[1] The material in this chapter was co-authored by M Subbir Parvej, Dr. Xinnan Wang, Joseph Fehrenbach, and Dr. Chad Ulven. M Subbir Parvej had primary responsibility for sample preparation and experimental data collection from testing and imaging. M Subbir Parvej was the primary developer of the conclusions that are advanced here. M Subbir Parvej also drafted and revised all versions of this chapter. Dr. Xinnan Wang provided guidance and support during experimentation, proofread and checked the math and logic of conclusions. Joseph Fehrenbach and Dr. Chad Ulven supported sample preparation, Instron TARDIS fiber tester, and proofreading. The majority of the section, by the listed authors, was originally published by SAGE in the Journal of Composite Materials [64]. Parvej, M.S., et al., *Atomic force microscopy-based nanomechanical characterization of kenaf fiber.* Journal of Composite Materials. and is reused here with permission.

or irregular surface was avoided by gradually reducing the scan size down to 1 nm ×1 nm right on the top of the fiber and keeping the scanning rate as low as 0.5 Hz. On the other hand, for the indentation, the sample was fixed firmly with a surface. To fix the kenaf microfiber with a clean flat glass slide surface, epoxy was used as a binding agent. The fibers with a length of 5-6 mm were spread on the surface covered by partially cured epoxy to prevent the epoxy from reinforcing the fiber, and another glass slide was pressed on it to fix the fibers strongly with the surface. After ensuring the fixation of the fibers to the surface, nanoindentations were performed on the same kenaf microfiber. The indentation voltage for the piezo sensor was set as 0.2 V and the indentation was continued up to that voltage. As the 3-sided pyramidal tip of the AFM probe pressed onto the fiber surface, the induced voltage changed with the value of the z-axis. The change in voltage was recorded during the experiment. Nanoindentations were performed at 4 different locations in total along the center of the fiber in a similar way with the AFM tip as shown in Figure 5.1 (b). To minimize the deformation effect of adjacent indentations, the distance between two indentations was maintained at least 300 nm. Next, the obtained voltage data were then converted into the indentation force by multiplying it by sensitivity and the spring constant, k_c. Among several methods to find k_c, the Sader method was followed. This method is regarded as a reliable and easy method to use. According to this method, k_c is given by equation (5.1).

$$k_c = M_e \rho b h l w_{vac}^2 \tag{5.1}$$

Here, M_e is the normalized effective mass, k_c is the density of the Si cantilever, *b, h, l,* are the width, thickness, and length of the cantilever, respectively, and the unloaded resonance frequency of the cantilever is expressed as w_{vac}.

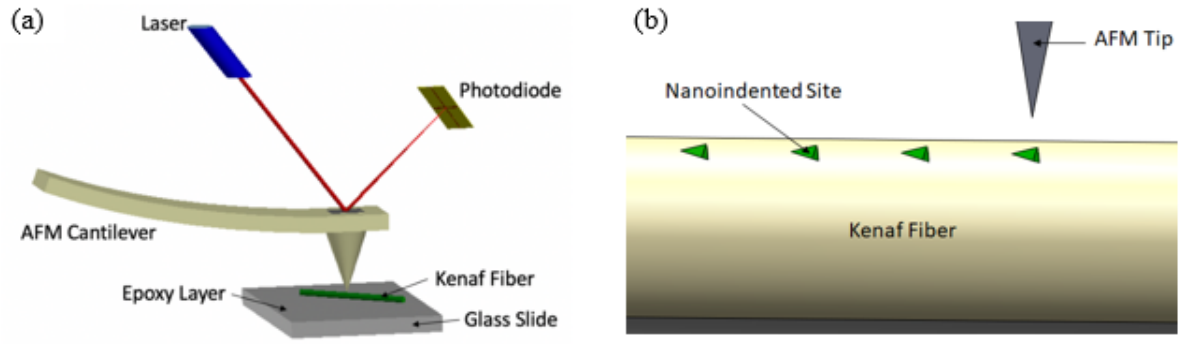

Figure 5.1. Schematic of (a) AFM scanning and (b) nanoindentation on kenaf microfiber [64].

5.1.2. Result and discussion

19 Kenaf microfibers were imaged by optical microscope and the average diameter of the imaged kenaf microfiber was found as 62.1±11.4 µm. Figure 5.2 (a) shows the optical imaging of the fiber. The fiber was later subjected to AFM imaging, presented in Figure 5.2 (b). As the diameter of kenaf microfiber is very large compared to that of the AFM probes, the surface was found almost flat. Also, the imperfections of the fiber surface and traces of different microfibers in the entangled form are visible from the surface morphology.

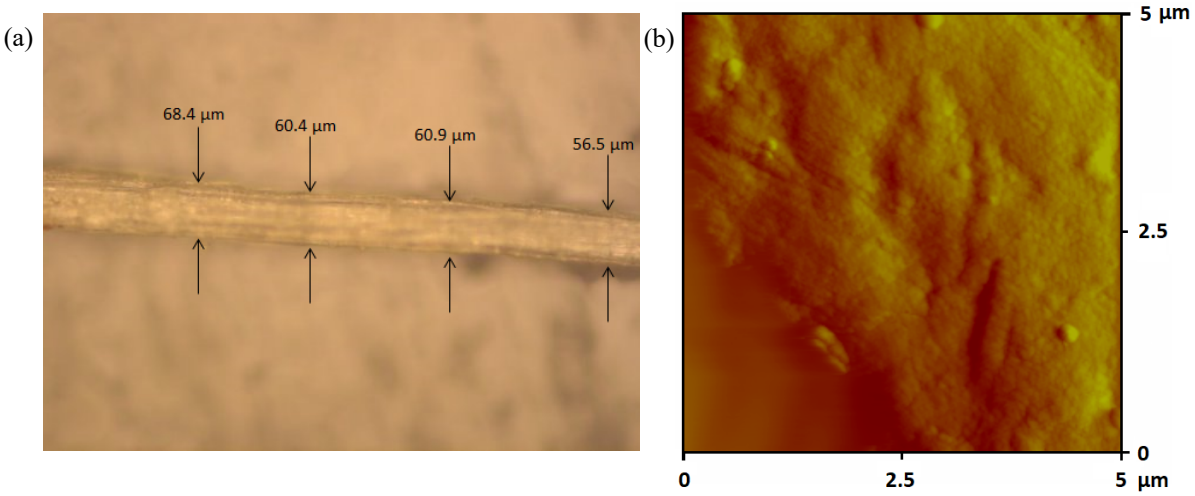

Figure 5.2. (a) Optical microscope image of a kenaf microfiber, (b) AFM surface image of kenaf microfiber [64].

When nanoindentation was performed on the sample, the deflection (z-axis displacement of the cantilever) curve was influenced by the adhesive forces coming both from the sample and the glass slide. To extract the deformation of the sample from this combination deducting the effect of glass, we need to perform nanoindentation on glass separately. Herein, nanoindentation force vs Z-piezo displacement (F-z) curves for kenaf microfiber and glass slide are shown in Figure 5.3. It is observed that, as the AFM probe approached the sample surface, i.e., extension, the reaction force decreased suddenly. The cause of this phenomenon is due to the van der Waals force that is adhesive between the probe and the sample, thereby bending the AFM cantilever towards the sample. The AFM cantilever continued to come down after this 'jump to contact' point and started to apply force on the sample up to the specified limit. After that, the AFM cantilever starts to move up, i.e., retraction, and as the probe is in contact with more surface of the sample, it experienced more van der Waals force making the adhesive force of retraction larger over the adhesion force of extension. Besides, the moisture of the fiber has a certain effect on the van der Waals force. For this study, the fibers were dried in an oven before the AFM procedure and the moisture content was determined by a Computrac Moisture Analyzer which was very low, i.e. 10%, for which the effect of moisture content can be overlooked. Additionally, it has also been observed in Figure 5.3 (b) that the glass has a significant amount of adhesion with the AFM probe. It implies that the effect of adhesive force from the glass is extant in the extension and retraction curve of the sample depicted in Figure 5.3 (a). So, the difference of deformation between Figure 5.3(a) and 5.3 (b) for a particular force can be regarded as the deformation for the kenaf sample [150].

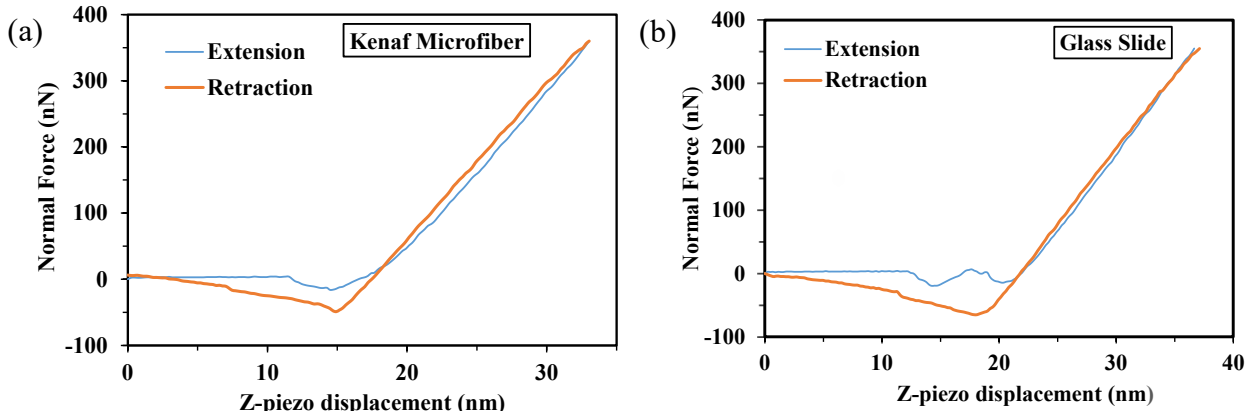

Figure 5.3. AFM nanoindentation curve for (a) Kenaf microfiber, and (b) Glass slide [64].

5.1.3. Theoretical analysis

The contact mechanics theory of Hertz has been widely used, especially for the non-adhesive elastic contact [151, 152]. When surface adhesion force is present, particularly at the nanoscale contact, an inaccurate elastic modulus can stem from the error in the normal force vs. sample deformation (F-Δz) curve, if the conventional Hertz model is applied, which makes this theory insufficient. Later in the 1970s, the Johnson-Kendall-Roberts (JKR) and Derjaguin-Muller-Toporov (DMT) models were developed to account for the adhesive effect [144, 149]. Tabor was the first to investigate the applicability of these two models that are based on the opposite extremities of sample compliance and the adhesive force range. The Tabor parameter, μ, is used to choose a correct model for a system between DMT and JKR [148, 149]. When $\mu \ll 1$, i.e., stiff solids, small radius of curvature, and weak energy of adhesion, DMT is appropriate [144]. On the other hand, for compliant solids with a large radius of curvature and large adhesion energy where $\mu \gg 1$, JKR is applicable [148, 149]. A limitation of these three models is their estimation of the sphere as a parabola, which can only be overlooked for a small contact radius. To curtail the extent of error, Maugis extended the JKR model by supplanting the parabola with

a spherical profile [140]. In this research, the extended JKR model was used to analyze nanoindentation.

According to the extended JKR, the indentation depth onto the sample Δz, and load, P can be expressed as the by equations (5.2) and (5.3).

$$\Delta z = \frac{a}{2}\ln\frac{R+a}{R-a} - \left(\frac{8\pi a\gamma}{3K}\right)^{\frac{1}{2}} \tag{5.2}$$

$$P = \frac{3aK}{2}\left[\frac{R^2+a^2}{4a} ln\frac{R+a}{R-a} - \frac{R}{2} - \left(\frac{8\pi a\gamma}{3K}\right)^{\frac{1}{2}}\right] \tag{5.3}$$

Here, a is contact radius and γ is adhesion release rate at the contact surface which is determined by equation (5.4).

$$\gamma = -\frac{3P_o}{2\pi R} \tag{5.4}$$

Here, P_o is the pull-off force and using equation (5.5) the nominal radius, R, is calculated.

$$R = \left(\frac{1}{R_i} + \frac{1}{R_s}\right)^{-1} \tag{5.5}$$

The radius of the indenter and the radius of the sample is denoted by R_i and R_s, respectively. K is called the nominal elastic constant that is computed from equation (5.6).

$$K = \frac{4}{3\pi(k_1+k_2)} \tag{5.6}$$

k_1 and k_2 are measured as $k_1 = \frac{1-\nu_1^2}{\pi E_1}$ and $k_2 = \frac{1-\nu_2^2}{\pi E_2}$, where $\nu_1$and ν_2 are the Poisson's ratio and $E_1$and E_2 are elastic moduli of the interacting spheres.

As the radius of the fiber is very large compared to the radius of the AFM probe tip, it can be considered a flat surface, taking the radius of the sample as $R_s = \infty$. The radius, elastic moduli, and Poisson's ratio of the indenter were extracted from the indenter manufacturer's data,

which are $R_i = 15\ nm$, $\nu_1 = 0.27$, and $E_1 = 150\ GPa$. Poisson's ratio of kenaf microfiber was assumed as $\nu_2 = 0.3$ [153].

The elastic modulus of the kenaf microfiber was estimated by finding the $F - \Delta z$ curve, generated from equation (5.2) and (5.3) that fits best with the experimental data.,

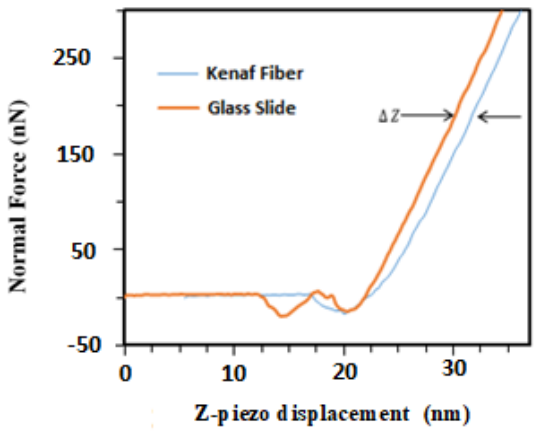

Figure 5.4. Combined $F - \Delta z$ curve of kenaf microfiber and glass slide indentation [64].

To find Δz the retraction $F - z$ curves found from the indentation of the glass slide and kenaf microfiber sample depicted in Figure 5.4. For a certain value of force, Δz is counted as the horizontal difference between the z-piezo displacements of kenaf microfiber and glass slide. Thus, for different forces, corresponding Δz values were extracted, therefore, the $F - \Delta z$ curve for the kenaf microfiber was obtained. A shooting method, i.e., using different assumed elastic moduli of the kenaf sample back and forth to find the expected value, was used to quantify the transverse elastic modulus of the fiber. The quality of the fit was assessed by determining the coefficient of determination (R^2). Figure 5.5 shows the best fit curve having the highest R^2 value as 0.97 (inset) for the elastic moduli 2.3 GPa where, from the study of 3 samples in total, the average transverse elastic modulus of kenaf microfiber was calculated as 2.33$\pm$0.05 GPa. The elastic modulus is much lower than the value for longitudinal elastic modulus found in the literature[154]. Nevertheless, this ambiguity can be elucidated if the fashion of loading is

observed. AFM-based nanoindentation determines elastic modulus in the transverse direction of the fiber whereas the higher elastic modulus of kenaf presented in the literature is for the longitudinal direction. A similar scenario has been observed for the bamboo fiber where the transverse elastic modulus was 55% of the longitudinal elastic modulus [155].

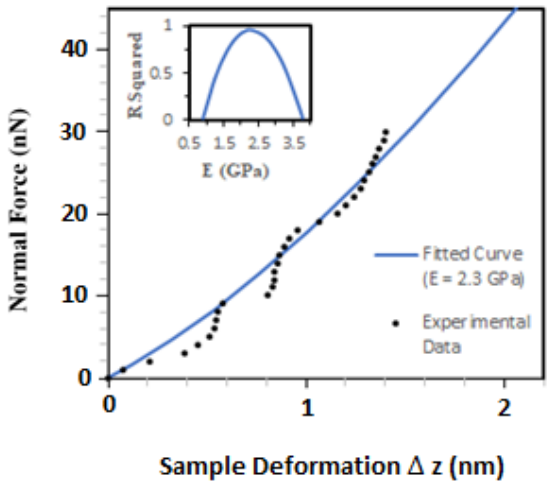

Figure 5.5. Nanoindentation forces vs sample deflection graph; Inset: Co-efficient of determination [64].

As the fibrils of fiber are oriented towards the longitudinal direction, this is expected to have a greater modulus in that direction. Besides, being an anisotropic material, it is essential to know the mechanical properties of kenaf microfiber in every possible direction. Here, the transverse elastic modulus is particularly important to determine the shear modulus and Poisson's ratio of the fiber properly [126]. In addition to that, transverse elastic modulus strongly influences torsional strength [127]. Thus, the transverse elastic modulus can contribute to understanding the mechanical properties of kenaf microfiber completely.

5.2. Axial elastic modulus of kenaf microfiber

In this section, the measurement of the axial elastic modulus of kenaf microfiber will be discussed. To find the axial elastic modulus of kenaf microfiber, individual kenaf microfiber was subjected to the experiment. A TARDIS fiber testing machine from Instron has been used to

measure the diameter and the tensile strength of the fiber. A stress-strain curve was extracted from the experiment for the kenaf microfiber. The elastic modulus was calculated from the curve as 15.54±1.95 GPa. Besides, tensile modulus and failure strain were also quantified from the curves and have been presented in the result section with Weibull distribution.

5.2.1. Material and experimental procedures

The kenaf microfiber was collected from Sunstand LLC. where the room temperature and humidity of the lab were maintained as 70° F and 30%, respectively. To prepare the fibers for the tensile test, they were kept in a heated chamber maintained at 120° F for 24 hours. The humidity was measured by Computrac moisture analyzer which was found as low as 3%. In the next step of sample preparation, the finest microfibers of kenaf were extracted carefully with a tweezer and stored on a tray.

The tensile test was performed on an Instron TARDIS set up that is capable of testing micro-level fibers under a very small strain rate. According to the ASTM C1557 standard, the test parameters were selected [156]. A cassette with 10 mm gauge length was selected for the experiment and the fibers were placed tout between the two ends of the ultra-violet (UV) curable Epoxy. During the curing, it was ensured that the fiber was dipped into the hole of the tab filled with uncured liquid Epoxy and the Epoxy did not overflow to come out of the tab to touch the portion of the kenaf microfiber that is subjected to the tensile test. A B.M.C UV generator was used to cure the Epoxy resin for 30 seconds. Figure 5.6 shows the UV generator used to cure the Epoxy on the two sides of the kenaf microfiber.

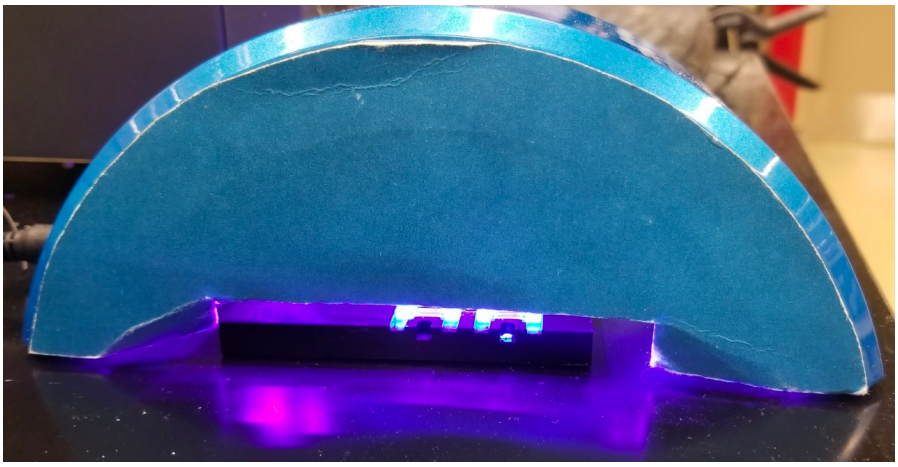

Figure 5.6. UV curing of epoxy resin.

As the TARDIS setup is a pneumatic device, constant air pressure is necessary to run it. Hence, air pressure was maintained 50 MPa in the setup. Besides, the setup was calibrated to increase the accuracy of the result. The whole testing method is regulated by a computer-operated software where the test parameters are set. The test parameters used for this experiment have been given below in Table 5.1.

Table 5.1. Test parameters.

Test Parameters	Set Value
The extension (%)	10
Rate (mm/sec)	0.01
Gauge Force (gmf)	1
Maximum force (gmf)	2000
Break threshold (gmf)	10

The samples to be tested were kept serially on the cassette and they were brought to a tensile tester one after one. Besides, before the tensile test, the diameter of fiber was also measured in a laser-based set up to determine the stress. Figure 5.7 shows a fiber that is subjected to the tensile test.

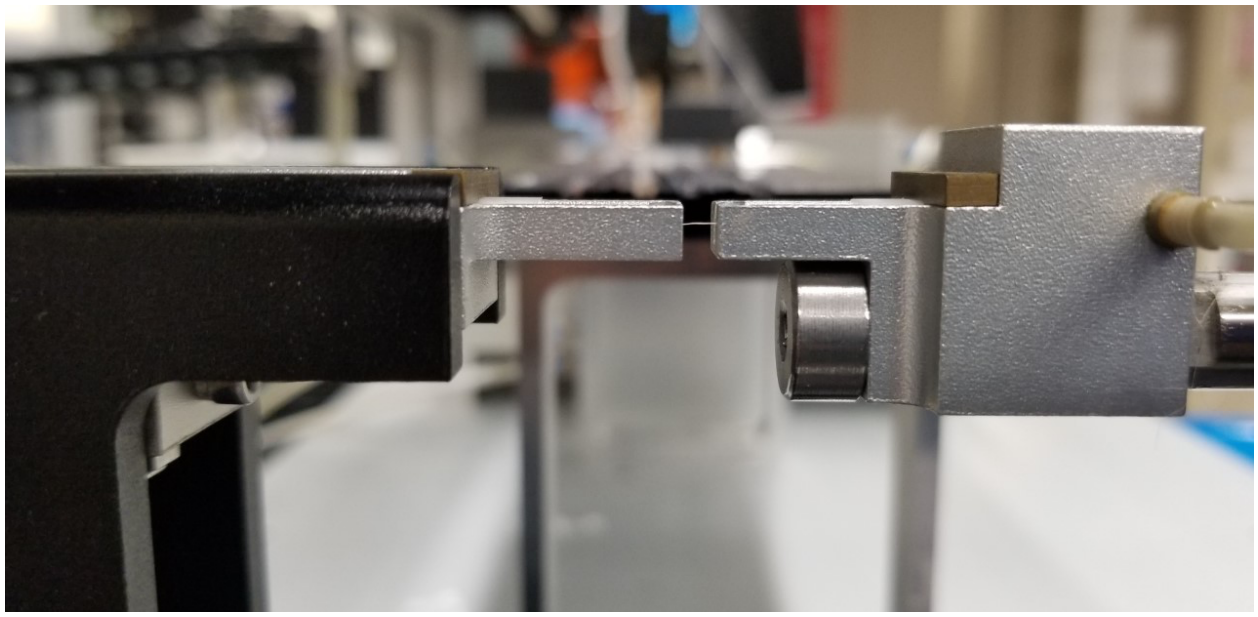

Figure 5.7. Tensile test of a fiber.

In total, 40 fibers were tested in this study and after the tensile test, the data was extracted and analyzed to find the diameter, tensile strength, axial elastic modulus, and failure strain of the fibers.

5.2.2. Result and discussion

5.2.2.1. Determination of diameter

The diameter of each kenaf microfiber was measured at three places along its length and the average was recorded by the TARDIS setup. The average diameter of the kenaf microfiber was found as 62.3 ± 8.5 μm which satisfies the diameter suggested in the literature [157]. It also implies that we were able to extract the microfiber for the study. However, the smallest diameter was found 55.23 μm where the largest diameter of kenaf microfiber was found as 80.64 μm.

5.2.2.2. Tensile test

A quasi-static tensile test was performed maintaining the test parameters. After the diameter determination, the fiber was directly taken to the tensile test set up. From the tensile test of the fibers, stress-strain curves were obtained. There were three regions observed in a curve:

toe region, linear region, and failure region. Figure 5.8 shows a representative curve of a kenaf microfiber representing all three regions of the curve.

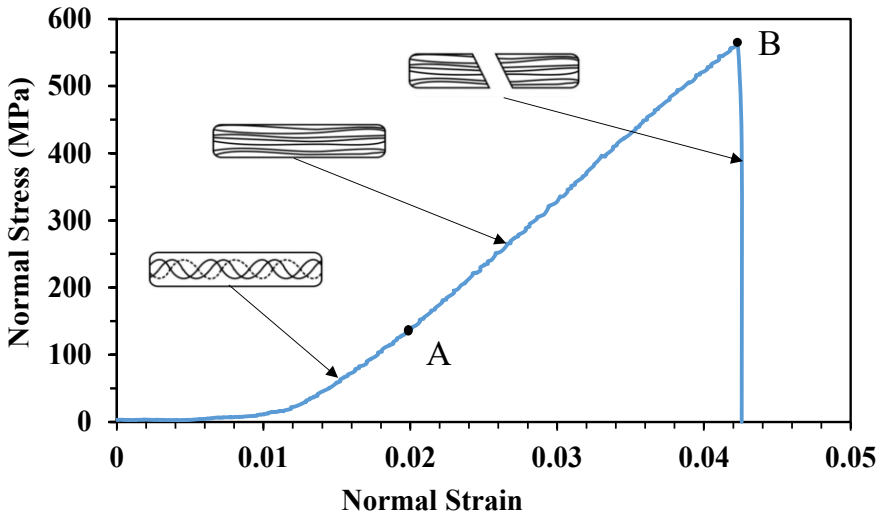

Figure 5.8. Stress-strain curve of a representative kenaf microfiber showing three different regions.

Up to about 1.6% of strain (point a), the curve is showing the toe region. At this stage, the entanglements and curled nanofibrils of the kenaf microfiber start to stretch out and become uncrimped. As the stress further increases, the fibrils straighten, and the linear portion of the curve starts.

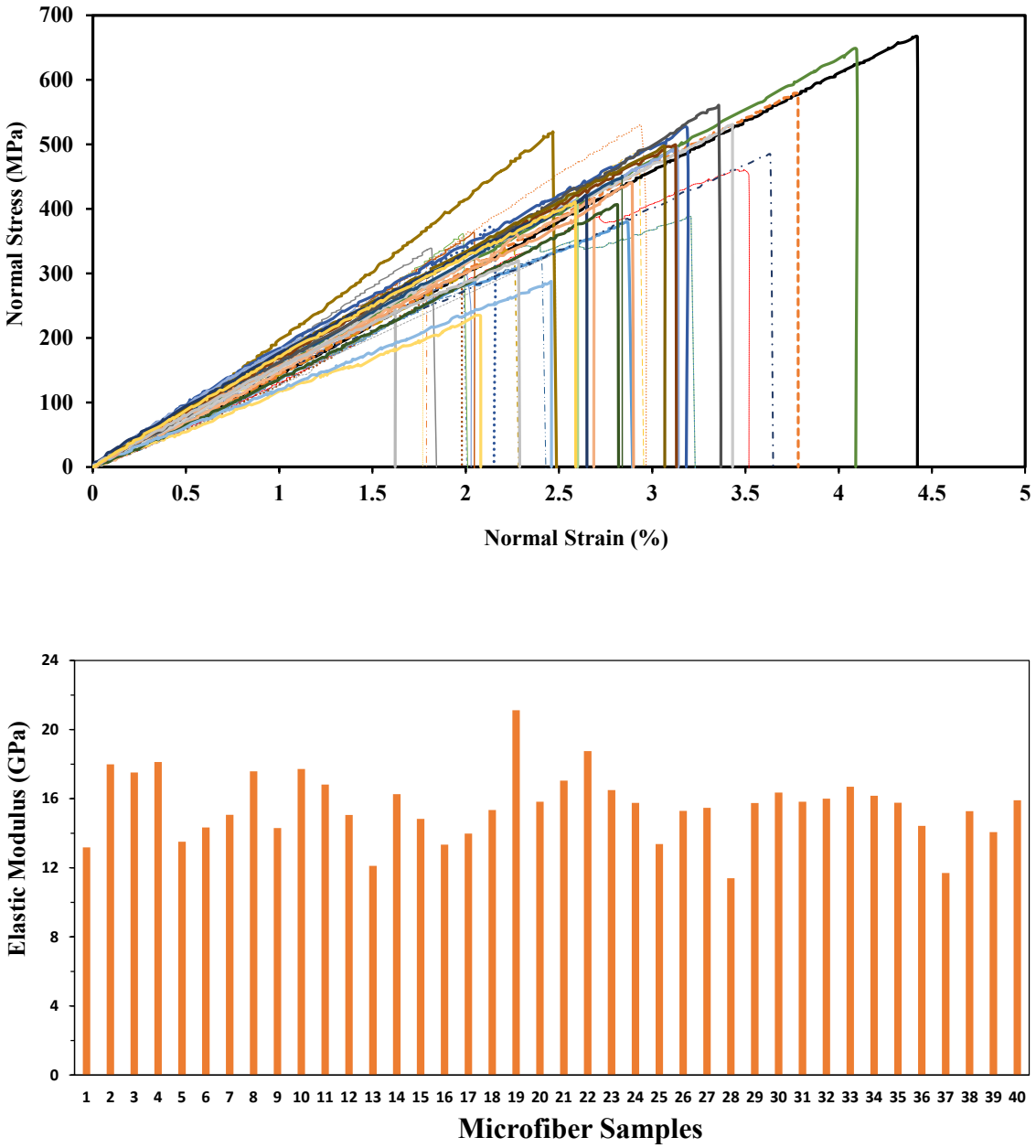

Figure 5.9. (a) Stress-Strain curve of kenaf microfiber samples; (b) Axial elastic moduli of samples.

The slope of the linear portion has been taken as the axial elastic modulus of kenaf microfiber. As soon as the normal stress reaches point b, the linear region ends where the rest of the portion of the curve is the failure region. The b point has been marked as ultimate strength

and the strain at that point has been taken as failure strain. The mode of failure of the kenaf microfibers has been found as brittles failure.

Figure 5.9 (a) is the stress-strain curves of all the kenaf microfibers subjected to the tensile test where the toe region has been excluded to show the linear portion of the curve. The stress-strain curves were found almost repetitive. The slopes of the curves have been determined as axial elastic modulus and have been presented as a bar chart in Figure 5.9 (b). The average elastic modulus of kenaf microfiber has been calculated as 15.54±1.95 GPa which is lower than the elastic moduli presented in the literature review section. There are several reasons why elastic modulus can vary. The first is the small gauge length we have chosen. Literature has shown a similar scenario for other natural fibers, e.g., bamboo, jute, coir, where axial elastic modulus was found low for small gauge length , and where it increases with the increase of gauge length [158]. Jute is a bast fiber that has a similar structure to kenaf. The average axial elastic modulus of jute was found to be 8.68 GPa when the gauge length is 5 mm, and increases up to 27.3 GPa as the gauge length reaches 35 mm. For 10 mm gauge length, their calculated average axial elastic modulus was 14.83 GPa which is similar to our experimental result [158]. A similar fashion of axial elastic moduli has been found by Pan et al.. They additionally showed tensile strength remains unchanged and failure strain increases with the increase of gauge length [159]. Figure 5.10 shows the influence of gauge length change on axial elastic modulus, failure strain, and tensile strength [159].

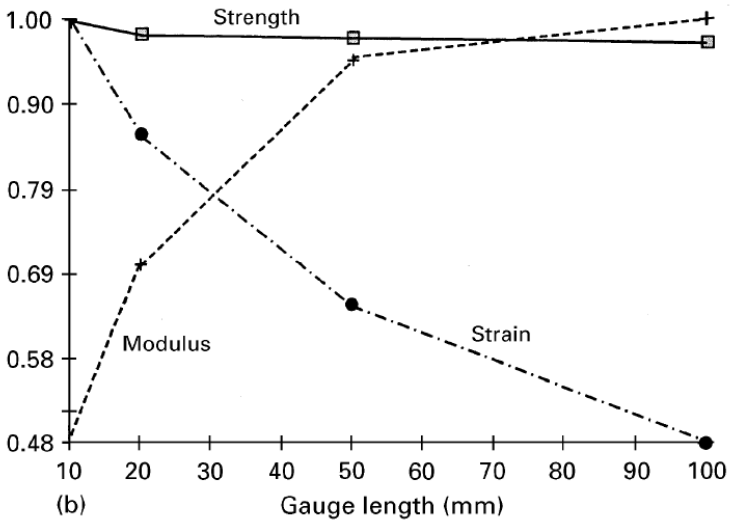

Figure 5.10. Effect of changing gauge length on axial elastic modulus, failure strain, and tensile strength [159].

Additionally, the quality of microfibers depends on the source and weather condition where it is cultivated. Shinji et al. showed how the axial elastic modulus can vary when kenaf plant length is changed which has been shown in figure 1.23 (b) [119]. Elastic modulus between 12-33 GPa has been found for their sample with different plant lengths. On top of that, the kenaf microfiber used in this research was a dried sample without any chemical modification or surface treatment and there were cracks and impurities on the surface as found from AFM surface morphology, which can stand as other reasons for low elastic modulus.

Figure 5.11 is a combined bar chart of ultimate strength and failure strain. The black bars in the bar chart show the ultimate strength of different microfibers and the orange bars represent the failure strain. The average ultimate strength of the microfibers was found as 453.31 ± 116.13 MPa. On the other hand, the average failure of the strain of the kenaf microfibers has been determined as (4.37 ± 1.36) %. Here a higher value of tensile strength and failure strain has been observed which resulted from our consideration of a continuous single strand of kenaf microfiber where the gauge length is small.

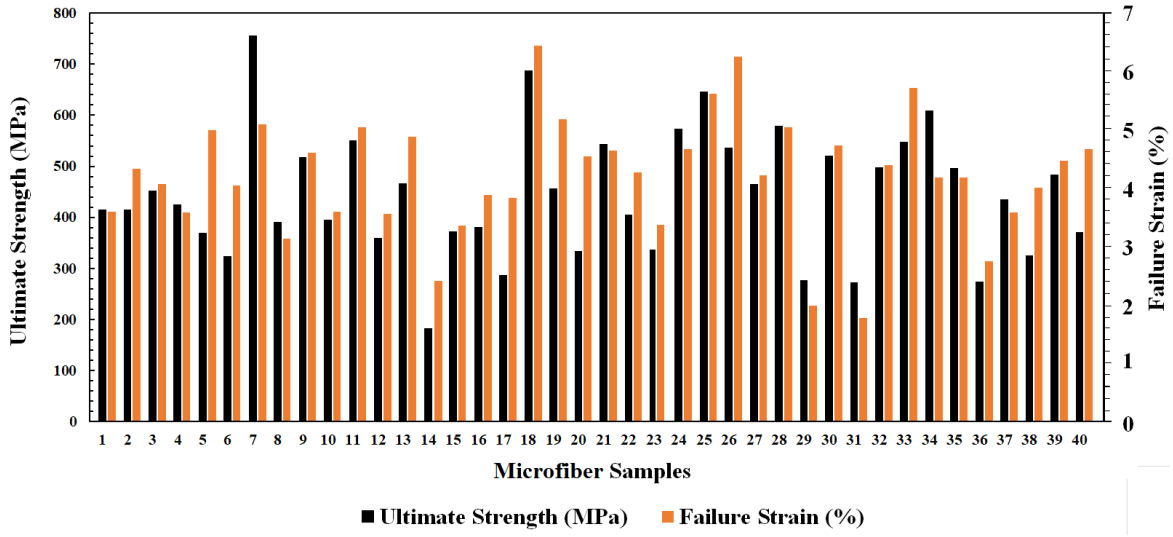

Figure 5.11. Ultimate strength (shown by black bars) and failure strain (shown by orange bars) of microfiber samples.

5.2.3. Statistical analysis of failure

For the materials like natural fiber, merely average and standard deviation are not enough to predict the failure where it is clear from Figure 5.11 that many of the microfibers fail below the average Strength or failure strain. Hence, a statistical reliability analysis is important to predict failure. The tensile strength and failure strain were subjected to statistical analysis to predict the failure and quantify the probability of failure for a certain applied load. Different established statistical models can be used in this regard. However, for the failure of brittle materials, Weibull distribution has been successfully used in the literature to characterize the tensile strength [160]. From the result of the tensile test, the tensile strength and failure strain data were used to generate the probability curve and distribution curve using the Weibull distribution equation.

5.2.3.1. Weibull distribution

The Weibull distribution is popular in reliability engineering that is used in lifetime distribution. From the perspective of probability theory and statistics, it is a kind of continuous

probability distribution. The distribution has been named after a Swedish mathematician Waloddi Weibull, who described it in detail in 1951. However, this distribution was first introduced by Fréchet in 1927 where Rosin & Rammler were the first to use the distribution to describe a particle size distribution in 1933. The Weibull probability density function with three parameters (scale, shape, and location parameter) is expressed as follows:

$$P(\sigma_f) = \frac{m}{\sigma_o}\left(\frac{\sigma_f-\gamma}{\sigma_o}\right)^{m-1} . e^{-\left(\frac{\sigma_f-\gamma}{\sigma_o}\right)^m} \quad (5.7)$$

Here, $P(\sigma)$ is the probability function that simply indicates the probability of an event (e.g. failure) at a certain applied parameter (e.g. applied stress, strain, etc.). σ_o is called Weibull modulus or scale factor where γ is threshold or location parameter. Using the experimental data in a least-square fitting, the three parameters are determined for a set of data. Integration of equation (5.7) yields the cumulative probability equation (5.8).

$$P(\sigma_f) = 1 - e^{-\left(\frac{\sigma_f-\gamma}{\sigma_o}\right)^m} \quad (5.8)$$

Besides, it is also possible to quantify the average and standard deviation of a set of data under Weibull analysis. The equation (5.10) and (5.11) are used to determine Weibull average and standard deviation, respectively, where Γ is called the Gamma function.

$$\bar{\sigma} = \gamma + \sigma_o . \Gamma(\frac{1}{m} + 1) \quad (5.9)$$

$$\sigma = \sigma_o \sqrt{\Gamma\left(\frac{2}{m} + 1\right) - \left\{\Gamma\left(\frac{1}{m} + 1\right)\right\}^2} \quad (5.10)$$

5.2.3.2. Weibull analysis of tensile strength

From the least square fitting of the experimental data, the values of location, scale, and shape factor were calculated as 121.4, 370.5 MPa, and 3.105, respectively. Before applying the Weibull distribution, the applicability of this distribution was assessed. A Weibull cumulative

failure percentage vs. ultimate strength curve was drawn at a 95% confidence interval using the location, scale, and shape parameters applying equation (5.8).

Figure 5.12 shows a log-log graph of failure percentage vs. ultimate strength where the blue dots denote the cumulative probability of failure at different ultimate strengths determined from tensile tests. On the other hand, the middle red line is the failure probability found from the Weibull equation for the three Weibull parameters. The left and right lines are lower and upper bound values of ultimate strength respectively for a certain probability of failure.

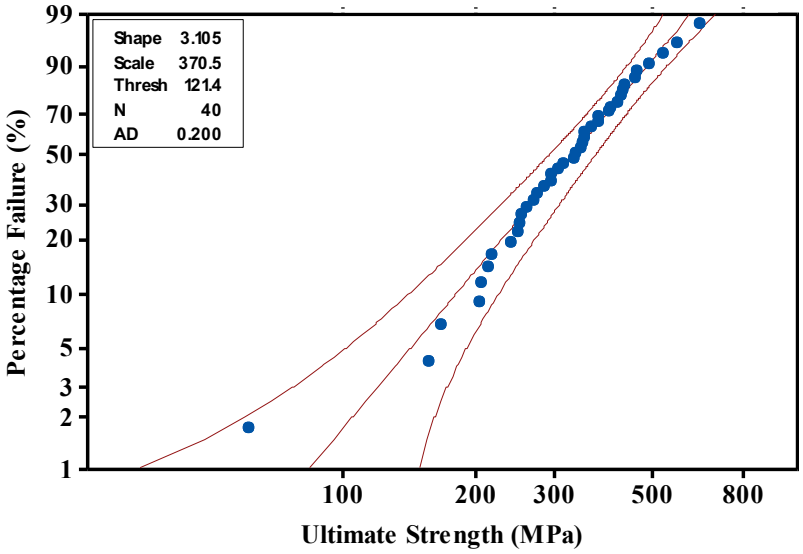

Figure 5.12. Weibull analysis compatibility test for ultimate strength.

Anderson-Darling (AD) goodness-of-fit has been calculated to determine the level of fit. It determines how well a set of data follow a certain distribution by measuring the area between the fitted line and an empirical/theoretical distribution's value. The less the area is, the smaller the AD value becomes indicating a better fit. For our case, AD is found as 0.2. As the value is very low, it implies the quality of fit of our data with the Weibull cumulative distribution curve is high. Hence, we can conclude, Weibull distribution can be successfully applied for predicting failure at different ultimate strengths.

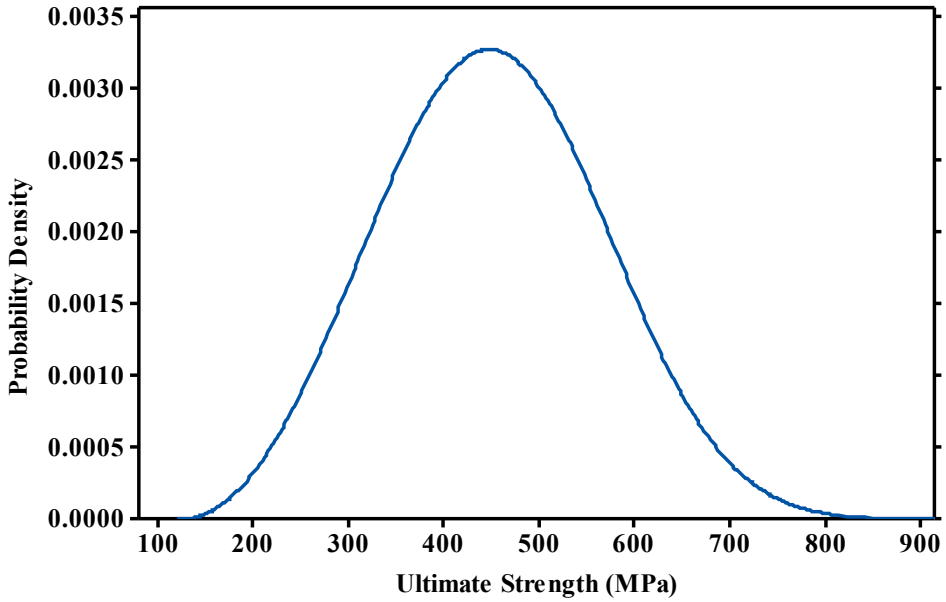

Figure 5.13. Weibull distribution of ultimate strength.

Using the location, scale, and shape parameter in equation (5.7), Figure 5.13 has been generated. Here, the probabilities of kenaf microfibers' to possess different ultimate strengths have been suggested. The probability density for a certain ultimate strength denotes the probability of failure of a fiber under the normal stress associated with the ultimate strength. The total area under the curve is 1 and the area under the curve lying left to a certain ultimate strength is the cumulative probability of a sample to possess that strength or below that. Hence, for a particular ultimate strength, the area of the left of the point under the curve indicates the total probability of failure at normal stress associated with the ultimate strength or below that.

Using equations (5.09) and (5.10), the average ultimate strength and standard deviation were determined which are 451.145 MPa and 116.47 MPa, respectively. The average and standard deviation of the ultimate strength were found to be very close to the value determined in the previous section.

5.2.3.3. Weibull analysis of failure strain

Similar to ultimate strength, the values of location, scale, and shape factor were determined from the least square fitting. The value of location, scale, and shape factor were calculated as 0.7525, 3.798%, and 3.889, respectively. Before applying the Weibull distribution, the applicability of this distribution was assessed. A log-log cumulative Weibull failure percentage vs. failure strain curve was drawn at a 95% confidence interval using location, scale, and shape parameters using equation (5.8).

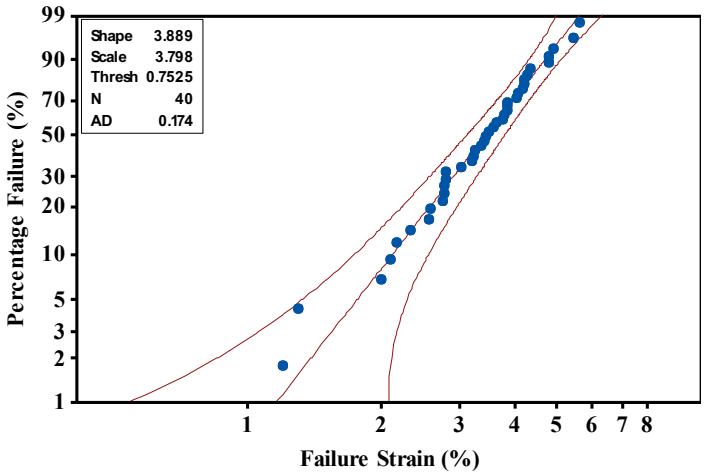

Figure 5.14. Weibull analysis compatibility test for failure strain.

Figure 5.14 shows the failure percentage vs. failure strain curve where the blue dots are the cumulative probability of failure at different failure strains determined from tensile tests. On the other hand, the middle red line is the cumulative probability of failure found from the Weibull equation using the parameters. The left and right lines are lower and upper bound values of ultimate strength respectively for a certain probability of failure.

Anderson-Darling (AD) goodness-of-fit has been calculated to determine the level of fit which was found as 0.174. The low value of AD implies the quality of fit of our data with the Weibull cumulative distribution curve is excellent. Hence, we can conclude, Weibull distribution can be successfully applied for predicting failure for different failure strains.

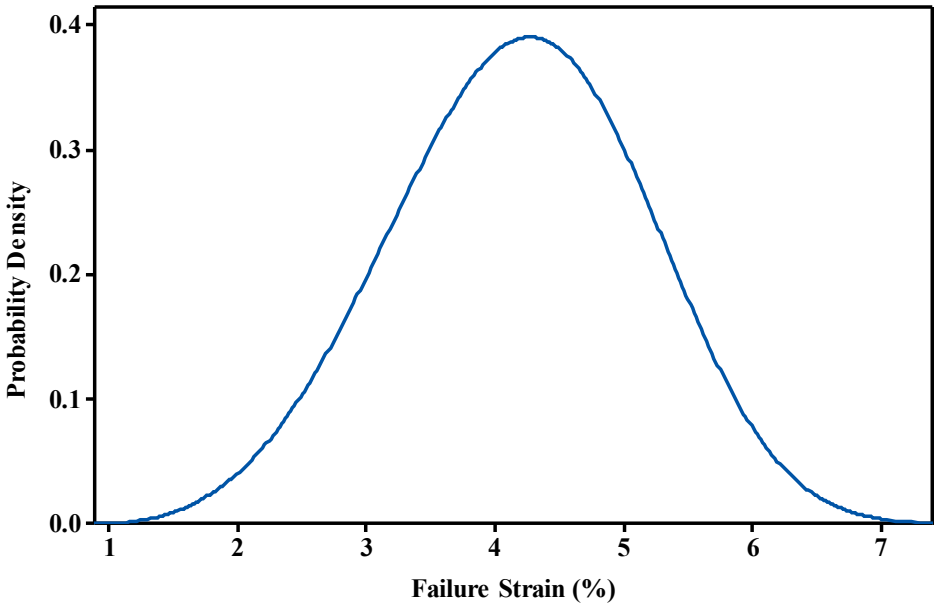

Figure 5.15. Weibull distribution of failure strain.

Using the location, scale, and shape parameter in equation (5.7), Figure 5.15 has been drawn where the probabilities of kenaf microfibers' failure at different failure strains have been quantified. The probability density for a certain failure strain denotes the probability of failure of a fiber at that strain. The total area under the curve is 1 and the area under the curve that is left to a certain failure strain is the cumulative probability of a sample's failure at that or below that particular strain. Therefore, for a particular failure strain, the left lying area of the strain under the curve indicates the total probability of failure at a certain strain or below that.

Using equations (5.9) and (5.10), the average failure strain and standard deviation were determined which are 4.19% and 0.99%, respectively. The average and standard deviation of the ultimate strength were found to be very close to the value determined in the previous section.

5.3. Conclusion

The transverse and axial elastic modulus of kenaf microfiber has been characterized in this study. The AFM-based study of kenaf microfiber suggests a novel technique to determine transverse elastic modulus that focuses on the nanomechanical characterization of individual

kenaf microfibers. Surface topography of the fiber was scanned utilizing AFM and later AFM-based nanoindentation was performed to determine the transverse elastic modulus of the kenaf microfiber. The extended JKR model was chosen that considers the adhesive force between the AFM probe and kenaf microfiber. Different elastic moduli from the model were compared with the extracted data from the experiment to determine the elastic modulus of kenaf microfiber. The transverse elastic modulus of kenaf microfiber was determined as 2.33±0.05 GPa. Additionally, the axial elastic modulus of a single kenaf microfiber was determined by an Instron micro tensile test set up. The axial elastic modulus, tensile strength, and failure strain were also characterized in the study. The axial elastic modulus, ultimate strength, and failure strain were determined as 15.54±1.95 GPa, 453.±116.13 MPa, and 4.37±1.36 %, respectively, where the reason of the low axial elastic modulus has been explained that is due to low gauge length, growing condition, and imperfections in the fiber. Additionally, the tensile strength and failure strain were analyzed further by 3-parameters Weibull distribution to predict the failure for certain stress and strain. Hence, the probability density and cumulative probability for tensile strength and failure strain can be easily estimated from the distribution curve generated in the analysis section. However, the experimental procedures used for the kenaf microfiber can be used to establish protocol to characterize other plant-based natural microfibers to find an accurate elastic modulus. Hence, the study can be able to address a significant gap in the literature associated with microfiber characterization.

6. DETERMINATION OF ELASTIC MODULUS OF CELLULOSE NANOFIBRIL[2]

In this chapter, the measurement of the axial and transverse elastic modulus of cellulose nanofibril and their analysis have been presented. Besides, the results have been compared with the literature and the validity of the result has been assessed.

6.1. Determination of transverse elastic modulus of cellulose nanofibril

The measurement of the transverse elastic modulus of cellulose nanofibril has been discussed in this section. As discussed before, cellulose nanofibril (CNF) is the fundamental unit of almost all types of natural fibers and is regarded as one of the main factors that influence their mechanical properties. Besides, owing to having a high aspect ratio, it is increasingly being used in the research of nanocomposite as a reinforcement recently. In order to utilize CNF as reinforcement more effectively, it is important to have a comprehensive idea of the mechanical properties of individual CNFs. Most of the studies are focused on the elastic modulus in the longitudinal direction, but the study of the elastic modulus in the transverse direction is still lacking. In this study, a single strand of CNF was subjected to an atomic force microscopy to characterize the surface morphology of CNF and determine the transverse elastic modulus through nanoindentation.

6.1.1. Material and experimental procedures

CNF was collected from The Process Development Center, the University of Maine and was stored at 40° F. A 0.03 M solution of CNF was prepared with water to make the sample. The

[2] The material in this chapter was co-authored by M Subbir Parvej, Dr. Xinnan Wang, and Dr. Long Jiang. M Subbir Parvej had primary responsibility for sample preparation and experimental data collection from testing and imaging. M Subbir Parvej was the primary developer of the conclusions that are advanced here. M Subbir Parvej also drafted and revised all versions of this chapter. Dr. Xinnan Wang and Dr. Long Jiang provided guidance and support during experimentation, proofread, and checked the math and logic of conclusions The majority of the section, by the listed authors, was originally published by SAGE in the Journal of Composite Materials [161]. Parvej, M.S., X.N. Wang, and L. Jiang, *AFM based nanomechanical characterization of cellulose nanofibril.* Ibid.2020. **54**(28): p. 4487-4493. and is reused here with permission.

solution was sonicated with Misonix 3000 sonicator at a power of 150 W for 1.5 minutes for dispersion. Next, the sonicated solution of CNF was smeared on a clean silicon wafer and was placed in an oven for 24 hours at 140° F to evaporate the water and leave CNF on the silicon wafer. The moisture content in CNF was determined by a Computrac Moisture Analyzer which was found on an average of less than 1%. The surface morphology of CNF was scanned by the AFM. Tapping mode was used to scan the CNF surface with a 15 nm-radius probe (Bruker: SNL 10). The transverse elastic modulus was determined by AFM-based nanoindentation. The scan size was gradually reduced from 300 nm × 300 nm to 1 nm × 1 nm to ensure the indentation was performed on the top of the CNF surface. Rupture of the CNF sample was avoided by setting indentation voltage for the piezo sensor as low as 0.05 V. A voltage was induced to the piezo sensor with the displacement of the probe along the z-axis as the probe tip starts to press the CNF sample. The indentation on CNF was continued until the voltage at the piezo sensor reaches 0.05 V. 8 indentations were performed at different locations of the 6 individual CNFs. The deflection data was the result of the combined deformation of both CNF and the AFM cantilever. To determine the deformation on the CNF only, the deformation of the AFM cantilever is needed to be extracted from the combined deflection data. Hence, indentations were also carried out on the silicon wafer. The induced voltage was converted into indentation force by multiplying it with the sensitivity and spring constant where the spring constant was determined by using the Sader method [162].

6.1.2. Result and discussion

The 2D AFM surface image of a representative CNF is shown in Figure 6.1 where the inset shows a sample with an average height (diameter) of 7.41 nm. The average of the diameters of 6 samples was found as 7.47 nm with a standard deviation of 0.86 nm.

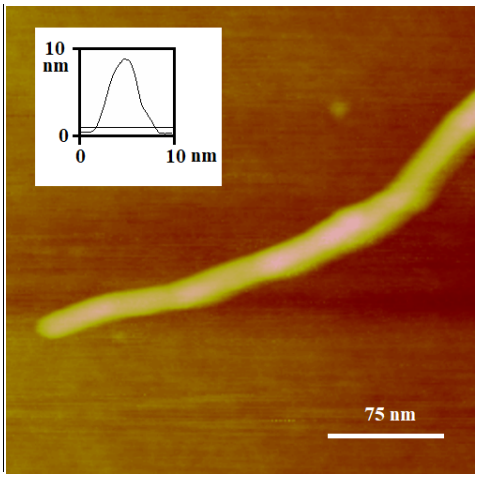

Figure 6.1. 2D AFM surface image of CNF; Inset: average height of CNF [161].

Figure 6.1 shows the indentation force vs Z-piezo displacement (F-z) curves for CNF and silicon wafer. Two parts of the curves are included in the indentation process: extension and retraction. While the AFM cantilever is approaching the CNF sample, a sudden drop of force in the extension curve is observed. This is due to the van der Waals forces acting between the sample and the AFM probe tip. This phenomenon is termed as 'jump to contact' and the probe continues to come down to indent on the sample surface. The indentation takes place until the voltage induced in the piezo-sensor reaches a certain value, i.e., 0.05 V for this study. The sample deformation is the difference of deformations between figure 6.2(a) and 6.2(b) under equal forces.

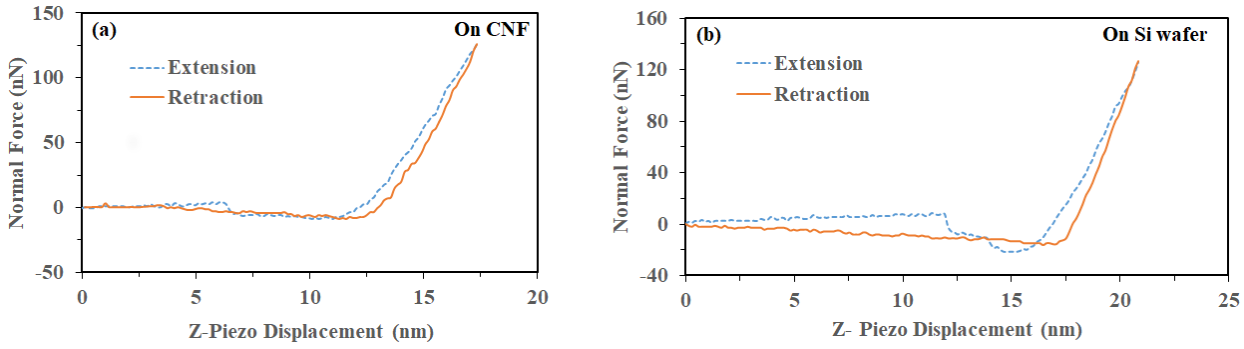

Figure 6.2. AFM nanoindentation curve for (a) CNF, and (b) silicon wafer [161].

6.1.3. Theoretical analysis

The Extended JKR model was chosen for the same reason as discussed in chapter 5 and equations (5.1) -(5.6) were used in this analysis. The radius of the CNF was determined from the AFM height images where the nanoindenter manufacturer's datasheet provided the radius, elastic modulus, and Poisson's ratio of the nanoindenter. In this study, the radius (R_i), elastic modulus (E_1), and Poisson's ratio (ν_1) of the AFM probe were 15 nm, 150 GPa, and 0.27, respectively. The Poisson's ratio of CNF was taken as 0.3 [163].

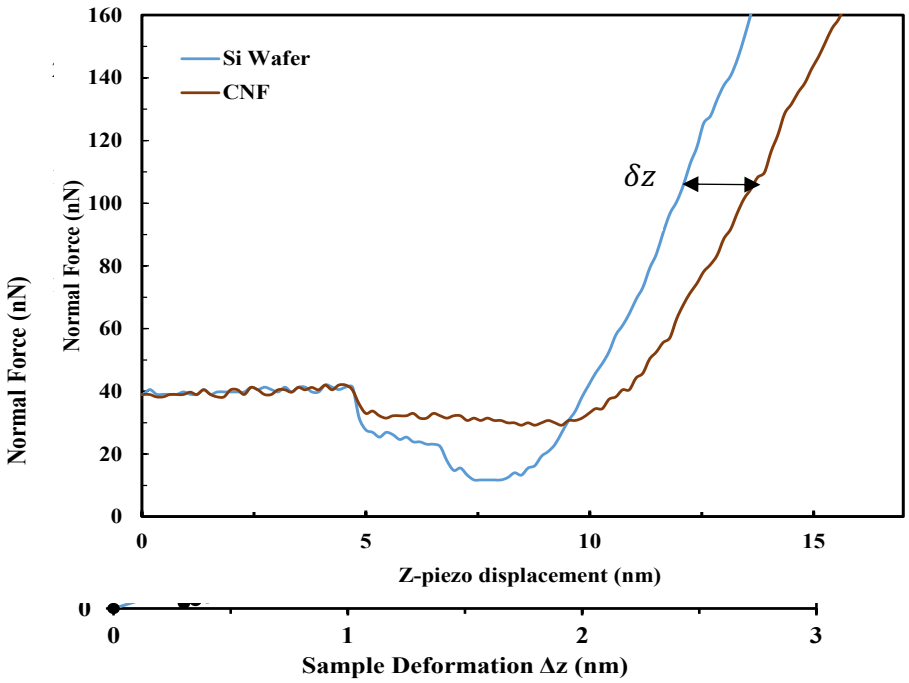

Figure 6.3. (a) Combined $F - z$ curve of CNF and silicon wafer indentation (b) Normal forces vs sample deformation curve; Inset: Coefficient of determination [161].

The best fit curve is presented in Figure 6.3 (b) which is obtained for 6.9 GPa. Additionally, the inset depicts the maximum R^2 was found as 0.90 for the elastic modulus 6.9 GPa. This transverse elastic modulus determined in this study is lower than the longitudinal elastic modulus presented by literature satisfying our hypothesis [113, 164]. The higher

longitudinal modulus of CNF also implies its higher load carrying capability across the longitudinal direction. The higher elastic modulus in the longitudinal direction can be elucidated from the structure of cellulose which is a chain of glycoside bonded numerous pyranose units strengthening the chain in the longitudinal direction [72]. Moreover, the transverse elastic modulus of CNF has been found comparatively lower than that of CNC measured by AFM nanoindentation [105]. It clearly shows the effect of the amorphous portion of CNF which is expected to possess a lower elastic modulus owing to its lower crystallinity [165]. However, the transverse elastic modulus is particularly important for an anisotropic material like CNF where properties in every possible plane can provide us information. The transverse elastic modulus can be used in the studies to determine shear modulus and torsional strength [126, 127]. Hereby, the study can contribute to the exploration and growth of a sound idea about the mechanical properties of CNF.

6.2. Determination axial elastic modulus of cellulose nanofibril

In this section, the measurement of the axial elastic modulus of cellulose nanofibril has been discussed. Literature shows a good number of studies in this regard and the measurement of axial elastic modulus of cellulose nanofibril has been done mostly for a bundle of fibrils. However, the method has some errors which has been discussed in the previous chapters. In the current approach, CNFs were spread on a microfabricated grid with square holes and a single strand of CNF was subjected to an atomic force microscopy-based 3-points bending to determine the transverse elastic modulus through nanoindentation.

6.2.1. Material and experimental procedures

The same type of CNF has been used as the previous section, which was collected from The Process Development Center, University of Maine and stored at 40° F. A 0.03 M solution of

CNF was prepared with water to make the sample similarly which was sonicated with Misonix 3000 sonicator at a power of 10 W for 1.5 minutes for dispersion. In the next step, the sonicated solution of CNF was smeared on a clean pit array and was placed in an oven for 24 hours at 140° F to evaporate the water and leave CNF on the silicon wafer. The pit array is an array of pits with a known depth that is usually used to calibrate the AFM. However, in this study, it has been used to facilitate the 3 points bending of CNF. The model name of the pit array used in this study is VGRP 15m from Bruker Company which had a pitch length of 5 μm and depth of 180 nm. The AFM scan of the pit array has been shown in Figure 6.4.

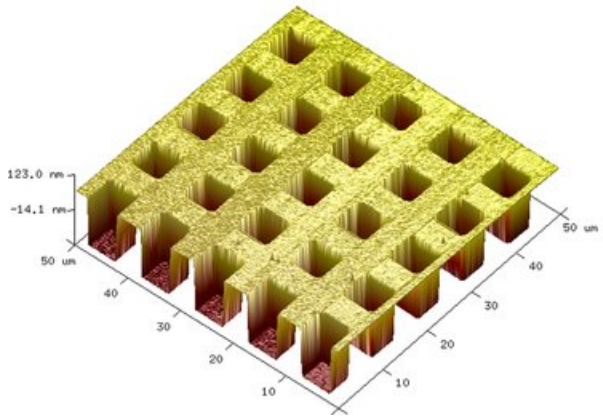

Figure 6.4. An AFM scan of a pit array used in a study with 10 μm pitch and 180 nm depth [166].

The moisture content in CNF was determined by a Computrac Moisture Analyzer which was found on an average of less than 1%. The axial elastic modulus was determined by AFM-based 3 points bending. The experimental setup has been illustrated in Figure 6.5. According to the Figure, the edge of the pit works as a support of the CNF when the AFM probe works as the indenter to cause deflection at the half-length (L/2) of the CNF fiber.

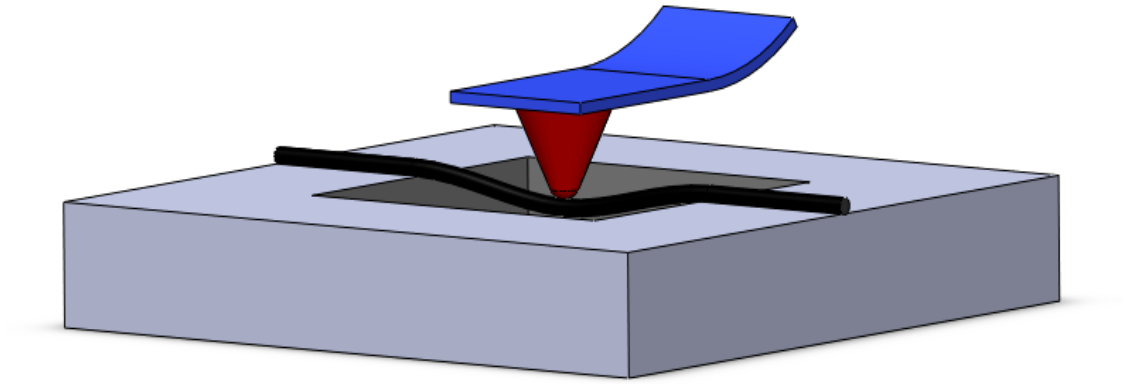

Figure 6.5. A schematic of AFM-based 3 points bending of CNF.

The surface morphology and the depth of the pit array were scanned on what CNF was spread. Tapping mode was activated to scan the total surface morphology of the setup with a 15 nm-radius probe (Bruker: SNL 10). Some best spots were selected where the orientations of CNF were similar to the schematic and the CNF can be considered as a beam. Figure 6.6 shows a representative AFM-scanned surface morphology of the 3-points bending setup that gives an idea about the orientation of the fiber on the pit array.

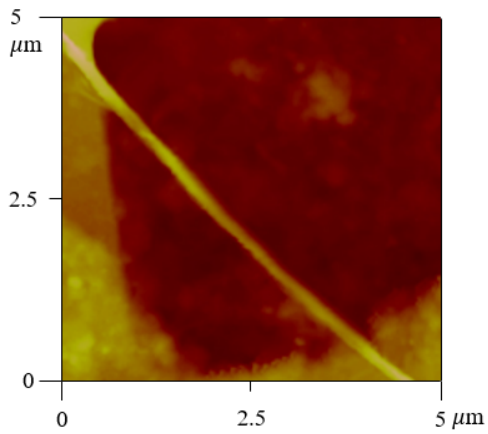

Figure 6.6. CNF sample for 3-points bending on pit array.

To perform the 3-points bending, the nanoindentation mode was set where the rupture of the CNF sample was avoided by setting indentation voltage for the piezo sensor as low as 0.01 V. A voltage was induced to the piezo sensor with the displacement of the probe along the z-axis

as the probe tip starts to press the suspended CNF between the edges of the pit. The indentation on CNF was continued until the voltage at the piezo sensor reaches 0.01 V. 3 tests were performed at different locations of the pit array. To determine the 3-points bending deformation for the CNF beam, the deformation of a reference is needed to be subtracted from the deformation of the AFM probe found in the test initially. Hence, indentations were also carried out on the silicon wafer. The induced voltage from the interaction between the sample and the probe was converted into indentation force by multiplying it with the sensitivity and spring constant where the spring constant was determined by using the Sader method [162].

6.2.2. Determination of CNF deflection

One of the most important steps to calculate the axial elastic modulus of CNF through 3 points bending is to find the deflection of the CNF beam while subjected to bending. A representative force-displacement (F-z) curve has been shown in Figure 6.8 (a) which has been derived from the AFM-based 3-points bending experiment on the representative fiber shown in Figure 6.6. The 3-point bending curve contains two types of information: the deflection of the cantilever and the deflection of CNF where we need to eliminate the deflection of the cantilever from it. Compared to the deflection of CNF, the deflection of Si wafer is very negligible for what it can be regarded as a rigid substance. Hence, for the same force applied to the CNF beam, it will contain only the deflection of the cantilever and there will be no deflection of the tip into the surface. The CNF beam deflection, $\Delta\delta$ was found by subtracting the displacement on Si wafer substrate from the displacement on the CNF beam. The retraction curve of nanoindentation on a reference Si wafer substrate (marked with blue line) has been coupled with the 3-points bending curve (marked with orange line) in Figure 6.7 (a). For different forces, the beam deflection has been calculated. The data was used to form a force-beam deflection (F- $\Delta\delta$) curve as shown in

Figure 6.7 (b). The slope of this curve is $\frac{F}{\Delta\delta}$ that will be used later in Euler beam equation to find the axial elastic modulus.

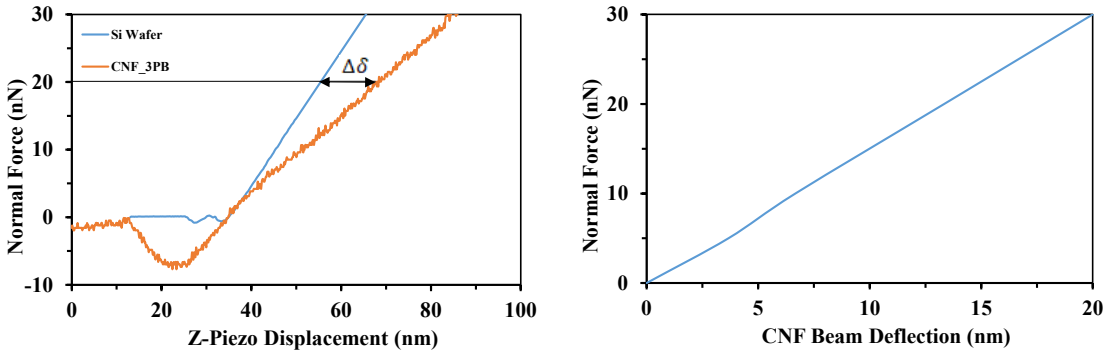

Figure 6.7. (a) Combined $F - z$ curve of CNF 3-points bending and silicon wafer indentation; (b) Force-beam deflection (F- $\Delta\delta$) curve.

6.2.3. Result and theoretical analysis

The action of deflection of a beam under the influence of a certain force consists of both bending and shear deformations. However, with the increase of the length to diameter ratio, the effect of shear deformation starts to become insignificant [167, 168]. As the length to diameter ratio is more than 8 in the current study, equation (8.1) was used to quantify the axial elastic modulus of CNF that is a pure bending formula [167].

$$E = \frac{FL^3}{192\Delta\delta I} \tag{6.1}$$

Here, F is the force that is concentrated on the CNF beam, L is the span length, $\Delta\delta$ is the deflection, and I is the second moment of inertia of the circular section of the CNF strand.

However, there are a few assumptions that have been adopted while considering the pure bending formula. Firstly, the cross-section of the CNF has been taken as a circular cross-section though the beam doesn't need to have a circular cross-section all the time. Secondly, both end of the CNF strand has been regarded as fixed. As the sample was dried, a van der Waals bond was created between the CNF and the pit array. The adhesion between the pit array and the CNF

sample was high enough compared to the small load at the mid-span for what the assumption was made. Thirdly, the CNF strand has been regarded as fully elastic.

For the fiber shown in Figure 6.6, the diameter was found 106.5 nm where the strand length was 4800 nm. From Figure 6.7 (b), the slope of F- $\Delta\delta$ was found 1.5 nN/nm.

Using the data in equation (8.1), the axial elastic modulus of CNF was determined as 136.8 GPa. The mean of the three samples was found at 138.38 GPa with a standard deviation of 2.82 GPa. The axial elastic modulus determined in this study aligns with the existing results presented in the literature. In the AFM-based 3-points bending on CNF, Cheng et al. found the modulus as 93 GPa while experimenting on a CNF bundle of 270 nm [113]. Hsieh et al. presented Raman spectroscopy-based technique to determine the axial elastic modulus of a single filament and obtained 114 GPa where Guhados et al. used AFM to determine the forces with sub-nanonewton sensitivity at the nanometer scale to measure axial elastic modulus 78 ±17 GPa [109, 110]. However, in the AFM based 3-points bending of this study, a single CNF strand of 135 nm was considered, and a higher modulus was determined that supports the experimental results obtained from different kind of setups.

6.3 Summary

CNF is one of the most important constituent elements of the plant-based natural fibers that contribute significantly to its overall mechanical properties. Besides, recently the usage of CNF as reinforcement in nanocomposites is increasing. Hence, it is important to know the elastic modulus accurately. The study in this chapter determines the elastic modulus of CNF in the axial and longitudinal directions. The study of transverse elastic modulus aims at the AFM-based nanomechanical characterization of a single strand of CNF and compensates for the information gap in the literature. The surface morphology was investigated through AFM scanning while

transverse elastic modulus was determined by AFM-based nanoindentation. The Extended JKR model was used and an exclusive shooting model was employed to determine the transverse elastic modulus of CNF as 6.9±0.4 GPa. Besides, the CNF was spread on a pit array and CNFs with the orientation resembling to simply supported beam were selected for a 3-points bending test. AFM nanoindentation mode was selected for a 3-points bending test and the data was compared with silicon wafer indentation data to determine the deflection of the beam at the midspan for different forces. The Euler beam formula was used to calculate the axial elastic modulus which was found as 138.38±2.82 GPa. However, the moduli determined in this study were compared with the literature which aligned well with that and can address the information gap in the literature. Besides, another important aspect of this study is the experimental procedures and protocol adopted. Though there are ample studies on the axial elastic modulus, the transverse elastic modulus is less pronounced and studied property of different nanofibrils. The study can easily be replicated for the other natural or synthetic nanofibrils to know their elastic moduli in the axial and longitudinal direction. Therefore, the study can be regarded as an important reference for the researchers working with the elastic modulus of different nanofibrils and their surface morphologies.

7. FUTURE STUDY

The research focuses on the surface morphology and elastic moduli of kenaf microfiber and CNF. AFM was involved to scan surface morphology, perform nanoindentation, and 3-points bending where an Instron set up was used to study the axial elastic modulus of kenaf microfiber. However, there are scopes to work further on this research. In this chapter, the scopes of future studies have been discussed.

7.1. Using different gauge length of kenaf microfiber

In this study, kenaf microfiber with 10 mm gauge length has been studied and a lower elastic modulus was determined from the study. However, there is a significant contribution of gauge length on the elastic modulus of bast fibers where the lower axial elastic moduli can stem from early rupture due to imperfection in the microfiber structure or discontinuity. Hence, it is necessary to perform tests for the other gauge lengths of kenaf microfibers as well.

7.2. Using microfabricated trenched surface for AFM 3-points bending

The axial elastic modulus of CNF was studied spreading CNF on a pit array where it was hard to find a CNF in a correct orientation that resembles completely like how an ideal Euler-Bernouli beam is used to be oriented. Though the nanofibril was expected to be parallel with the edge of the pit, the test was performed where the fibril was oriented diagonally. Therefore, the similar trenched surface used by Iwamoto et al. can ease the experiment and can be able to have a more similar orientation of Euler- Bernouli beam on the trench [112].

7.3. Using microfabricated trenched surface for AFM 3-points bending

In the 3 points bending test of CNF, the load was applied only on the mid-span of the CNF beam. However, there is a possibility of not indenting onto the intended position. Hence,

future experiments can focus on some other sites along the length of CNF additionally to increase the accuracy of the experiment.

7.4. Studying treated kenaf microfiber and CNF

The surface morphology reveals the presence of foreign particles and imperfection on the kenaf microfiber's surface. These imperfections and initial crack on a surface can cause early failure and fibers can fail at different stresses. Hence, to reduce the variation of the properties, chemical treatment can be done on the fiber before the application. For similar reasons and better performance, CNF can be functionalized. These treated kenaf microfibers and CNF can also be studied in the future.

7.5. Studying other bast fibers and nanofibrils

Bast fibers like hemp, flax, jute, etc., are some lucrative multipurpose products and have a great significance in various applications. Therefore, the experiment technique demonstrated in this thesis can be extended to study those bast fibers. Besides, elastic moduli of different nanofibrils can also be studied following the technique applied for CNF.

7.6. Model for axial to transverse elastic moduli conversion and calibration

It has been a quite pronounced problem to find a model or equation for the conversion of the elastic modulus of fiber between the axial and transverse direction. The data determined in the thesis can be helpful in the development of the model where it can be used to calibrate the model.

8. CONCLUSION

The elastic modulus of kenaf microfiber and cellulose nanofibril were determined both in the axial and transverse direction in this thesis. The thesis also suggests a novel method to estimate the transverse elastic modulus of different nano and microfibers through AFM-based nanomechanical characterization. The limitations of the previous methods adopted by the researchers in the literature have been taken into the account and were addressed in the current study which helps to determine more accurate values of the elastic moduli of kenaf microfiber and cellulose nanofibril for the fiber samples. The remarkable aspects of this thesis have been focused on below.

- The surface morphology of the kenaf microfiber has been revealed which shows the entangled microfibers, cracks, and imperfections on the surface. The transverse elastic modulus of the kenaf microfiber was characterized by AFM-based nanoindentation. To determine the transverse elastic modulus from the force versus sample deformation data, the extended JKR model was used. As the adhesion forces from the fiber surface are considered, the extended JKR model fits well with this case and can outperform the other existing models, e.g., Hertz, DMT, etc. The transverse elastic modulus of the kenaf fiber was found to be 2.33 ± 0.05 GPa. The moduli determined in this study is much lower than the values suggested in the literature. However, the nanofibrils in the kenaf microfibers are aligned in the axial direction and thus the axial elastic modulus suggested from the existing literature possesses a larger value. Hence, the transverse modulus determined in this study can be considered as an important contribution towards the literature..

- The axial elastic modulus of kenaf microfiber was determined by subjecting a single microfiber to an Instron fiber testing setup for a quasi-static tensile test. The stress-strain curves have been formed from the tensile tests of the samples and the mode of failure is found as a brittle failure. The axial elastic modulus, ultimate strength, and failure strain were determined as 15.54±1.95 GPa, 453.31±116.13 MPa, and (4.37±1.36) %, respectively. As expected, the axial elastic modulus is greater than the transverse elastic modulus where it lower value than the literature comes from the lower gauge length, growing condition, and defects on microfiber surface. The ultimate strength and failure strain were further analyzed with the 3-parameters Weibull statistical distribution to predict the failure of the kenaf microfiber accurately. According to the fashion of data and low AD parameter, the 3-parameter Weibull distribution was found to be the most appropriate one to interpret the experimental data. A single strand of microfiber was considered for tensile unlike most of the previous studies and therefore, the results can be expected to not have the error what bundle basis test results usually have.
- A single strand of CNF was subjected to an atomic force microscopy to characterize the surface morphology of CNF and determine the transverse elastic modulus through nanoindentation. The transverse elastic modulus of CNF was calculated to be 6.9 ± 0.4 GPa using extended the JKR model. However, most of the studies are focused on the elastic modulus of CNF in the longitudinal direction where the current study of the elastic modulus is in the transverse direction. Transverse elastic modulus is an important property to know an anisotropic material comprehensively. Therefore, the

experiment can serve as a significant source of protocol for future research focusing on the transverse elastic modulus of other nanofibrils.

- CNFs were spread on a pit array to determine the axial elastic modulus through an AFM-based 3-points bending test. Euler beam formula was applied to calculate the axial elastic modulus as 138.38±2.82 GPa. As a single strand of fibril was tested instead of a bundle of CNF what the previous studies performed, the modulus obtained through this process can be regarded as more acceptable data for future experiments and applications involving CNF. However, spreading the CNF on a microfabricated trenched surface can be able to improve the end condition of CNF and can bring it closer to simply supported beam condition to apply the Euler-Bernouli beam formula.

An important thing to note from the elastic moduli determined from the experiments is, the elastic moduli on the both axial and longitudinal direction for CNF are greater than those for kenaf microfiber where CNF is one of the most significant constituent elements of kenaf microfiber. The ambiguity can be explained from the orientation of the CNF in kenaf microfibers. There are many other fibrils in the structure of kenaf microfiber alongside CNF, e.g., hemicellulose, lignin, etc, which are weak. Besides, CNF and other fibrils in the kenaf microfibers form entanglements with angular orientation for which CNF cannot directly carry the load and thus the moduli of kenaf microfiber is lower. Besides, the imperfection, cracks, and defects on the kenaf microfiber's surface are also some other reasons of their low moduli. Similarly, the moduli of other cellulose-based natural fibers can also be explained. Additionally, the research also indicates the superiority of CNF as a reinforcement and it can possess a potential future in nanocomposites if the dispersion issue can be resolved.

The importance of the transverse elastic modulus of fibers is particularly mentionable. Fibers are anisotropic material, so, elastic moduli are not the same in all directions. Hence, it is essential to know the mechanical properties of kenaf microfiber in every possible direction. It helps us to choose a correct reinforcement fiber in the cases where fibers have to carry loads in the transverse direction. Transverse elastic modulus can also play a significant role to determine the shear modulus and Poisson's ratio of the fiber properly.

The thesis not only paves a way to address the issues in the previous research to determine the axial elastic modulus of kenaf microfiber and CNF, but also determines their elastic modulus in the transverse direction. Moreover, the protocol established for the transverse elastic modulus in this thesis can potentially help future researchers to find the transverse elastic moduli for other nano and microfibers.

REFERENCES

1. Fazeli, M., J.P. Florez, and R.A. Simao, *Improvement in adhesion of cellulose fibers to the thermoplastic starch matrix by plasma treatment modification.* Composites Part B-Engineering, 2019. **163**: p. 207-216.
2. *Composition of Composites*. [cited 2020 02.06.2020]; Available from: https://www.tenmat.com/news/the-only-way-to-fulfil-the-uic-510-1-interchangeability-conditions-is-to-use-composite-material-find-out-why/.
3. *Composites*. [cited 2020 02.06.2020]; Available from: https://www.essentialchemicalindustry.org/materials-and-applications/composites.html.
4. N Saria Sahreen, D.E.V.S.R., H. Raghavendra Rao, *Fabrication, Testing, Analysis on Glass and Jute Fibers Reinforced with Bentonite Nano Clay Filler, Epoxy Hybrid Composites*. 2005, Int. J. Innv. Res. Sci. Engg. Tech. p. 9194-9201.
5. Author links open overlay panel U.S.Toti, S.G.K., C.T. Laurencin, R. Mathew, D. Balasubramaniam, *Handbook of Medical Textiles*. Drug-releasing textiles. Vol. 7. 2011: Woodhead Publishing Series.
6. Babak Jahani, X.W., Amanda Brooks, *Additive Manufacturing Techniques for Fabrication of Bone Scaffolds for Tissue Engineering Applications,*. 2020: Journal of Recent Progress in Materials.
7. Daniels, W.W., *Relationship Between Fiber Properties and Fabric Wrinkle Recovery.* Textile Research Journal, 1960 ***30***: p. 656–661.
8. Fangueiro, R., et al., *Wicking Behavior and Drying Capability of Functional Knitted Fabrics.* Textile Research Journal, 2010. **80**(15): p. 1522-1530.
9. Simal, A.L. and A.R. Martin, *Structure of heat-treated Nylon 6 and 6.6 fibers. I. The shrinkage mechanism.* Journal of Applied Polymer Science, 1998. **68**(3): p. 441-452.
10. Elgarhy, Y.M., *Polyamide fiber substrate having stain resistance, composition and method*, U.S. Patent, Editor. Yassin M. Elgarhy: USA.
11. Kadolph, S., *Textiles*. 2002: Prentice Hall.
12. M.A., B.K.a.I., *Natural Fiber as a substitute to Synthetic Fiber in Polymer Composites: A Review*. 2013, International Science Community Association. p. 46-53.
13. Singh Z, B.S., *Toxicity of Synthetic Fibres & Health.* Adv Res Text Eng, 2017. **2**(1): p. 1012.
14. Andreas Schmidt, E.B., Eckhard Schollmeyer, *Damage to Natural and Synthetic Fibers Treated in Supercritical Carbon Dioxide at 300 bar and Temperatures up to 160°C*. 2002. p. 1023-1032.
15. Akil, H.M., et al., *Kenaf fiber reinforced composites: A review.* Materials & Design, 2011. **32**(8-9): p. 4107-4121.
16. Kozlowski, R. and M. Wladyka-Przybylak, *Flammability and fire resistance of composites reinforced by natural fibers.* Polymers for Advanced Technologies, 2008. **19**(6): p. 446-453.
17. Tajuddin, M., Z. Ahmad, and H. Ismail, *A Review of Natural Fibers and Processing Operations for the Production of Binderless Boards.* Bioresources, 2016. **11**(2): p. 5600-5617.
18. Jagadeesh, D., et al., *Preparation and Properties of Propylene Glycol Plasticized Wheat Protein Isolate Novel Green Films.* Journal of Polymers and the Environment, 2013. **21**(4): p. 930-936.

19. Rao KMM, R.K., Prasad AVR, *Fabrication and testing of natural fibre composites: vakka, sisal, bamboo and banana*. 2010, Materials & Design. p. 508-513.
20. Satyanarayana, K.G., J.L. Guilmaraes, and F. Wypych, *Studies on lignocellulosic fibers of Brazil. Part I: Source, production, morphology, properties and applications.* Composites Part a-Applied Science and Manufacturing, 2007. **38**(7): p. 1694-1709.
21. Amir Lotfi, H.L., Dzung Viet Dao, Gangadhara B Prusty, *Natural fiber–reinforced composites: A review on material, manufacturing, and machinability.* Journal of Thermoplastic Composite Materials, 2019.
22. Goutianos, S., et al., *Development of flax fibre based textile reinforcements for composite applications.* Applied Composite Materials, 2006. **13**(4): p. 199-215.
23. Jenkins, D.J.A., et al., *Dietary Fibers, Fiber Analogs, And Glucose-Tolerance - Importance Of Viscosity.* British Medical Journal, 1978. **1**(6124): p. 1392-1394.
24. Burley V.J., B.J.E., *Action of Dietary Fiber on the Satiety Cascade*. 1990: Springer, Boston, MA.
25. Shinoj, S., et al., *Oil palm fiber (OPF) and its composites: A review.* Industrial Crops and Products, 2011. **33**(1): p. 7-22.
26. *Natural Fiber Composites (NFC) Market Size, Share & Trends Analysis Report By Raw Material, By Matrix, By Technology, By Application, And Segment Forecasts, 2018 - 2024*. Available from: https://www.grandviewresearch.com/industry-analysis/natural-fiber-composites-market.
27. C. Elanchezhian, B. VijayaRamnath, G. Ramakrishnan, M. Rajendrakumar, V. Naveenkumar, M.K. and Saravanakumar, *Review on mechanical properties of natural fiber composites*. 2018. p. 1785–1790
28. Ramesh, M., et al., *Mechanical and Water Intake Properties of Banana-Carbon Hybrid Fiber Reinforced Polymer Composites.* Materials Research-Ibero-American Journal of Materials, 2017. **20**(2): p. 365-376.
29. P.J. LeMahieu, E.S.O., and D.H. Putnam. *Kenaf.* [cited 2020 February 14]; Available from: https://hort.purdue.edu/newcrop/afcm/kenaf.html.
30. Bhardwaj, H.L., C.L. Webber, and G.S. Sakamoto, *Cultivation of kenaf and sunn hemp in the mid-Atlantic United States.* Industrial Crops and Products, 2005. **22**(2): p. 151-155.
31. Abdal Basit Adam Mariod, M.E., Saeed Mirghani, Ismail Hussein, *Unconventional Oilseeds and Oil Sources*. 2017: Academic Press. 45-51.
32. Ayerza, R. and W. Coates, *Kenaf performance in northwestern Argentina.* Industrial Crops and Products, 1996. **5**(3): p. 223-228.
33. Mambelli, S. and S. Grandi, *Yield and quality of kenaf (hibiscus-cannabinus l) stem as affected by harvest date and irrigation.* industrial crops and products, 1995. **4**(2): p. 97-104.
34. Rouison, D., M. Sain, and M. Couturier, *Resin transfer molding of natural fiber reinforced composites: cure simulation.* Composites Science and Technology, 2004. **64**(5): p. 629-644.
35. Nishino, T., et al., *Kenaf reinforced biodegradable composite.* Composites Science and Technology, 2003. **63**(9): p. 1281-1286.
36. *Kenaf Bio-Energy*. 2015 [cited 2020 16 February]; Available from: http://www.kenafibers.com/kenaf.html.
37. Khalid Rehman Hakeem , M.J., Othman Y. Alothman, *Agricultural Biomass Based Potential Materials*. 2015: Springer. 505.

38. Lee, S.A. and M.A. Eiteman, *Ground kenaf core as a filtration aid.* Industrial Crops and Products, 2001. **13**(2): p. 155-161.
39. Karnani, R., M. Krishnan, and R. Narayan, *Biofiber-reinforced polypropylene composites.* Polymer Engineering and Science, 1997. **37**(2): p. 476-483.
40. Rowell, R.M., et al., *Properties of kenaf/polypropylene composites.* Kenaf properties, processing and products. Mississippi State, MS : Mississippi State University, Ag & Bio Engineering, 1999: p. 381-392.
41. Ramaswamy, G.N., et al., *Kenaf nonwovens as substrates for laminations.* Industrial Crops and Products, 2003. **17**(1): p. 1-8.
42. Vilay, V., et al., *Effect of fiber surface treatment and fiber loading on the properties of bagasse fiber-reinforced unsaturated polyester composites.* Composites Science and Technology, 2008. **68**(3-4): p. 631-638.
43. Edeerozey, A.M.M., et al., *Chemical modification of kenaf fibers.* Materials Letters, 2007. **61**(10): p. 2023-2025.
44. Kim, H.J. and D.W. Seo, *Effect of water absorption fatigue on mechanical properties of sisal textile-reinforced composites.* International Journal of Fatigue, 2006. **28**(10): p. 1307-1314.
45. George, J., M.S. Sreekala, and S. Thomas, *A review on interface modification and characterization of natural fiber reinforced plastic composites.* Polymer Engineering and Science, 2001. **41**(9): p. 1471-1485.
46. Dempsey, J.M., *Fiber crops*. 1975, Florida, USA: The Univ. Presses of Florida, Gainesville.
47. Brown, R.C. and T.R. Brown, *Biorenewable Resources: Engineering New Products from Agriculture, 2nd Edition.* Biorenewable Resources: Engineering New Products from Agriculture, 2nd Edition, 2014: p. 1-375.
48. T. Seller Jr., N.A.R.E., *Kenaf properties, processing, and products*. 1999.
49. Wood, I.M.I.M., *Fibre crops : new opportunities for Australian agriculture / Ian M. Wood.* 1997, <Brisbane> : Queensland Dept. of Primary Industries.
50. Datwyler, S.L. and G.D. Weiblen, *Genetic variation in hemp and marijuana (Cannabis sativa L.) according to amplified fragment length polymorphisms.* Journal of Forensic Sciences, 2006. **51**(2): p. 371-375.
51. *Kenaf – The Legal Cousin of Hemp*. 2015; Available from: https://www.hempinc.com/kenaf-the-legal-cousin-of-hemp/.
52. *International Jute Study Group Datasheet*, I.J.S. Group, Editor. 2014.
53. Naheed Saba, P.M.T., Mohammad Jawaid, Khalina Abdan, Nor Azowa Ibrahim, *Potential Utilization of Kenaf Biomass in Different Applications*, in *Agricultural biomass based potential materials*. 2015, Springer-Verlag, Switzerland.
54. Danalatos, N., and Archontoulis, S. *Sowing time and plant density effects on growth and biomass productivity of two kenaf varieties in central Greece.* in *International Conference on Industrial Crops and Rural Development*. 2005.
55. Pervaiz, M. and M.M. Sain, *Carbon storage potential in natural fiber composites.* Resources Conservation and Recycling, 2003. **39**(4): p. 325-340.
56. Wang, J.H. and G.N. Ramaswamy, *One-step processing and bleaching of mechanically separated kenaf fibers: Effects on physical and chemical properties.* Textile Research Journal, 2003. **73**(4): p. 339-344.

57. Cook, C.G. *Effect of soil salinity on kenaf performance in California*. in *Annual Conference Proceedings*. 1998. The Society.
58. J.R., O. *Weed control in kenaf*. in *Proc. Int. Kenaf Conf.* 1964.
59. Neagu, R.C., E.K. Gamstedt, and F. Berthold, *Stiffness contribution of various wood fibers to composite materials.* Journal of Composite Materials, 2006. **40**(8): p. 663-699.
60. Sheldon, A., *Preliminary Evaluation of Kenaf as a Structural Material*, in *Civil Engineering*. 1997, Clemson University. 61. I.S. Aji, S.M.S., E.S. Zainudin, K. Abdan, *Kenaf fibres as reinforcement for polymeric composites: a review*. 2009, Int J Mech Mater Eng. p. 239-248.
61. I.S. Aji, S.M.S., E.S. Zainudin, K. Abdan, *Kenaf fibres as reinforcement for polymeric composites: a review*. 2009, Int J Mech Mater Eng. p. 239-248.
62. Author links open overlay panel Paul Wambua, J.I., Ignaas Verpoest, *Natural fibres: can they replace glass in fibre reinforced plastics?* Composites Science and Technology Volume, 2003. **63**(9): p. 1259-1264.
63. A., A., *Fibers for Strengthering of Timber Structures.* 2006.
64. Parvej, M.S., et al., *Atomic force microscopy-based nanomechanical characterization of kenaf fiber.* Journal of Composite Materials.
65. Jonas, R. and L.F. Farah, *Production and application of microbial cellulose.* Polymer Degradation and Stability, 1998. **59**(1-3): p. 101-106.
66. Hokkanen, S., A. Bhatnagar, and M. Sillanpaa, *A review on modification methods to cellulose-based adsorbents to improve adsorption capacity.* Water Research, 2016. **91**: p. 156-173.
67. Alfred Rudin, P.C., *Biopolymers*, in *The Elements of Polymer Science & Engineering (Third Edition)*. 2013.
68. El-Saied, H., A.H. Basta, and R.H. Gobran, *Research progress in friendly environmental technology for the production of cellulose products (bacterial cellulose and its application).* Polymer-Plastics Technology and Engineering, 2004. **43**(3): p. 797-820.
69. Ross, P., R. Mayer, and M. Benziman, *Cellulose Biosynthesis and Function in Bacteria.* Microbiological Reviews, 1991. **55**(1): p. 35-58.
70. Sani, A. and Y. Dahman, *Improvements in the production of bacterial synthesized biocellulose nanofibres using different culture methods.* Journal of Chemical Technology and Biotechnology, 2010. **85**(2): p. 151-164.
71. Rivas, B., et al., *Development of culture media containing spent yeast cells of Debaryomyces hansenii and corn steep liquor for lactic acid production with Lactobacillus rhamnosus.* International Journal of Food Microbiology, 2004. **97**(1): p. 93-98.
72. Brigham, C., *Biopolymers: Biodegradable Alternatives to Traditional Plastics*, in *Green Chemistry*, B. Török, Editor. 2017, Elsevier: University of Massachusetts Boston, Boston, MA, United States.
73. Klemm, D., et al., *Cellulose: Fascinating biopolymer and sustainable raw material.* Angewandte Chemie-International Edition, 2005. **44**(22): p. 3358-3393.
74. Abitbol, T., et al., *Nanocellulose, a tiny fiber with huge applications.* Current Opinion in Biotechnology, 2016. **39**: p. 76-88.
75. Zadorecki, P. and A.J. Michell, *Future-Prospects for Wood Cellulose as Reinforcement in Organic Polymer Composites.* Polymer Composites, 1989. **10**(2): p. 69-77.

76. Orts, W.J., et al., *Application of cellulose microfibrils in polymer nanocomposites.* Journal of Polymers and the Environment, 2005. **13**(4): p. 301-306.
77. S. Nishikawa , S.O., *Transmission of X-Rays through Fibrous, Lamellar and Granular Substances.* Proceedings of the Tokyo Mathematico-Physical Society. 2nd Series, 1913. **7**(8).
78. Mark, K.H.M.H., *Über den Bau des krystallisierten Anteils der Cellulose.* Berichte der deutschen chemischen Gesellschaft (A and B Series), 1928. **61**(4): p. 593-614.
79. Hermans, P.H., J. DeBooys, and C.K.Z. Mann, *Über die Gestalt und die Beweglichkeit des Moleküls der Zellulose.* 1943. **102**: p. 169-180.
80. Jones, D.W., *Crystalline modifications of cellulose. Part III. The derivation and preliminary study of possible crystal structures.* J. Polym. Sci., 1958. **32**(125).
81. Marchessault, C.Y.L.R.H., *Infrared spectra of crystalline polysaccharides. I. Hydrogen bonds in native celluloses.* Journal of Polymer Science, 1959. **37**(132): p. 385-395.
82. Ferrier, W.G., *The Crystal and Molecular Structure of β-D-glucose.* Acta Crystallographica, 1962. **16**: p. 1023-1031.
83. Honjo, G. and M. Watanabe, *Examination of cellulose fibre by the low-temperature specimen method of electron diffraction and electron microscopy.* Nature, 1958. **181**: p. 326.
84. Gardner, K.H. and J. Blackwell, *The structure of native cellulose.* J. Biopolymers, 1974. **13**(10).
85. Anatole Sarko, R.M., *Packing Analysis of Carbohydrates and Polysaccharides. III. Valonia Cellulose and Cellulose II.* ACS Publications, 1974. **7**(4): p. 486-494.
86. Sarko, A.J.S., *Packing Analysis of Carbohydrates and Polysaccharides. 6. Molecular and Crystal Structure of Regenerated Cellulose II.* 1976. **9**(5): p. 851-857.
87. Rajai H. Atalla, D.L.V., *Native Cellulose: A Composite of Two Distinct Crystalline Forms.* 1984. **223**(4633): p. 283-285.
88. P. S. Belton, S.F.T., N. Cartier, H. Chanzy, *High-resolution solid-state carbon-13 nuclear magnetic resonance spectroscopy of tunicin, an animal cellulose.* M*acromolecules* 1989. **22**(4): p. 1615-1617
89. Tomas Larsson, U.W., Tommy Iversen, *Determination of the cellulose Iα allomorph content in a tunicate cellulose by CP/MAS 13C-NMR spectroscopy.* 1995.
90. Sugiyama, J., et al., *Transformation of Valonia Cellulose Crystals by an Alkaline Hydrothermal Treatment.* Macromolecules, 1990. **23**(12): p. 3196-3198.
91. Sugiyama, J., R. Vuong, and H. Chanzy, *Electron-Diffraction Study on the 2 Crystalline Phases Occurring in Native Cellulose from an Algal Cell-Wall.* Macromolecules, 1991. **24**(14): p. 4168-4175.
92. Koyama, M., et al., *Parallel-up structure evidences the molecular directionality during biosynthesis of bacterial cellulose.* Proceedings of the National Academy of Sciences of the United States of America, 1997. **94**(17): p. 9091-9095.
93. Andreas P. Heiner, J.S., OlleTeleman, *Crystalline cellulose Iα and Iβ studied by molecular dynamics simulation.* 1995. **2**(273): p. 207-223.
94. Aabloo, A., et al., *Studies of Crystalline Native Celluloses Using Potential-Energy Calculations.* Cellulose, 1994. **1**(2): p. 161-168.
95. Aabloo, A. and A.D. French, *Preliminary Potential-Energy Calculations of Cellulose I-Alpha Crystal-Structure.* Macromolecular Theory and Simulations, 1994. **3**(1): p. 185-191.

96. Vietor, R.J., et al., *A priori crystal structure prediction of native celluloses.* Biopolymers, 2000. **54**(5): p. 342-354.
97. Simon, I., et al., *Structure of Cellulose .2. Low-energy Crystalline Arrangements.* Macromolecules, 1988. **21**(4): p. 990-998.
98. Finkenstadt, V.L. and R.P. Millane, *Crystal structure of Valonia cellulose I beta.* Macromolecules, 1998. **31**(22): p. 7776-7783.
99. Nishiyama, Y., P. Langan, and H. Chanzy, *Crystal structure and hydrogen-bonding system in cellulose 1 beta from synchrotron X-ray and neutron fiber diffraction.* Journal of the American Chemical Society, 2002. **124**(31): p. 9074-9082.
100. Nishiyama, Y., *Structure and properties of the cellulose microfibril.* Journal of Wood Science, 2009. **55**(4): p. 241-249.
101. Diddens, I., et al., *Anisotropic Elastic Properties of Cellulose Measured Using Inelastic X-ray Scattering.* Macromolecules, 2008. **41**(24): p. 9755-9759.
102. Matsuo, M., et al., *Effect of Orientation Distribution and Crystallinity on the Measurement by X-Ray-Diffraction of The Crystal-Lattice Moduli of Cellulose-I And Cellulose-II.* Macromolecules, 1990. **23**(13): p. 3266-3275.
103. Sakurada, I., T. Ito, and K. Nakamae, *Elastic moduli of polymer crystals for the chain axial direction.* Makromolekulare Chemie, 1964. **75**: p. 1-10.
104. Sakurada, I., Y. Nukushina, and T. Ito, *Experimental determination of elastic modulus of crystalline regions in oriented polymers.* Journal of Polymer Science, 1962. **57**(165): p. 651-660.
105. Lahiji, R.R., et al., *Atomic Force Microscopy Characterization of Cellulose Nanocrystals.* Langmuir, 2010. **26**(6): p. 4480-4488.
106. Paavilainen, S., T. Rog, and I. Vattulainen, *Analysis of Twisting of Cellulose Nanofibrils in Atomistic Molecular Dynamics Simulations.* Journal of Physical Chemistry B, 2011. **115**(14): p. 3747-3755.
107. Sturcova, A., G.R. Davies, and S.J. Eichhorn, *Elastic modulus and stress-transfer properties of tunicate cellulose whiskers.* Biomacromolecules, 2005. **6**(2): p. 1055-1061.
108. Rusli, R. and S.J. Eichhorn, *Determination of the stiffness of cellulose nanowhiskers and the fiber-matrix interface in a nanocomposite using Raman spectroscopy.* Applied Physics Letters, 2008. **93**(3).
109. Guhados, G., W.K. Wan, and J.L. Hutter, *Measurement of the elastic modulus of single bacterial cellulose fibers using atomic force microscopy.* Langmuir, 2005. **21**(14): p. 6642-6646.
110. Hsieh, Y.C., et al., *An estimation of the Young's modulus of bacterial cellulose filaments.* Cellulose, 2008. **15**(4): p. 507-513.
111. Paavilainen, S., et al., *Mechanical properties of cellulose nanofibrils determined through atomistic molecular dynamics simulations.* Nordic Pulp & Paper Research Journal, 2012. **27**(2): p. 282-286.
112. Iwamoto, S., et al., *Elastic Modulus of Single Cellulose Microfibrils from Tunicate Measured by Atomic Force Microscopy.* Biomacromolecules, 2009. **10**(9): p. 2571-2576.
113. Cheng, Q.Z. and S.Q. Wang, *A method for testing the elastic modulus of single cellulose fibrils via atomic force microscopy.* Composites Part a-Applied Science and Manufacturing, 2008. **39**(12): p. 1838-1843.
114. Thiruchitrambalam, M., A. Alavudeen, and N. Venkateshwaran, *Review on kenaf fiber composites.* Reviews on Advanced Materials Science, 2012. **32**(2): p. 106-111.

115. Anuar, H., et al., *Improvement of Mechanical Properties of Injection-Molded Polylactic Acid-Kenaf Fiber Biocomposite.* Journal of Thermoplastic Composite Materials, 2012. **25**(2): p. 153-164.
116. Zampaloni, M., et al., *Kenaf natural fiber reinforced polypropylene composites: A discussion on manufacturing problems and solutions.* Composites Part a-Applied Science and Manufacturing, 2007. **38**(6): p. 1569-1580.
117. Salleh, F.M., et al., *Effects of extrusion temperature on the rheological, dynamic mechanical and tensile properties of kenaf fiber/HDPE composites.* Composites Part B-Engineering, 2014. **58**: p. 259-266.
118. M.A.A. Ghani, Z.S., K.M. Hyie, M.N. Berhan, Y.M.D. Taib, M.A.I. Bakri, *Mechanical properties of kenaf/fiberglass polyester hybrid composite*. 2012, Procedia Engineering. p. 1654 – 1659.
119. Asumani, O.M.L., R.G. Reid, and R. Paskaramoorthy, *The effects of alkali-silane treatment on the tensile and flexural properties of short fibre non-woven kenaf reinforced polypropylene composites.* Composites Part a-Applied Science and Manufacturing, 2012. **43**(9): p. 1431-1440.
120. Ochi, S., *Tensile Properties of Kenaf Fiber Bundle*. 2010, SRX Materials Science.
121. Shibata, S., Y. Cao, and I. Fukurnoto, *Flexural modulus of the unidirectional and random composites made from biodegradable resin and bamboo and kenaf fibres.* Composites Part a-Applied Science and Manufacturing, 2008. **39**(4): p. 640-646.
122. Cicala, G., et al., *Properties and performances of various hybrid glass/natural fibre composites for curved pipes.* Materials & Design, 2009. **30**(7): p. 2538-2542.
123. Mohanty, A.K., M. Misra, and G. Hinrichsen, *Biofibres, biodegradable polymers and biocomposites: An overview.* Macromolecular Materials and Engineering, 2000. **276**(3-4): p. 1-24.
124. Parikh, D.V., et al., *Improved chemical retting of kenaf fibers.* Textile Research Journal, 2002. **72**(7): p. 618-624.
125. Rassmann, S., R. Paskaramoorthy, and R.G. Reid, *Effect of resin system on the mechanical properties and water absorption of kenaf fibre reinforced laminates.* Materials & Design, 2011. **32**(3): p. 1399-1406.
126. P Boresi, J.S., *Advanced Mechanics of Solids*. 6 ed., United States of America: John Wiley and Sons, Inc.
127. Liu, J.Y. and R.J. Ross, *Relationship between radial compressive modulus of elasticity and shear modulus of wood.* Wood and Fiber Science, 2005. **37**(2): p. 201-206.
128. Chinga-Carrasco, G., *Cellulose fibres, nanofibrils and microfibrils: The morphological sequence of MFC components from a plant physiology and fibre technology point of view.* Nanoscale Research Letters, 2011. **6**.
129. *Improved Surface Characterization with AFM Imaging*. November 1, 2017 [cited 2020 November 1]; Available from: https://www.techbriefs.com/component/content/article/tb/supplements/pit/features/applications/27833.
130. More, N.a. *Oltespa*. Available from: https://www.nanoandmore.com/AFM-Tip-OLTESPA.
131. Masch. *HQ:CSC17/HARD/AL BS*. Available from: https://www.spmtips.com/afm-tip-hq-csc17-hard-al-bs.

132. USA, N. *ISC-125C40-R*. Available from: https://www.nanoandmore.com/AFM-Probe-ISC-125C40-R.
133. Solutions, N. *AFM Edge Probes*. Available from: https://www.ndsolns.com/afm-edge-probes/.
134. System, P. *AFM Metrology Considerations of Hard Disk Manufacturing*. November 1, 2020]; Available from: https://parksystems.com/jp/applications/electrical-electronics/data-storage/202-afm-metrology-considerations-of-hard-disk-manufacturing.
135. Karen Gaskell, D.R. *AFM Standard Operating Procedure*. 2013; Available from: http://www.chem.umd.edu/wp-content/uploads/2013/05/AFM-SOP-ver2.pdf.
136. *Determining the Elasticity of Graphene*. 2019 [cited 2020 November 23]; Available from: https://analyticalscience.wiley.com/do/10.1002/imaging.6677.
137. Khalil, A., et al., *Electrospun metallic nanowires: Synthesis, characterization, and applications.* Journal of Applied Physics, 2013. **114**(17).
138. Hertz, H., *Über die Berührung fester elastischer Körper.* Journal für die reine und angewandte Mathematik, 1881. **92**: p. 156-171.
139. Johnson, K.L., *Contact mechanics*. 1992, Cambridge, UK: Cambridge University Press.
140. Maugis, D., *Extension of the johnson-kendall-roberts theory of the elastic contact of spheres to large contact radii.* Langmuir, 1995. **11**(2): p. 679-682.
141. Johnson, K.L., K.K. , and a.A.D. Roberts, *Surface energy and the contact of elastic solids.* Proceedings of Royal Society A, 1971. **324**: p. 301-313.
142. *Contact mechanics*. 5.20.2019]; Available from: https://en.wikipedia.org/wiki/Contact_mechanics.
143. Babahosseini, H., et al., *Biomechanical profile of cancer stem-like/tumor-initiating cells derived from a progressive ovarian cancer model.* Nanomedicine-Nanotechnology Biology and Medicine, 2014. **10**(5): p. 1013-1019.
144. B. V. Derjaguin, V.M.M., and YU. P. Toporov, *Effect of contact deformations on the adhesion of particles*. 1975, Journal of Colloid and Interface Science. p. 314-326.
145. M.A., R.S.B., *The cohesive force between solid surfaces and the surface energy of solids.* The London, Edinburgh, and Dublin Philosophical Magazine and Journal of Science, 2009. **13**(86): p. 853-862.
146. Maugis, D., *Adhesion of spheres - the jkr-dmt transition using a dugdale model.* Journal of Colloid and Interface Science, 1992. **150**(1): p. 243-269.
147. Jeffery S. Marshall, U.o.V., Shuiqing Li, *Adhesive Particle Flow*, in *Adhesive Particle Flow*. Contact Mechanics with Adhesion Forces, Tsinghua University, Beijing p. 81-129.
148. Tabor, D., *Surface forces and surface interactions*. 1977, Journal of Colloid and Interface Science. p. 2-13.
149. Johnson, K.L. and J.A. Greenwood, *An adhesion map for the contact of elastic spheres.* Journal of Colloid and Interface Science, 1997. **192**(2): p. 326-333.
150. Wang, H.R., et al., *Nanomechanical characterization of rod-like superlattice assembled from tobacco mosaic viruses.* Journal of Applied Physics, 2013. **113**(2).
151. Wang, X.N., et al., *Nanomechanical characterization of polyaniline coated tobacco mosaic virus nanotubes.* Journal of Biomedical Materials Research Part A, 2008. **87A**(1): p. 8-14.
152. Zhao, Y., Z.B. Ge, and J.Y. Fang, *Elastic modulus of viral nanotubes.* Physical Review E, 2008. **78**(3).

153. Gindl, W., et al., *Anisotropy of the modulus of elasticity in regenerated cellulose fibres related to molecular orientation.* Polymer, 2008. **49**(3): p. 792-799.
154. Mahjoub, R., et al., *Characteristics of continuous unidirectional kenaf fiber reinforced epoxy composites.* Materials & Design, 2014. **64**: p. 640-649.
155. Yu, Y., et al., *Mechanical characterization of single bamboo fibers with nanoindentation and microtensile technique.* Holzforschung, 2011. **65**(1): p. 113-119.
156. ASTM, *Standard Test Method for Tensile Strength and Young's Modulus of Fibers*. 2003.
157. Hashim, S.T.W.L.a.J., *Interfacial Adhesion Characteristics of Kenaf Fibres Subjected to Different Polymer Matrices and Fibre Treatments*. 2014.
158. Biswas, S., et al., *Effect of Span Length on the Tensile Properties of Natural Fibers.* Advances in Materials and Processing Technologies Ii, Pts 1 and 2, 2011. **264-265**: p. 445-450.
159. Pan, N., et al., *The size effects on the mechanical behaviour of fibres.* Journal of Materials Science, 1997. **32**(10): p. 2677-2685.
160. Trustrum, K. and A.D. Jayatilaka, *Applicability of weibull analysis for brittle materials.* Journal of Materials Science, 1983. **18**(9): p. 2765-2770.
161. Parvej, M.S., X.N. Wang, and L. Jiang, *AFM based nanomechanical characterization of cellulose nanofibril.* Journal of Composite Materials, 2020. **54**(28): p. 4487-4493.
162. Sader, J.E., et al., *Method for the calibration of atomic-force microscope cantilevers.* Review of Scientific Instruments, 1995. **66**(7): p. 3789-3798.
163. Nakamura, K., et al., *Poisson's ratio of cellulose I-beta and cellulose II.* Journal of Polymer Science Part B-Polymer Physics, 2004. **42**(7): p. 1206-1211.
164. Moon, R.J., et al., *Cellulose nanomaterials review: structure, properties and nanocomposites.* Chemical Society Reviews, 2011. **40**(7): p. 3941-3994.
165. Gao, S.L. and J.K. Kim, *Cooling rate influences in carbon fibre/PEEK composites. Part 1. Crystallinity and interface adhesion.* Composites Part a-Applied Science and Manufacturing, 2000. **31**(6): p. 517-530.
166. Yan, Y.D., et al., *AFM tip characterization by using FFT filtered images of step structures.* Ultramicroscopy, 2016. **160**: p. 155-162.
167. Salvetat, J.P., et al., *Elastic and shear moduli of single-walled carbon nanotube ropes.* Physical Review Letters, 1999. **82**(5): p. 944-947.
168. Tan, E.P.S. and C.T. Lim, *Physical properties of a single polymeric nanofiber.* Applied Physics Letters, 2004. **84**(9): p. 1603-1605.

APPENDIX A. FUNCTION TO FILTER DATA

```
%this program eliminates the unnecessary data and keeps only the extension
%data. limiting condition for peak is kept .15
% d is the element  number where curve starts to rise which is set at zero
% and the y value is upshifted to positive value
function [d,f]=filterit(x,y)
z = length(y);
amp = input('What is the Amplitude?');
sen = input('What is the Sensitivity?');
k = input('What is the Spring Constant?');
%amp = .15
%finding where the fluctuation stops
for i = 2 : z
    if y(i)-y(i-1)>=amp
        m=i+1;
    end
end
p = m;
%forming filterted deflection
for i = 1 : z-p+1
    d(i)=x(p);
    p = p +1;
end
p = m;
%forming filterted force
for i = 1 : z-p+1
    f(i)=y(p) * amp * k;
    p = p +1;
end
yoffset = f(1);
p = m;
%killing yoffset
for i = 1 : z-p+1
    f(i)=f(i)-yoffset;
end
plot(d,f)
p = m;
xoffset = input('X value of the point you want to shift?');
%the point will be always shifted to x = 5
for i = 1 : z-p+1
    d(i)=d(i)-xoffset + 5;
end
end
```

APPENDIX B. PROGRAM TO FILTER DATA

```
dataset = xlsread('yc','yc420','A3: B355'); %contains force and displacement
raw data found from AFM
x = dataset(:,1);
y = dataset(:,2);
[p,q]=filterit(x,y); % p and q are dz and F respectively
plot(p,q)
A=[p' q'];
filename = 'filtered_data.xlsx';
xlswrite(filename,A)
```

APPENDIX C. FUNCTION TO FIND ROOT MEAN SQUARE FROM DATA THROUGH SHOOTING METHOD

```
function RSQ=JKRRSQ(a,y,E2,P)
avg = mean(y);
x = sum((y - avg).^2);  %SUM OF (force - avg force)^2  %importing (force -
avg force)^2
len = length(y);
R = 15;
P = 9.78;
G = 3*P/(2 * pi * R);
v1 = .27;E1 = 150;v2 = 0.3;
k1 = (1 - v1 * v1)/(pi * E1);
k2 = (1 - v2 * v2)/(pi * E2);
K = 4 / (3 * pi * (k1 + k2));
for n = 1:len
    e = 10^-6 ;
    low = 3;
    high = 13;
    for i = 1:10000000
        aa = low;
        ad = aa/2 * log((R+aa)/(R-aa)) - sqrt(8* pi* aa*G/(3*K)) - a(n);
        bb= high;
        cc = (aa + bb)/2;
        cd = cc/2 * log((R+cc)/(R-cc)) - sqrt(8* pi* cc*G/(3*K)) - a(n);
        if ad * cd < 0
            low = aa;
            high = cc;
        else
            low = cc;
            high = bb;
        end
        if abs(high - low)<e
            break;
        end
    end
    b(n)= cc;
end
dz = a;
a = b;
for m = 1:len
T(m) = 3 * a(m) * K/2 * ( (R^2 - (a(m))^2)/(4*a(m)) * log((R+a(m))/(R-a(m)))
+ dz(m) - R/2);
end
T = T - T(1); %shifting to origin
all = [dz T'];
plot(dz,T'); hold on;
dataset = xlsread('Result','deflection','B2:B35');
dd = dataset(:,1);
scatter(dz,dd');
SSE = sum((T'-y).^2);
RSQ = (1 - SSE/x)*100
End
```

APPENDIX D. PROGRAM TO FIND ROOT MEAN SQUARE FROM DATA THROUGH SHOOTING METHOD

```
dataset = xlsread('Result','deflection','A2:B35'); %The two column contains
Δz and Normal force data of Figure 5.5
a = dataset(:,1); % importing dz
y = dataset(:,2); %importing force
P = 9.78;
E2 = input('What is the predicted modulus?');
RSQ=JKRRSQ(a,y,E2,P);
```